

**Master Thesis**  
**Simulation Sciences**

Rheinisch-Westfälische Technische Hochschule (RWTH) Aachen

Fakultät 4 - Maschinenwesen

---

TITAN: A code and its applications for time-dependent  
transport and angular momentum in nanostructures

---

February 26, 2018

**Jens Renè Suckert**



# Eigenhändigkeitserklärung

Diese Arbeit ist von mir selbstständig angefertigt und verfasst. Es sind keine anderen als die angegebenen Quellen und Hilfsmittel benutzt worden.

---

(Ort, Datum)

---

(Unterschrift)

Diese Arbeit wurde betreut von:

Betreuer:	Prof. Dr. Samir Lounis	(FZJ, IAS-1)
Co-Betreuer:	Dr. Filipe S.M. Guimarães	(FZJ, IAS-1)
1. Prüfer:	Prof. Dr. Samir Lounis	(FZJ, IAS-1)
2. Prüfer:	Prof. Dr. Marjana Ležaić	(FZJ, PGI-1)

Sie wurde angefertigt in der Forschungszentrum Jülich GmbH im Institute for Advanced Simulation.



*I'm being quoted to introduce something,  
but I have no idea what it is  
and certainly don't endorse it.*

– Randall Munroe



# Contents

<b>1. Introduction</b>	<b>1</b>
<b>2. Theory</b>	<b>3</b>
2.1. Hamiltonian . . . . .	3
2.1.1. Crystal Hamiltonian . . . . .	4
2.1.2. Tight-binding approximation . . . . .	6
2.1.3. Coulomb interaction . . . . .	9
2.1.4. Zeeman interaction . . . . .	11
2.1.5. Spin-orbit interaction . . . . .	11
2.2. Ground state properties . . . . .	12
2.2.1. Band structure . . . . .	13
2.2.2. Density of states . . . . .	13
2.2.3. Magnetization and Stoner criterion . . . . .	14
2.3. Dynamical properties . . . . .	15
2.3.1. Linear response formalism . . . . .	15
2.3.2. Mean field approximation . . . . .	17
2.3.3. Random phase approximation . . . . .	18
2.3.4. Magnetic perturbations . . . . .	19
<b>3. Computational Methods</b>	<b>21</b>
3.1. Lattice setup . . . . .	21
3.2. Brillouin zone generation . . . . .	22
3.3. Complex continuation . . . . .	24
3.4. Energy-dependent Brillouin zone mesh . . . . .	26
3.5. Self-consistency . . . . .	27
3.6. Parallelization . . . . .	29
3.7. Full list of implementations . . . . .	30
<b>4. Numerical aspects</b>	<b>31</b>
4.1. Quality of ground state properties . . . . .	31
4.2. Convergence of dynamic calculations . . . . .	33
4.3. Performance . . . . .	33
4.4. Summary . . . . .	37
<b>5. Gilbert Damping</b>	<b>39</b>
5.1. Overview . . . . .	40
5.2. Breathing Fermi surface model (BFS) . . . . .	41
5.3. Ferromagnetic Resonance (FMR) . . . . .	42

5.4. Spin-correlation method (SCM) . . . . .	44
5.5. Torque-torque method (TTM) . . . . .	48
5.6. Torque-correlation method (TCM) . . . . .	52
5.6.1. Spin-orbit torque (TCM-SO) . . . . .	54
5.6.2. Exchange-correlation torque (TCM-XC) . . . . .	55
5.7. Summary of methods . . . . .	55
<b>6. Conclusions</b>	<b>61</b>
<b>References</b>	<b>63</b>
<b>A. Parameters</b>	<b>A 1</b>
A.1. bcc Fe . . . . .	A 2
A.2. fcc Co . . . . .	A 2
A.3. fcc Ni . . . . .	A 3

# 1. Introduction

The interrelation between charge, spin and orbital angular momentum in nanostructured systems will significantly shape future technologies [1]. When spin and orbital degrees of freedom interact, a variety of fascinating phenomena occur. From the conversion of spin into charge currents [2, 3, 4], as well as spin accumulations, generated by an electric currents [5], to topological insulators [6], the coupling of spin and orbital moments is subject of much interest and abundant research activities [7, 8, 9]. Excitations of spin waves by means of spin-orbit torques [10, 11, 12] can be used to achieve switching of the magnetization in ferromagnets [13] and antiferromagnets [14] in ultrafast speeds.

Even though these advanced investigations are pushing the field forward, fundamental questions regarding ordinary magnetization dynamics are still debated. The relaxation of magnetic moments, for example, has been studied for decades [15, 16, 17, 18], but still generated controversial results [19, 20, 21]. Since the ability to tune the energy dissipation of a precessing magnet would permit the optimization of magnetic switching times and the propagation of spin currents, a quantum-mechanical material-dependent description of the relaxation process from first principles is indispensable

From the arguments above, one can understand that a full quantum-mechanical investigation of dynamical effects is important to explore possible use cases of all these phenomena. This work introduces TITAN, an efficient simulation program, made with the purpose of investigating such intriguing effects. It uses a multi-orbital tight-binding model as basis to build a powerful, highly parallelized tool for the exploration of time-dependent transport and angular momentum properties in nanostructures.



Figure 1.1.: Logo of TITAN, representing an itinerant electron and its connection to spin and orbital degrees of freedom.

The intend of this thesis lies in presenting the basic theoretical concepts used as foundations of the code and to discuss the numerical aspects that are used to perform the calculations in a optimized way. This framework is examined by means of ground state properties for ferromagnetic bulk transtion metals, and then applied to the calculation of the Gilbert damping, an important aspect of magnetization dynamics.

This thesis is structured as follows:

Chapter 2 sets up the theoretical framework that builds the foundation of TITAN. The model Hamiltonian that is used to describe the electronic structure is carefully examined. A parametrized multi-orbital tight-binding approximation is used to describe the crystal structure of the system, which is extended by an effective Coulomb interaction, the spin-orbit interaction as well as interactions with external magnetic fields. This is followed by discussions about how the ground state properties of the system are accessed and how dynamical effects can be studied using linear response formalism.

The third chapter will display important core components of TITAN. New implementations are highlighted, in particular, the generalization of the code that enables the investigation of a broad set of materials. Additionally, it discusses how the code is optimized to allow more efficient calculations.

In chapter 4, the program is evaluated in terms of quality and performance. By calculations of electronic structure and magnetic ground state properties, the validity of the model will be tested. The efficiency of TITAN will be investigated by means of convergence and performance measurements.

As an application to TITAN, the fifth chapter investigates the Gilbert damping [16], a parameter of profound influence for magnetization dynamics. Several different methods for the description of these relaxation processes from a microscopical point-of-view are introduced. Using TITAN, these methods are thereupon compared to determine their similarities and differences.

In the last chapter, the work is concluded, summarizing the results and providing a short outlook on future research perspectives.

## 2. Theory

One of the most powerful and used approaches to obtain information about a system, without the use of phenomenological parameters, is density functional theory (DFT). Theoretically, the ground state properties of a system can be calculated from first principles. By describing the full Hilbert space of a quantum system, insight into the electronic and magnetic properties of materials is gained by application of quantum mechanics while only using fundamental constants. However, computation and storage costs for DFT-based methods increase drastically with the number of inequivalent atoms, making the treatment of complex systems from *ab initio* very time consuming and computationally intensive. In comparison, tight-binding methods are simplified models that are still based on quantum mechanics and capture the essential physics of the studied systems. In this thesis, a parametrized tight-binding model, using input obtained from DFT calculations for elemental bulk materials, is used to simulate the ground state properties of several bulk systems. The parameters for paramagnetic elemental bulk materials are obtained from *Handbook of the Band Structure of Elemental Solid* [22]. The model is extended to magnetic properties by introducing Hubbard two-body terms, Zeeman and spin-orbit interaction.

In the ground state of a system, observables can be obtained from the Green function formalism. They are essential to describe the system under investigation and can also be used to quantify the accuracy of the model compared to experimental results and other available *ab initio* simulations. Additionally, the study of dynamical behaviours in the system requires knowledge about the observables in their ground state. Dynamical properties of the system are obtained by calculation of linear response functions using the Kubo formalism [23].

Throughout this thesis atomic units are used, such that  $\hbar = e = m_e = \frac{1}{4\pi\epsilon_0} = 1$  and energies are given in Rydberg and length in Bohr units.

### 2.1. Hamiltonian

The Schrödinger equation can be used to describe quantum mechanical systems in condensed matter theory. Its time-independent version

$$\hat{H}|\Psi\rangle = E|\Psi\rangle \quad (2.1.1)$$

describes stationary systems whose properties remain unchanged over time, where  $\hat{H}$  is the Hamiltonian of the system,  $E$  is an eigenenergy associated to the many-body eigenstate  $|\Psi\rangle$ .

For a complete description of the electrons in a crystal, the Hamiltonian includes the kinetic energy  $\hat{T}$ , the interaction between electrons  $\hat{H}_{e-e}$ , the interaction between

ions  $\hat{H}_{i-i}$  as well as the interaction between electrons and ions  $\hat{H}_{e-i}$  and with external fields  $\hat{H}_{\text{ext}}$ :

$$\hat{H} = \hat{T} + \hat{H}_{e-e} + \hat{H}_{i-i} + \hat{H}_{e-i} + \hat{H}_{\text{ext}} . \quad (2.1.2)$$

In a crystal, the motion of ions is much slower than those of the electrons due to their higher mass. As such, one considers them to be frozen and the degrees of freedom for electrons and ions can be separated by means of the Born-Oppenheimer approximation [24]. For the description of the electrons in the system, the ion-ion interaction can be neglected as it only leads to a shift of the total energy. The electron-ion interaction is treated as a positive charged background in which the electrons are moving around.

In principle, the description of the many-body problem in condensed matter needs to be solved using the relativistic Dirac equation. As an approximation, one can treat relativistic effects by adding the spin-orbit interaction arising from the approximation of the Dirac equation to low velocities to the Hamiltonian in the Schrödinger equation. This spin-orbit interaction term is of fundamental importance to describe certain properties of the system, such as magnetic anisotropies, and phenomena such as magnetoresistances, the anomalous Hall effect and the spin Hall effect [25]. These effects offer a novel and promising way of reading and writing information in spintronic devices [9].

Taking all this into account, the full model Hamiltonian that will be used here, can be summarized as

$$\hat{H} = \hat{H}_{\text{Crystal}} + \hat{H}_{e-e} + \hat{H}_{\text{ext}} + \hat{H}_{\text{SO}} . \quad (2.1.3)$$

Each of these terms will be explored in one of the following sections.

### 2.1.1. Crystal Hamiltonian

The Coulomb interaction of electrons at position  $\vec{r}$  with a positively-charged periodic potential created by the ions at position  $\vec{R}_I + \vec{r}_i$ , where  $\vec{R}_I$  describes the center of an unit cell and  $\vec{r}_i$  the position of an atomic site inside this unit cell, is given by

$$\hat{H}_{e-i}(\vec{r}) = \sum_{Ii} \hat{H}_{\text{ion}, i}(\vec{r} - \vec{R}_I - \vec{r}_i) = \sum_{Ii} \frac{Z_i}{|\vec{r} - \vec{R}_I - \vec{r}_i|} . \quad (2.1.4)$$

The interaction between electrons will be treated separately in the next section. The crystal potential is written as a superposition of atomic ion potentials with charges  $Z_i$ . A system without any further interactions can therefore be written as

$$\hat{H}_{\text{Crystal}} = \frac{\vec{p}^2}{2} + \hat{H}_{e-i}(\vec{r}) , \quad (2.1.5)$$

where the first term, containing the linear momentum  $\vec{p}$  of an electron, describes its kinetic energy.

In second quantization, this model can be written as

$$\hat{H}_{\text{Crystal}} = \sum_{IJ} \sum_{ij} \sum_{\mu\nu} \sum_{\sigma} t_{\mu\nu}(\vec{R}_I + \vec{r}_i, \vec{R}_J + \vec{r}_j) c_{Ii\mu\sigma}^\dagger c_{Jj\nu\sigma} , \quad (2.1.6)$$

where an orthogonal basis of spin-dependent localized atomic orbitals has been used. Here, a system of periodic unit cells is assumed. The electron spin,  $\sigma$ , is given with respect to the quantization axis. The operator  $c_{Ii\mu\sigma}^\dagger$  ( $c_{Ii\mu\sigma}$ ) creates (annihilates) an electron at lattice position  $\vec{R}_I + \vec{r}_i$  with orbital moment  $\mu$  and spin  $\sigma$ . These operators fulfill the commutation relations

$$\begin{aligned} \{c_{Ii\mu\sigma}^\dagger, c_{Jj\nu\sigma'}^\dagger\} &= 0, \\ \{c_{Ii\mu\sigma}, c_{Jj\nu\sigma'}\} &= 0, \text{ and} \\ \{c_{Ii\mu\sigma}^\dagger, c_{Jj\nu\sigma'}\} &= \delta_{IJ}\delta_{ij}\delta_{\mu\nu}\delta_{\sigma\sigma'}. \end{aligned} \quad (2.1.7)$$

The parameters  $t_{\mu\nu}(\vec{R}_I + \vec{r}_i, \vec{R}_J + \vec{r}_j)$  are the matrix elements of Equation 2.1.5 in this basis,

$$t_{\mu\nu}(\vec{R}_I + \vec{r}_i, \vec{R}_J + \vec{r}_j) = \int d\vec{r} \phi_\mu^*(\vec{r} - \vec{R}_I - \vec{r}_i) \left( \frac{\vec{p}^2}{2} + \sum_{Kk} \hat{H}_{\text{ion}, k}(|\vec{r} - \vec{R}_K - \vec{r}_k|) \right) \phi_\nu(\vec{r} - \vec{R}_J - \vec{r}_j), \quad (2.1.8)$$

where  $\phi_\mu(\vec{r} - \vec{R}_I - \vec{r}_i)$  is the atomic wavefunction for orbital  $\mu$  at atomic site  $\vec{R}_I + \vec{r}_i$ . They are usually called hopping integrals as they are related to the probability of an electron moving from one site to another [26].

For periodic systems, the hopping integrals depend solely on the relative distance between the unit cells. Bloch's theorem states that in systems with a perfectly periodic potential the wavefunctions can be written as

$$\Psi_{n,\vec{k}}(\vec{r}) = u(\vec{r})e^{i\vec{k}\cdot\vec{r}} \quad (2.1.9)$$

where  $u(\vec{r})$  is a function with the same periodicity as the potential. The wave-like vector  $\vec{k}$  is confined to the first Brillouin Zone. Therefore, it is practical to transform the hopping integrals into reciprocal space where one has an integral over a compact region in contrast to an infinite sum. The transformation is achieved by rewriting the creation and annihilation operators in terms of their Fourier transformed counterparts.

$$\begin{aligned} c_{Ii\mu\sigma} &= \int_{\text{BZ}} d\vec{k} e^{i\vec{k}\cdot\vec{R}_I} c_{\vec{k}i\mu\sigma} \\ c_{Ii\mu\sigma}^\dagger &= \int_{\text{BZ}} d\vec{k} e^{-i\vec{k}\cdot\vec{R}_I} c_{\vec{k}i\mu\sigma}^\dagger, \end{aligned} \quad (2.1.10)$$

where the operator  $c_{\vec{k}i\mu\sigma}^\dagger$  ( $c_{\vec{k}i\mu\sigma}$ ) is the creation (annihilation) operator in reciprocal space that fullfills the commutation relations

$$\begin{aligned} \{c_{\vec{p}i\mu\sigma}^\dagger, c_{\vec{q}'j\nu\sigma'}^\dagger\} &= 0, \\ \{c_{\vec{p}i\mu\sigma}, c_{\vec{q}'j\nu\sigma'}\} &= 0, \text{ and} \\ \{c_{\vec{p}i\mu\sigma}^\dagger, c_{\vec{q}'j\nu\sigma'}\} &= \delta(\vec{p} - \vec{q}')\delta(\vec{r}_i - \vec{r}_j)\delta_{\mu\nu}\delta_{\sigma\sigma'}. \end{aligned} \quad (2.1.11)$$

With this the Hamiltonian can be written as

$$\hat{H}_{\text{Crystal}} = \sum_{ij} \sum_{\mu\nu} \sum_{\sigma} \int_{\text{BZ}} d\vec{k} t_{ij}^{\mu\nu}(\vec{k}) c_{k i \mu \sigma}^{\dagger} c_{k j \nu \sigma} \quad (2.1.12)$$

with

$$t_{ij}^{\mu\nu}(\vec{k}) = \sum_J t_{\mu\nu}(\vec{r}_i, \vec{R}_J + \vec{r}_j) e^{i\vec{k} \cdot \vec{R}_J}. \quad (2.1.13)$$

### 2.1.2. Tight-binding approximation

In the tight-binding approximation, the wavefunctions are described by a set of localized atomic-like functions that are limited to a small set of orbitals close to the Fermi level. This is in contrast to DFT calculations, where one usually tries to describe the full Hilbert space of an effective single particle system and thus has a large amount of basis functions. The tight-binding model is best suited to systems with well-localized wavefunctions that do not overlap too much with neighboring atoms. There exist several tight-binding models that differ in the amount of approximations made. However, they all have in common that they use a minimal local basis of atomic orbitals. Throughout this thesis, nine orbitals,  $\mu$ , per atomic site will be used, i.e. real spherical harmonics with orbital moments  $s$ ,  $p_x$ ,  $p_y$ ,  $p_z$ ,  $d_{xy}$ ,  $d_{yz}$ ,  $d_{zx}$ ,  $d_{x^2-y^2}$  and  $d_{3z^2-r^2}$ , Figure 2.1 shows their visual representation.

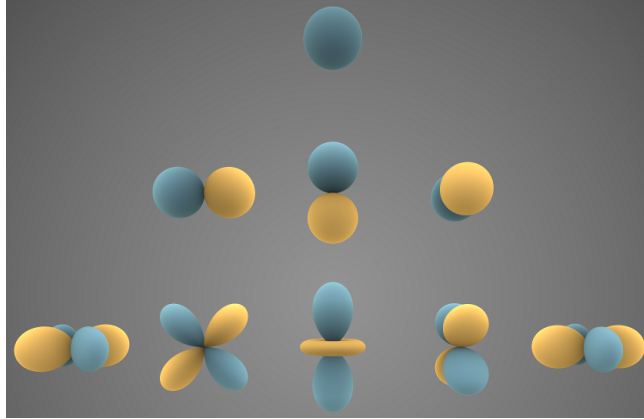


Figure 2.1.: Visual representation of real spherical harmonics for the orbitals:  $s$  (top),  $p_x$ ,  $p_z$ ,  $p_y$  (middle) and  $d_{xy}$ ,  $d_{zx}$ ,  $d_{3z^2-r^2}$ ,  $d_{yz}$ ,  $d_{x^2-y^2}$  (bottom). Image obtained from Ref. [27].

The hopping integrals, introduced in the previous section, can be grouped into three different types.

- On-site terms are obtained when both wavefunctions are at the same atomic site:

$$t_{\mu\nu}(\vec{r}_i, \vec{r}_i) = \int d\vec{r} \phi_{\mu}^*(\vec{r} - \vec{r}_i) \left( \frac{\hat{p}^2}{2} + \sum_j \hat{H}_{\text{ion}, j}(|\vec{r} - \vec{r}_j|) \right) \phi_{\nu}(\vec{r} - \vec{r}_i) \quad (2.1.14)$$

The vector  $\vec{R}_I$  has been omitted for simplicity.

- Two-center integrals are obtained for wavefunctions with  $i \neq j$  and the ion potential located on the same site as one of the wavefunctions:

$$t_{\mu\nu}(\vec{r}_i, \vec{r}_j) = \int d\vec{r} \phi_\mu^*(\vec{r} - \vec{r}_i) \left( \frac{\vec{p}^2}{2} + \hat{H}_{\text{ion}, i}(|\vec{r} - \vec{r}_i|) + \hat{H}_{\text{ion}, j}(|\vec{r} - \vec{r}_j|) \right) \phi_\nu(\vec{r} - \vec{r}_j) \quad (2.1.15)$$

- Three-center integrals are obtained for wavefunctions at different atomic sites and the ion potential at a third atomic site:

$$t_{\mu\nu}(\vec{r}_i, \vec{r}_j) = \int d\vec{r} \phi_\mu^*(\vec{r} - \vec{r}_i) \left( \frac{\vec{p}^2}{2} + \sum_{k \neq i, k \neq j} \hat{H}_{\text{ion}, k}(|\vec{r} - \vec{r}_k|) \right) \phi_\nu(\vec{r} - \vec{r}_j) \quad (2.1.16)$$

Since the wavefunctions are orthogonal and the Coulomb interaction decays as  $1/|\vec{r}|$ , the three-center integrals are much smaller than the on-site and two-center integrals.

From Equation 2.1.4, it is obvious that the hopping integrals will also become smaller with increasing distance  $|\vec{r}_i - \vec{r}_j|$ . Therefore, in tight-binding approximations only the first few nearest neighbors are taken into account and hopping integrals for distances larger than a certain cutoff are neglected [28].

### Slater-Koster parametrization

Instead of explicitly calculating the hopping integrals, they are parametrized and can be fitted to known results of a system, e.g. from more sophisticated first principles calculations. At first glance, for a nine orbital basis set this would mean fitting 81 parameters for each pair of atoms. Slater and Koster [29] introduced a method on how they can be obtained from known band structures and how to significantly reduce the amount of independent parameters. This was done by first removing the three-center integrals of the problem, which are significantly smaller than the on-site and two-center integrals and using the symmetries of the system, they arrive at a form which has just enough arbitrary constants to fit them to the high symmetry points of the band structure obtained with a given *ab initio* calculation.

Assuming a quantization axis that coincides with the vector  $\vec{r}_i - \vec{r}_j$  between two atomic sites, one can write an atomic orbital in terms of orbital functions with respect to that axis. For example, one could write an atomic  $d$  orbital as linear combination of  $d_\sigma$ ,  $d_\pi$  and  $d_\delta$  where  $\sigma$ ,  $\pi$  and  $\delta$  describe different types of covalent bonding with respect to the quantization axis. A  $\sigma$  bond has a single overlapping lobe, a  $\pi$  bond two overlapping lobes and a  $\delta$  bond four overlapping lobes (see Figure 2.2). In the case of  $p$  orbitals, given the quantization axis is along the  $z$ -axis, this means that  $p_z$ — $p_z$  has a  $\sigma$  bond,  $p_y$ — $p_y$  and  $p_x$ — $p_x$  have  $\pi$  bonds. As the wavefunctions for different angular momenta along the quantization axis are orthogonal, in Equation 2.1.15 only those integrals with covalent bonds will be non-zero. Only ten two-center integrals

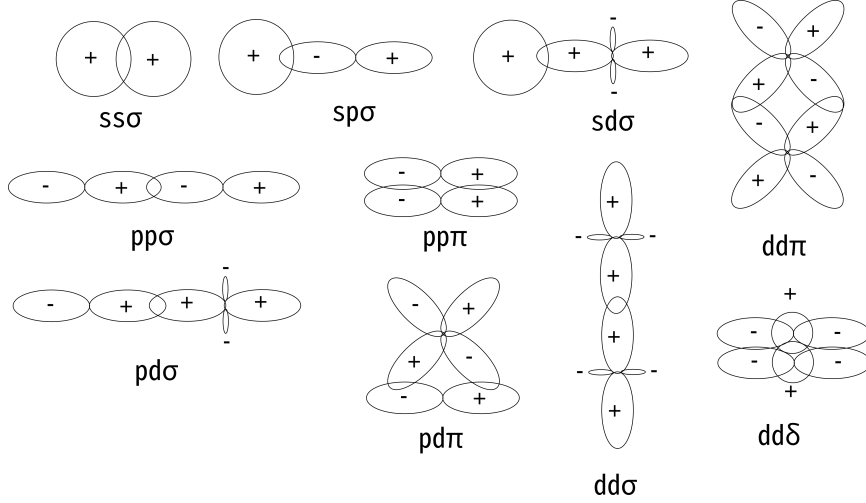


Figure 2.2.: This shows various  $s, p$  and  $d$  orbitals joined along a bond. Radial symmetry along the bond axis defines the type of bond as  $\sigma$ ,  $\pi$  or  $\delta$ .

remain:  $(ss\sigma)$ ,  $(pp\sigma)$ ,  $(pp\pi)$ ,  $(dd\sigma)$ ,  $(dd\pi)$ ,  $(dd\delta)$ ,  $(sp\sigma)$ ,  $(sd\sigma)$ ,  $(pd\sigma)$ ,  $(pd\pi)$ . The notation has to be read in the following way:

$$(sp\sigma) = \int d\vec{r} \phi_{s\sigma}^*(\vec{r} - \vec{r}_i) \left( \frac{\vec{p}^2}{2} + \hat{H}_{\text{ion}, i}(|\vec{r} - \vec{r}_i|) + \hat{H}_{\text{ion}, j}(|\vec{r} - \vec{r}_j|) \right) \phi_{p\sigma}(\vec{r} - \vec{r}_j) \quad (2.1.17)$$

Rotating back to the global cartesian coordinate system yields a general formula for the hopping matrix elements. As an example, the hopping between  $p_z$  and  $d_{xy}$  orbitals is given by

$$t_{p_z d_{xy}} = lmn (\sqrt{3}(pd\sigma) - 2(pd\pi)) . \quad (2.1.18)$$

Here,  $l, m$  and  $n$  denote the elements of the directional cosine of  $\vec{r}_i - \vec{r}_j$ . A full table containing all the elements for the hopping matrices is given in the publication of Slater and Koster [29].

### Mixing Scheme

Although the method proposed by Slater and Koster minimizes the amount of tight-binding parameters, they still increase quadratically with the amount of inequivalent atoms in the unit cell. Parameter sets for elemental bulk systems are smaller, easier and most importantly more available in the literature [22]. It is significantly harder to find parameters for compound materials with two or more inequivalent atoms in the unit cell. Here, an approximation for hopping between inequivalent atoms is proposed based on just elemental parameter sets. This basically consists in taking the geometric average of the hopping parameter for the two participating atoms. As an example, the averaged  $(ss\sigma)$  parameter for hopping between atom of element  $A$  and an atom of element  $B$  is calculated as the geometric average

$$(ss\sigma) = \text{sign} [(ss\sigma)_A + (ss\sigma)_B] \cdot \sqrt{|(ss\sigma)_A| \cdot |(ss\sigma)_B|} \quad (2.1.19)$$

which is preferable to the arithmetic average that could result in a vanishing hopping term.

### Andersen Scaling law

When computing structures for which the distance between atomic sites differs when compared to the original distances used for the calculation of the Slater-Koster parameters, the two-center integrals in Equation 2.1.15 and therefore the corresponding parameters will change. Following Andersen *et al.* [30], the distance dependence of Slater-Koster parameters for each pair of atomic sites can be written as

$$(l, l', m) = C_{ll'm} d^{-(l+l'+1)} \quad (2.1.20)$$

where  $d$  is the distance between the pair of atomic sites and  $C_{ll'm}$  is a material dependent constant which is independent of the volume. The indices  $l, l'$  describe again the orbital quantum number and  $m$  the type of bond ( $\sigma, \pi, \delta$ ). The new parameters can be obtained as

$$(l, l', m) = C_{ll'm} d^{-(l+l'+1)} = \left[ \frac{(l, l', m)_0}{d_0^{-(l+l'+1)}} \right] d^{-(l+l'+1)} \quad (2.1.21)$$

where  $(l, l', m)_0$  is the original Slater-Koster parameter obtained for atomic distance  $d_0$  and  $(l, l', m)$  is the scaled parameter for the new atomic distance. One can now identify an orbital dependent scaling factor  $\kappa$  as

$$\kappa_{ll'} = \left( \frac{d}{d_0} \right)^{-(l+l'+1)}. \quad (2.1.22)$$

Shore and Papaconstantopoulos [31] showed that for lattice constant variations of up to 3% this kind of scaling is in very good agreement with first principles augmented plane-wave calculations.

### 2.1.3. Coulomb interaction

The Coulomb interaction is a two particle operator, correlating all electrons of the system. In second quantization it can be written as

$$\hat{H}_{e-e} = \frac{1}{2} \sum_{\alpha\beta\gamma\delta} U_{\alpha\beta\delta\gamma} c_{\alpha}^{\dagger} c_{\beta}^{\dagger} c_{\gamma} c_{\delta} \quad (2.1.23)$$

where the matrix elements  $U_{\alpha\beta\delta\gamma}$  are given as

$$U_{\alpha\beta\delta\gamma} = \int d\vec{r} \int d\vec{r}' \phi_{\alpha}^*(\vec{r}) \phi_{\beta}^*(\vec{r}') \frac{1}{|\vec{r} - \vec{r}'|} \phi_{\delta}(\vec{r}') \phi_{\gamma}(\vec{r}). \quad (2.1.24)$$

The strength of this interaction depends on the relative distance,  $\vec{r} - \vec{r}'$ , between the pair of electrons. Thus, the strongest interactions are those between electrons on the

same atomic site. In the Hubbard model, one considers only the on-site interactions, neglecting the interaction of electrons on different atomic sites. Hubbard estimates that for  $3d$ -transition metals the strength of the interaction between electrons on next nearest neighbors is already an order of magnitude smaller than for electrons on the same site [32]. Additionally, for  $3d$ -transition metals, the  $d$ -orbitals are strongly localized and the  $s$  and  $p$  orbitals are strongly delocalized. It is thus a reasonable approximation to only consider interactions between electrons in the  $d$ -orbitals. Another reasonable approximation is parametrizing the matrix elements of the Coulomb interaction as  $U_{\alpha\beta\delta\gamma}^i = U^i \delta_{\alpha\gamma} \delta_{\beta\delta}$  as has been done implicitly by Löwde and Windsor in their study of the spin dynamics of nickel [33]. Using these, the contribution becomes

$$\hat{H}_{e-e} = \frac{1}{2} \sum_i \sum_{\mu\nu} \sum_{\sigma\sigma'} U^i c_{i\mu\sigma}^\dagger c_{i\nu\sigma'}^\dagger c_{i\mu\sigma'} c_{i\nu\sigma} . \quad (2.1.25)$$

The many-body problem is not exactly solvable, since the properties of each electron depend on all other electrons in the system. During the 1950s, it was shown that it is possible to describe the interaction of real particles through non-interacting quasiparticles moving in an effective field caused by the surrounding particles. When a real particle moves through the system it will repel its neighbors, thus dragging a cloud of electron holes with it. This cloud will screen the particle, weakening its interaction with other particles. These complex many-body interactions are substituted by an average field created by the other particles in the Hartree-Fock approximation, reducing the two-body operator to the one-body operator

$$c_\alpha^\dagger c_\beta^\dagger c_\gamma c_\zeta \rightarrow \langle c_\alpha^\dagger c_\zeta \rangle c_\beta^\dagger c_\gamma + \langle c_\beta^\dagger c_\gamma \rangle c_\alpha^\dagger c_\zeta - \langle c_\alpha^\dagger c_\gamma \rangle c_\beta^\dagger c_\zeta - \langle c_\beta^\dagger c_\zeta \rangle c_\alpha^\dagger c_\gamma . \quad (2.1.26)$$

In this approximation, the Coulomb interaction given in Equation 2.1.25 can be written as

$$\hat{H}_{e-e} = \sum_i \sum_{\sigma\sigma'} \sum_{\mu\nu} U^i \left( \langle c_{i\mu\sigma}^\dagger c_{i\nu\sigma} \rangle c_{i\nu\sigma'}^\dagger c_{i\mu\sigma'} - \langle c_{i\mu\sigma}^\dagger c_{i\mu\sigma'} \rangle c_{i\nu\sigma'}^\dagger c_{i\nu\sigma} \right) \quad (2.1.27)$$

Reordering of the indices results in

$$\hat{H}_{e-e} = \sum_i \sum_{\gamma\zeta} U^i \left( \sum_{\sigma'} \left[ \sum_{\sigma} \langle c_{i\zeta\sigma}^\dagger c_{i\gamma\sigma} \rangle - n_{\sigma'}^i \delta_{\gamma\zeta} \right] c_{i\gamma\sigma'}^\dagger c_{i\zeta\sigma'} - m_i^+ c_{i\gamma\downarrow}^\dagger c_{i\zeta\uparrow} \delta_{\gamma\zeta} - m_i^- c_{i\gamma\uparrow}^\dagger c_{i\zeta\downarrow} \delta_{\gamma\zeta} \right) \quad (2.1.28)$$

where  $n_\sigma^i = \sum_\mu \langle c_{i\mu\sigma}^\dagger c_{i\mu\sigma} \rangle$  is the electronic occupation of site  $i$  with spin  $\sigma$ , and  $m^+$  is the circular component of the magnetization, related to the expectation value of the spin raising operator  $\hat{S}^+$  as

$$m_i^+ = 2 \langle S_i^+ \rangle = 2 \sum_\mu \langle c_{i\mu\uparrow}^\dagger c_{i\mu\downarrow} \rangle \quad (2.1.29)$$

with  $S^+ = S^x + iS^y$  in cartesian coordinates. It is convenient to rewrite this equation in term of charge and magnetization densities as

$$\hat{H}_{e-e} = \sum_{ij} \sum_{\gamma\zeta} \sum_{\sigma\sigma'} W_{ij,\gamma\zeta}^{\sigma\sigma'} c_{i\gamma\sigma}^\dagger c_{i\zeta\sigma'} \quad (2.1.30)$$

with

$$W_{ij,\gamma\zeta}^{\sigma\sigma'} = \frac{U^i}{2} \delta_{ij} \left( \left[ 2 \sum_{\sigma''} \langle c_{i\zeta\sigma''}^\dagger c_{i\gamma\sigma''} \rangle - n^i \delta_{\gamma\zeta} \mp m_z^i \delta_{\gamma\zeta} \right] \delta_{\sigma\sigma'} - m_i^+ \delta_{\sigma\downarrow} \delta_{\sigma'\uparrow} \delta_{\gamma\zeta} - m_i^- \delta_{\sigma\uparrow} \delta_{\sigma'\downarrow} \delta_{\gamma\zeta} \right) \quad (2.1.31)$$

where the sign  $- (+)$  is taken for  $\sigma = \uparrow (\downarrow)$ .

The hopping parameters, described in the previous section, are obtained by fitting band structures of DFT calculations. Therefore, the Coulomb interaction will already be imprinted into these parameters. However, a change to the system can change its ground state and will subsequently change the Coulomb contribution from the value that is imprinted on the hopping parameters. This can be accounted for by self-consistent calculations of the spin and charge densities (see section 3.5).

#### 2.1.4. Zeeman interaction

An external magnetic field,  $\vec{B}$ , can be used to not only alter magnetic states, but in the presence of spin-orbit interaction also to manipulate currents through the magnetoresistance and Hall effects [25]. It couples to both spin,  $\vec{S}$ , and orbital,  $\vec{L}$ , degrees of freedom as

$$\begin{aligned} \hat{H}_{ZS} &= \sum_{i\mu} \sum_{\sigma_1\sigma_2} \mu_B g_S (\vec{S}_{\sigma_1\sigma_2} \cdot \vec{B}) c_{i\mu\sigma_1}^\dagger c_{i\mu\sigma_2} \\ \hat{H}_{ZL} &= \sum_{i\sigma} \sum_{\mu\nu} \mu_B g_L (\vec{L}_{\mu\nu} \cdot \vec{B}) c_{i\mu\sigma}^\dagger c_{i\nu\sigma} \end{aligned} \quad (2.1.32)$$

where  $\mu_B$  is the Bohr magneton,  $g_S$  and  $g_L$  are the Landé factors for spin and orbital angular momentum, respectively.

#### 2.1.5. Spin-orbit interaction

The spin-orbit interaction is a relativistic correction to the non-relativistic Schrödinger equation, obtained from the relativistic Dirac equation in the low velocity limit, coupling spin and orbital degrees of freedom

$$\hat{H}_{SO} = \sum_i \sum_{\mu\nu} \sum_{\sigma_1\sigma_2} \lambda_i \vec{S}_{\sigma_1\sigma_2} \cdot \vec{L}_{\mu\nu} c_{i\mu\sigma_1}^\dagger c_{i\nu\sigma_2} . \quad (2.1.33)$$

Here, the spin-orbit coupling parameters  $\lambda_i$  can be obtained from first principles calculations [34] by taking the expectation value of

$$\xi(\vec{r}) = \langle n, l | \frac{1}{2m^2c^2} \frac{1}{r} \frac{dV}{dr} | n, l \rangle \quad (2.1.34)$$

where  $\lambda_{i,n,l} = \langle i, n, l | \xi(\vec{r}) | i, n, l \rangle$  is only taken for the  $d$  orbitals ( $l = 2$ ) in the so-far investigated systems within this thesis. The spin-orbit coupling of the remaining orbitals is neglected.

One effect, that arises due to the spin-orbit interaction is the magnetic anisotropy. Under influence of an external magnetic field, the spin moments will try to re-orient themselves towards the field. But, the orbital moments are fixed in their orientation as they are strongly coupled to the crystal lattice and will resist attempts to re-orient towards the field. As the spin-orbit interaction connects their degrees of freedom, there will be a resistance to re-orient the spin moments. The energy needed to overcome this barrier is called the magnetic anisotropy energy (MAE) and depends on the orientation of the field with respect to the orbital moments. Certain orientation will minimize the MAE and are usually called easy axes, whereas orientations that maximize the MAE are called hard axes.

Other effects caused by spin-orbit interaction are the spin Hall and inverse spin Hall effect, which arises due to coupling of charge and spin currents of the system. The spin Hall effect describes the accumulation of opposing spin moments at opposing surfaces of the system due to an applied current. The manipulation of charge currents through magnetic fields is described by the inverse spin Hall effect.

There are more effects caused by the spin-orbit interaction, such as dissipative effects described in chapter 5.

## 2.2. Ground state properties

Observables are measurable quantities of a system. They can be used to compare the model described in the previous section with experimental results and other, more elaborate theoretical models which makes it possible to quantify the accuracy of the model.

These observables can be obtained by making use of mathematical objects called Green functions. In general, Green functions can be defined as solutions of inhomogeneous differential equations of the type

$$(z - \mathcal{L}(\vec{r})) G(\vec{r}, \vec{r}', z) = \delta(\vec{r} - \vec{r}') . \quad (2.2.1)$$

Therefore, for the Schrödinger equation, the Green function can be written in matrix notation as

$$G(E) = (E - \hat{H})^{-1} \quad (2.2.2)$$

In the second quantization formalism, the Green function can be written as

$$G_{\alpha\beta}(t, t') = \langle \mathcal{T} c_{\alpha}(t) c_{\beta}^{\dagger}(t') \rangle \quad (2.2.3)$$

with  $\mathcal{T}$  being the time-ordering operator. For a time-independent Hamiltonian the Green function only depends on the time difference  $\tau = t - t'$

$$G_{\alpha\beta}(\tau) = \langle \mathcal{T} c_{\alpha}(\tau) c_{\beta}^{\dagger}(0) \rangle . \quad (2.2.4)$$

Thus one can define the retarded and advanced Green functions as

$$\begin{aligned} G_{\alpha\beta}^r(t) &= -i\Theta(t)\langle \{c_{\alpha}(t), c_{\beta}^{\dagger}\} \rangle \\ G_{\alpha\beta}^a(t) &= i\Theta(-t)\langle \{c_{\alpha}^{\dagger}(t), c_{\beta}\} \rangle \end{aligned} \quad (2.2.5)$$

which play an important role in the calculation of observables. In the frequency domain, they can be written in matrix notation as [35]

$$G^{r/a}(E) = \lim_{\eta \rightarrow 0^+} (E - \hat{H} \pm i\eta)^{-1} \quad (2.2.6)$$

where the positive (negative) sign is used for the retarded (advanced) Green function. The parameter  $\eta$  is necessary for the function to be integrable. This artificial broadening will later be used to mimic disorder of the system through temperature.

The spectral representation of the retarded (advanced) Green function is given as

$$G^{r/a}(E) = \lim_{\eta \rightarrow 0^+} \sum_n \frac{|n\rangle\langle n|}{E - \epsilon_n \pm i\eta}, \quad (2.2.7)$$

where  $|n\rangle$  are the eigenstates of the Hamiltonian  $\hat{H}$ . The expectation value of an observable in the ground state is given as

$$\langle \hat{A} \rangle = -\frac{1}{\pi} \text{Im} \int_{-\infty}^{\infty} dE f_F(E) \text{Tr} [G^r(E) \hat{A}] \quad (2.2.8)$$

where  $f_F$  is the Fermi-Dirac distribution, which at zero temperature is the Heaviside step function  $\Theta(\epsilon_F - E)$ .

### 2.2.1. Band structure

From the band structure one can obtain insight about the available energy states,  $\epsilon_{\vec{k}\mu\sigma}$ , of an electronic system in the form of continuous bands in reciprocal space. At zero temperature, all states with energy smaller than the Fermi level,  $\epsilon_F$ , are occupied. The band energies are obtained by calculating the eigenvalue problem for the  $\vec{k}$ -dependent Hamiltonian.

$$\hat{H}(\vec{k})|\phi_{\mu\sigma}(\vec{k})\rangle = \epsilon_{\vec{k}\mu\sigma}|\phi_{\mu\sigma}(\vec{k})\rangle. \quad (2.2.9)$$

When a band crosses the Fermi level, it means that there are available states with very small energy above the ground state. Therefore, it is easy to accelerate and transport the electrons, as is in the case of metals. When there are no partially filled bands and the gap between the lowest band above and the highest band below the Fermi level is large, the system is insulating. For cases where there is no crossing of the Fermi level but the band gap is so small that it allows thermal excitations, the system is called a semiconductor.

### 2.2.2. Density of states

The density of states is a measure for the amount of electronic states present for a given energy. One can define an energy dependent operator by summing over all states with the given energy,

$$\hat{D}(E) = \sum_n |n\rangle\delta(E - \epsilon_n)\langle n|. \quad (2.2.10)$$

The local density of states is then given as the trace over spin and orbital space of this operator,

$$D(E) = \text{Tr} \hat{D}(E) . \quad (2.2.11)$$

The total electron occupation is obtained by integrating the density of states weighted by the Fermi-Dirac distribution  $f_F$ .

$$N = \int_{-\infty}^{\infty} dE f_F(E) D(E) \quad (2.2.12)$$

Using Dirac's identity,

$$\delta(E - \epsilon_n) = -\frac{1}{\pi} \lim_{\eta \rightarrow 0^+} \text{Im} \frac{1}{E - \epsilon_n + i\eta} \quad (2.2.13)$$

the density of states operator becomes

$$\hat{D}(E) = -\frac{1}{\pi} \lim_{\eta \rightarrow 0^+} \text{Im} \sum_n \frac{|n\rangle\langle n|}{E - \epsilon_n + i\eta} . \quad (2.2.14)$$

This can be written in terms of Green functions by identifying its spectral representation given by Equation 2.2.7 as

$$\hat{D}(E) = -\frac{1}{\pi} \lim_{\eta \rightarrow 0^+} \text{Im} \hat{G}^r(E + i\eta) . \quad (2.2.15)$$

As a generalization, the local density of states can be obtained by taking the site-dependent Green function  $G_{ii}$

$$\hat{D}_i(E) = -\frac{1}{\pi} \lim_{\eta \rightarrow 0^+} \text{Im} \hat{G}_{ii}^r(E + i\eta) \quad (2.2.16)$$

which besides giving information on the local electronic structure, is useful for example to understand charge or spin accumulations due to the spin Hall effect.

### 2.2.3. Magnetization and Stoner criterion

The spin magnetic moment for an atomic site is defined as the expectation value of the spin operator. The magnetic moments  $\vec{m}$  as well as the charge density  $n$  can be obtained from the Green function as

$$\begin{pmatrix} n_i \\ \vec{m}_i \end{pmatrix} = \left\langle \begin{pmatrix} \rho_i \\ 2\vec{S}_i \end{pmatrix} \right\rangle = -\frac{1}{\pi} \lim_{\eta \rightarrow 0^+} \text{Im} \int_{-\infty}^{\epsilon_F} dE \int_{\text{BZ}} d\vec{k} \text{Tr} \left[ \begin{pmatrix} \sigma_0 \\ \vec{\sigma} \end{pmatrix} \hat{G}_{ii}(E + i\eta, \vec{k}) \right] \quad (2.2.17)$$

where  $\sigma_0$  is the  $2 \times 2$  identity matrix and  $\vec{\sigma}$  are the Pauli matrices

$$\sigma_0 = \begin{pmatrix} 1 & 0 \\ 0 & 1 \end{pmatrix}, \quad \sigma_x = \begin{pmatrix} 0 & 1 \\ 1 & 0 \end{pmatrix}, \quad \sigma_y = \begin{pmatrix} 0 & -i \\ i & 0 \end{pmatrix}, \quad \sigma_z = \begin{pmatrix} 1 & 0 \\ 0 & -1 \end{pmatrix} . \quad (2.2.18)$$

In 1938, Stoner [36] derived a simple criterion for bulk systems to determine whether a material has a paramagnetic unstable ground state or not. In the Hubbard model, this Stoner criterion is given by

$$D(\epsilon_F)U > 1 \quad (2.2.19)$$

where  $U$  is as given in Equation 2.1.25 and  $D(\epsilon_F)$  the local density of states at the Fermi level.

## 2.3. Dynamical properties

There exist countless situations where one is interested in how an electronic system responds to external time-dependent perturbations. Especially the case of small perturbations, such as external electromagnetic fields that usually have energies much smaller than the energy difference between two bands, is used to experimentally probe a system without changing its state. A counter example to this are high fluence lasers which have much higher energies than can cause non-linear excitations, and effects beyond the adiabatic regime, such as ultrafast demagnetization. The time-evolution of observables for small perturbations are obtained through linear response functions [23].

### 2.3.1. Linear response formalism

For a system described by the time-independent Hamiltonian  $\hat{H}$ , which is acted upon by an external field  $f(\vec{r}, t)$  that couples to a physical quantity described by the operator  $\hat{B}$ , the Hamiltonian can be written as

$$\hat{H}_f(t) = \hat{H} + \int d\vec{r} \hat{B}(\vec{r}, t) f(\vec{r}, t) \quad (2.3.1)$$

At some time  $t_0$  the external field is turned on. Before that, the system is at the equilibrium ground state  $|\psi_0\rangle$

$$\hat{H}|\psi_0\rangle = E_0|\psi_0\rangle . \quad (2.3.2)$$

After turning on the field, the time evolution of the system is determined by the time-dependent Schrödinger equation

$$i \frac{\partial}{\partial t} |\psi(t)\rangle = \hat{H}_f(t) |\psi(t)\rangle \quad (2.3.3)$$

with the eigenstates of the system evolving as

$$|\psi(t)\rangle = \hat{U}(t, t_0) |\psi_0\rangle . \quad (2.3.4)$$

as given by the time evolution operator

$$\hat{U}(t, t') = \exp \left( -i \int_{t'}^t d\tau \hat{H}_f(\tau) \right) \quad (2.3.5)$$

which describes the change of the eigenstates from time  $t'$  to  $t$ . It can be split into the time-independent part of the Hamiltonian

$$\hat{U}_0(t, t') = e^{-i\hat{H}(t-t')} \quad (2.3.6)$$

and the time-dependent part which expanded up to first order in the perturbation field can be written as

$$\hat{U}_f(t, t') \approx \hat{1} - i \int_{t'}^t d\tau \int d\vec{r} \hat{B}(\vec{r}, \tau - t') f(\vec{r}, \tau) \quad (2.3.7)$$

With this, the change in the expectation value due to the time-dependent field is given by

$$\delta\langle A(\vec{r}, t) \rangle = \langle \hat{A}(\vec{r}, t) \rangle - \langle \hat{A}(\vec{r}) \rangle_0 = -i \int_{t_0}^t dt' \int d\vec{r}' \langle [\hat{A}(\vec{r}, t), \hat{B}(\vec{r}', t')] \rangle_0 f(\vec{r}', t') \quad (2.3.8)$$

where  $\langle \dots \rangle_0$  is the equilibrium expectation value. Using the time-independence and translational symmetry of the unperturbed Hamiltonian, one can write

$$\delta\langle \hat{A}(\vec{r}, t) \rangle = -i \int_{t_0}^t dt' \int d\vec{r}' \langle [\hat{A}(\vec{r} - \vec{r}', t - t'), \hat{B}] \rangle_0 f(\vec{r}', t') \quad (2.3.9)$$

Here, one can define the general response of an observable  $\hat{A}$  induced by a perturbation which couples to the observable  $\hat{B}$  as

$$\chi_{\hat{A}\hat{B}}(\vec{r}, t) = \langle \langle \hat{A}(\vec{r}, t), \hat{B} \rangle \rangle = -i\Theta(t) \langle [\hat{A}(\vec{r}, t), \hat{B}] \rangle_0 . \quad (2.3.10)$$

Using this, the change in the expectation value of an observable can be written as

$$\delta\langle A(\vec{r}, t) \rangle = \int dt' \int d\vec{r}' \chi_{\hat{A}\hat{B}}(\vec{r} - \vec{r}', t - t') f(\vec{r}', t') . \quad (2.3.11)$$

Taking the Fourier transform, this equation takes on a linear form

$$\delta\langle A(\vec{q}, \omega) \rangle = \chi_{\hat{A}\hat{B}}(\vec{q}, \omega) f(\vec{q}, \omega) \quad (2.3.12)$$

which shows that, in linear response, there is no mixing between frequencies or momenta. In this thesis, only uniform fields will be considered, i.e.,  $f(\vec{q} = 0, \omega)$ .

Equation 2.3.10 describes the after effect of turning on a perturbation, it is usually called the retarded response function. The causality is ensured by use of the Heaviside step function  $\Theta(t)$ .

One can write the response function in second quantization as

$$\chi_{\hat{A}\hat{B}}(t) = \sum_{\alpha\beta\gamma\delta} A_{\alpha\beta}(t) \chi_{\alpha\beta\gamma\delta}(t) B_{\gamma\delta} \quad (2.3.13)$$

where the simplified notation  $\alpha = \{i, I, \mu, \sigma_1\}$  was used.  $\chi_{\alpha\beta\gamma\delta}(t)$  is the general function that can be used to build the response of a given operator to any type of field and is given by

$$\chi_{\alpha\beta\gamma\delta}(t) = -i\Theta(t)\langle [c_\alpha^\dagger(t)c_\beta(t), c_\gamma^\dagger c_\delta] \rangle. \quad (2.3.14)$$

This general response has the advantage that, once calculated, can be used for a multitude of different operator responses, such as spin–spin or spin–orbital momentum responses.

### 2.3.2. Mean field approximation

The calculation of the response function for the full Hamiltonian, including the two-body Coulomb interaction, is not possible. Starting from the single-particle picture with the Coulomb interaction in the Hartree-Fock approximation, it is possible to write the response function in terms of single-particle non-interacting Green functions. Using Wick's theorem [37] on Equation 2.3.14, one obtains

$$\chi_{\alpha\beta\gamma\delta}(t) = -i\Theta(t) [\langle c_\alpha^\dagger(t)c_\delta \rangle \langle c_\beta(t)c_\gamma^\dagger \rangle - \langle c_\gamma^\dagger c_\beta(t) \rangle \langle c_\delta c_\alpha^\dagger(t) \rangle] \quad (2.3.15)$$

Reordering of the terms results in

$$\chi_{\alpha\beta\gamma\delta}(t) = -i\Theta(t) [\langle c_\alpha^\dagger(t)c_\delta \rangle \langle \{c_\beta(t), c_\gamma^\dagger\} \rangle - \langle c_\gamma^\dagger c_\beta(t) \rangle \langle \{c_\alpha^\dagger(t), c_\delta\} \rangle] \quad (2.3.16)$$

where one can identify the retarded and advanced Green functions (see Equation 2.2.5)

$$\chi_{\alpha\beta\gamma\delta}(t) = G_{\beta\gamma}^r(t) \langle c_\alpha^\dagger(t)c_\delta \rangle - G_{\alpha\delta}^a(t) \langle c_\gamma^\dagger c_\beta(t) \rangle. \quad (2.3.17)$$

The remaining expectation values can be written in terms of the retarded and advanced Green function [38] as

$$\begin{aligned} \langle c_\alpha^\dagger(t)c_\delta \rangle &= -\frac{i}{2\pi} \int d\omega' f_F(\omega) e^{i\omega't} [G_{\delta\alpha}^r(\omega') - G_{\delta\alpha}^a(\omega')] \\ \langle c_\gamma^\dagger c_\beta(t) \rangle &= \frac{i}{2\pi} \int d\omega' f_F(\omega) e^{-i\omega't} [G_{\beta\gamma}^r(\omega') - G_{\beta\gamma}^a(\omega')] \end{aligned} \quad (2.3.18)$$

The Fourier transform of the response function is then given as

$$\begin{aligned} \chi_{\alpha\beta\gamma\delta}(\omega) &= \frac{i}{2\pi} \int dt \int d\omega' f_F(\omega') G_{\beta\gamma}^r(t) e^{i(\omega+\omega')t} [G_{\delta\alpha}^a(\omega') - G_{\delta\alpha}^r(\omega')] \\ &\quad - G_{\alpha\delta}^a(t) e^{i(\omega-\omega')t} [G_{\beta\gamma}^r(\omega') - G_{\beta\gamma}^a(\omega')] . \\ &= \frac{i}{2\pi} \int d\omega' f_F(\omega') G_{\beta\gamma}^r(\omega + \omega') [G_{\delta\alpha}^r(\omega') - G_{\delta\alpha}^a(\omega')] \\ &\quad + G_{\alpha\delta}^a(\omega' - \omega) [G_{\beta\gamma}^r(\omega') - G_{\beta\gamma}^a(\omega')] \end{aligned} \quad (2.3.19)$$

which using the Fermi-Dirac distribution for  $T = 0$  K can be written as

$$\begin{aligned} \chi_{\alpha\beta\gamma\delta}(\omega) &= \frac{i}{2\pi} \int_{-\infty}^{\epsilon_F} d\omega' \left[ G_{\beta\gamma}^r(\omega + \omega') G_{\delta\alpha}^r(\omega') - G_{\alpha\delta}^a(\omega') G_{\beta\gamma}^a(\omega' + \omega) \right] \\ &\quad - \frac{i}{2\pi} \int_{\epsilon_F - \omega}^{\epsilon_F} d\omega' G_{\alpha\delta}^a(\omega') \left[ G_{\beta\gamma}^r(\omega + \omega') - G_{\beta\gamma}^a(\omega' + \omega) \right]. \end{aligned} \quad (2.3.20)$$

With the relation  $G_{\alpha\beta}^a(\omega) = [G_{\beta\alpha}^r(\omega)]^*$  the integrals can be written as

$$\begin{aligned} \chi_{\alpha\beta\gamma\delta}(\omega) = & \frac{i}{2\pi} \int_{-\infty}^{\epsilon_F} d\omega' \left( G_{\beta\gamma}^r(\omega + \omega') G_{\delta\alpha}^r(\omega') - [G_{\delta\alpha}^r(\omega') G_{\gamma\beta}^r(\omega' + \omega)]^* \right) \\ & - \frac{i}{2\pi} \int_{\epsilon_F - \omega}^{\epsilon_F} d\omega' [G_{\delta\alpha}^r(\omega')]^* \left( G_{\beta\gamma}^r(\omega + \omega') - [G_{\gamma\beta}^r(\omega' + \omega)]^* \right) \end{aligned} \quad (2.3.21)$$

For extended systems, one can Fourier transform the unit cell index  $I$  to reciprocal space to obtain

$$\begin{aligned} \chi_{\alpha\beta\gamma\delta}(\omega, \vec{q}) = & \frac{i}{2\pi} \int_{\text{BZ}} d\vec{k} \int_{-\infty}^{\epsilon_F} d\omega' \left( G_{\beta\gamma}^r(\omega + \omega', \vec{q} + \vec{k}) G_{\delta\alpha}^r(\omega', \vec{k}) \right. \\ & \left. - [G_{\delta\alpha}^r(\omega', \vec{k}) G_{\gamma\beta}^r(\omega' + \omega, \vec{q} + \vec{k})]^* \right) \\ & - \frac{i}{2\pi} \int_{\text{BZ}} d\vec{k} \int_{\epsilon_F - \omega}^{\epsilon_F} d\omega' [G_{\delta\alpha}^r(\omega', \vec{k})]^* \left( G_{\beta\gamma}^r(\omega + \omega', \vec{q} + \vec{k}) \right. \\ & \left. - [G_{\gamma\beta}^r(\omega' + \omega, \vec{q} + \vec{k})]^* \right) \end{aligned} \quad (2.3.22)$$

Thus, the response function within the mean-field approximation is given by a product of two single-particle retarded Green functions.

### 2.3.3. Random phase approximation

The mean-field response describes the response of each electron as an independent particle moving in an average field generated by all other electrons. Even though the electrons feel the potential generated by the others, there is no correlation between the electrons in the system. It describes only the one-electron dynamics, where there are only electron-hole excitations (spin-flip).

Most physical systems also have long-lived collective excitations that do not change the number of particles, such as spin waves [39], which are much lower in energy than single particle excitations, such as spin flips [40]. To describe such collective modes the particles must be correlated, since they are not captured by a mean-field single particle picture.

One of the best known approximation to include correlations is the random phase approximation (RPA) [41]. The correlations due to the Coulomb interaction are added as a self-energy term to the mean-field response by use of the Dyson equation [42]

$$\chi = \chi_0 + \chi_0 U \chi \quad (2.3.23)$$

where  $\chi_0$  is the mean-field response function,  $\chi$  the interacting response function in RPA and  $U$  is as given in Equation 2.1.25. The mean-field as well as the RPA response

function, as well as the Coulomb interaction are given as matrices in site, spin and orbital spaces. Care has to be taken for the repulsive Coulomb interaction, as the matrix  $U$  is only non-zero for the  $d$ -orbital block.

The RPA response function is calculated by first setting up the tight-binding Hamiltonian, Equation 2.1.3, afterwards one obtains the Green function, Equation 2.2.6, by inversion of the Hamiltonian, then one calculates the mean-field response function, Equation 2.3.22, and lastly from Equation 2.3.23 the final result is obtained.

### 2.3.4. Magnetic perturbations

Now that the framework is laid out, it will now be particularized to the case of magnetic excitations. Here, this is done by using a circular polarized magnetic field,  $\vec{b}(t) = b_0[\cos(\omega t)\vec{e}'_x - \sin(\omega t)\vec{e}'_y]$ , transversal to the quantization directions of the spin moments,  $\vec{e}_z$ . The time-dependent perturbation that couples to spin and orbital degrees of freedom can be written in real space as

$$\begin{aligned}\hat{H}_{\text{int}} &= \mu_B(g_S\vec{S} + g_L\vec{L}) \cdot \vec{b}(t) \\ &= \frac{\mu_B b_0}{2} \sum_{ij} \sum_{\mu\nu} \sum_{\sigma\sigma'} \left( g_S \delta_{\mu\nu} [e^{i\omega t} S^{+\sigma\sigma'} + e^{-i\omega t} S^{-\sigma\sigma'}] \right. \\ &\quad \left. + g_L \delta_{\sigma\sigma'} [e^{i\omega t} L'^+_{\mu\nu} + e^{-i\omega t} L'^-_{\mu\nu}] \right) \delta_{ij} c_{i\mu\sigma}^\dagger c_{j\nu\sigma'} \\ &= H_{\text{int,S}} + H_{\text{int,L}}\end{aligned}\tag{2.3.24}$$

where  $L'^\mu$  represents the orbital momenta along the spin quantization axis, and its circular components are given by

$$\begin{aligned}L'^- &= L^x[\cos(\theta)\cos(\phi) + i\sin(\phi)] + L^y[\cos(\theta)\sin(\phi) - i\sin(\phi)] - L^z\sin(\theta) \\ L'^+ &= L^x[\cos(\theta)\cos(\phi) - i\sin(\phi)] + L^y[\cos(\theta)\sin(\phi) + i\sin(\phi)] - L^z\sin(\theta)\end{aligned}\tag{2.3.25}$$

with  $\theta$  and  $\phi$  being the spherical polar and azimuthal angles of the equilibrium spin moments, respectively.

The change in  $m$ -th component of the spin density at site  $i$  due to the external magnetic field coupled to the spin of all atomic sites is given by Equation 2.3.11 as

$$\begin{aligned}\delta\langle S_i^m \rangle(t) &= -i \int dt' \Theta(t-t') \langle [S_i^m(t), \hat{H}_{\text{int,S}}(t')] \rangle \\ &= \frac{\mu_B b_0 g_S}{2} \sum_l \sum_{\mu\gamma} \sum_{\sigma_1\sigma_2} \int dt' S^{m\sigma_1\sigma_2} [e^{i\omega t'} S^{+\sigma_3\sigma_4} + e^{-i\omega t'} S^{-\sigma_3\sigma_4}] \chi_{i\text{ill},\mu\mu\gamma\gamma}^{\sigma_1\sigma_2\sigma_3\sigma_4}(t-t') \\ &= \frac{\mu_B b_0 g_S}{2} \sum_{l,\mu\gamma} \sum_{\sigma_1\sigma_2} S^{m\sigma_1\sigma_2} [e^{i\omega t} \chi_{i\text{ill},\mu\mu\gamma\gamma}^{\sigma_1\sigma_2\uparrow\downarrow}(-\omega) + e^{-i\omega t} \chi_{i\text{ill},\mu\mu\gamma\gamma}^{\sigma_1\sigma_2\downarrow\uparrow}(\omega)]\end{aligned}\tag{2.3.26}$$

Using that  $[\chi_{\alpha\beta\gamma\delta}(\omega)]^* = \chi_{\beta\alpha\delta\gamma}(-\omega)$ , one can write

$$\delta\langle S_i^m \rangle(t) = \frac{\mu_B b_0 g_S}{2} \sum_{l,\mu\gamma} \sum_{\sigma_1\sigma_2} S^{m\sigma_1\sigma_2} [e^{i\omega t} [\chi_{i\text{ill},\mu\mu\gamma\gamma}^{\sigma_2\sigma_1\downarrow\uparrow}(\omega)]^* + e^{-i\omega t} \chi_{i\text{ill},\mu\mu\gamma\gamma}^{\sigma_1\sigma_2\downarrow\uparrow}(\omega)]\tag{2.3.27}$$

The change in the x-component of the spin operator is given by

$$\begin{aligned}
 \delta\langle S_i^x \rangle(t) &= -i \int dt' \Theta(t-t') \langle [S_i^x(t), \hat{H}_{\text{int,S}}(t')] \rangle \\
 &= \frac{\mu_B b_0 g_S}{4} \sum_{l,\mu\gamma} \sum_{\sigma_1\sigma_2} (\delta_{\sigma_1\uparrow}\delta_{\sigma_2\downarrow} + \delta_{\sigma_1\downarrow}\delta_{\sigma_2\uparrow}) [e^{i\omega t} [\chi_{i\text{ill},\mu\mu\gamma\gamma}^{\sigma_2\sigma_1\downarrow\uparrow}(\omega)]^* + e^{-i\omega t} \chi_{i\text{ill},\mu\mu\gamma\gamma}^{\sigma_1\sigma_2\downarrow\uparrow}(\omega)] \\
 &= \frac{\mu_B b_0 g_S}{4} \sum_{l,\mu\gamma} e^{i\omega t} ([\chi_{i\text{ill},\mu\mu\gamma\gamma}^{\downarrow\uparrow\downarrow\uparrow}(\omega)]^* + [\chi_{i\text{ill},\mu\mu\gamma\gamma}^{\uparrow\downarrow\uparrow\downarrow}(\omega)]^*) \\
 &\quad + e^{-i\omega t} (\chi_{i\text{ill},\mu\mu\gamma\gamma}^{\downarrow\uparrow\downarrow\uparrow}(\omega) + \chi_{i\text{ill},\mu\mu\gamma\gamma}^{\uparrow\downarrow\uparrow\downarrow}(\omega)) \\
 &= \frac{\mu_B b_0 g_S}{2} \sum_{l,\mu\gamma} \text{Re} \left[ e^{i\omega t} [\chi_{i\text{ill},\mu\mu\gamma\gamma}^{\downarrow\uparrow\downarrow\uparrow}(\omega)]^* + e^{-i\omega t} \chi_{i\text{ill},\mu\mu\gamma\gamma}^{\uparrow\downarrow\uparrow\downarrow}(\omega) \right]
 \end{aligned} \tag{2.3.28}$$

The change in the y-component is given by

$$\begin{aligned}
 \delta\langle S_i^y \rangle(t) &= -i \int dt' \Theta(t-t') \langle [S_i^y(t), \hat{H}_{\text{int,S}}(t')] \rangle \\
 &= \frac{\mu_B b_0 g_S}{4} \sum_{l,\mu\gamma} \sum_{\sigma_1\sigma_2} i(-\delta_{\sigma_1\uparrow}\delta_{\sigma_2\downarrow} + \delta_{\sigma_1\downarrow}\delta_{\sigma_2\uparrow}) [e^{i\omega t} [\chi_{i\text{ill},\mu\mu\gamma\gamma}^{\sigma_2\sigma_1\downarrow\uparrow}(\omega)]^* + e^{-i\omega t} \chi_{i\text{ill},\mu\mu\gamma\gamma}^{\sigma_1\sigma_2\downarrow\uparrow}(\omega)] \\
 &= \frac{i\mu_B b_0 g_S}{4} \sum_{l,\mu\gamma} e^{i\omega t} (-[\chi_{i\text{ill},\mu\mu\gamma\gamma}^{\downarrow\uparrow\downarrow\uparrow}(\omega)]^* + [\chi_{i\text{ill},\mu\mu\gamma\gamma}^{\uparrow\downarrow\uparrow\downarrow}(\omega)]^*) \\
 &\quad + e^{-i\omega t} (-\chi_{i\text{ill},\mu\mu\gamma\gamma}^{\downarrow\uparrow\downarrow\uparrow}(\omega) + \chi_{i\text{ill},\mu\mu\gamma\gamma}^{\uparrow\downarrow\uparrow\downarrow}(\omega)) \\
 &= \frac{\mu_B b_0 g_S}{2} \sum_{l,\mu\gamma} \text{Im} \left[ e^{i\omega t} [\chi_{i\text{ill},\mu\mu\gamma\gamma}^{\downarrow\uparrow\downarrow\uparrow}(\omega)]^* + e^{-i\omega t} \chi_{i\text{ill},\mu\mu\gamma\gamma}^{\uparrow\downarrow\uparrow\downarrow}(\omega) \right]
 \end{aligned} \tag{2.3.29}$$

It is convenient to introduce the notation  $\uparrow\downarrow = +$ ,  $\uparrow\uparrow = \uparrow$ ,  $\downarrow\downarrow = \downarrow$  and  $\downarrow\uparrow = -$  for the spin indices and write the summed up response as

$$\chi_i^{++}(\omega) = \sum_{l,\mu\gamma} \chi_{i\text{ill},\mu\mu\gamma\gamma}^{\uparrow\downarrow\uparrow\downarrow}(\omega) \tag{2.3.30}$$

and analogous for all other spin combinations.

Using this notation, the change in the circular spin components  $S^\pm = S^x \pm iS^y$  can be written as

$$\begin{pmatrix} \delta\langle S_i^+ \rangle(t) \\ \delta\langle S_i^- \rangle(t) \end{pmatrix} = \frac{\mu_B g_S}{2} \begin{pmatrix} [\chi_i^{--}(\omega)]^* & \chi_i^{+-}(\omega) \\ [\chi_i^{+-}(\omega)]^* & \chi_i^{--}(\omega) \end{pmatrix} \begin{pmatrix} b^+(t) \\ b^-(t) \end{pmatrix} \tag{2.3.31}$$

The interest in this thesis lies in the responses for extended systems, which are obtained by the Fourier transform of Equation 2.3.31. For uniform fields such as the ones considered here, it is given by Equation 2.3.22 for  $\vec{q} = 0$ , which requires just one integral over the Brillouin Zone with the Green functions calculated at each wave vector  $\vec{k}$ .

In the same fashion, further dynamic properties of the system can be obtained, such as disturbances of orbital angular momenta,  $\delta\langle L \rangle(t)$ , spin-orbit and exchange torques,  $\langle \tau \rangle(t)$ , and spin and charge currents,  $\langle \vec{I} \rangle$ , flowing through the system.

## 3. Computational Methods

The simulation program for time-dependent transport and angular momentum properties in nanostructures, TITAN, already existed before this thesis. However, it has been originally written for a very specific use case: multilayers composed of transition metals with either a bcc surface along the  $[1\bar{1}0]$  or a fcc surface along the  $[001]$  direction. For this thesis, the program was generalized and extended for a broader range of use cases.

This chapter details the key points of the numerical procedures done to obtain the ground state and dynamical properties described in the previous chapter. It discusses the generation of the Bravais lattice for general systems and the set up of the Brillouin zone in reciprocal space. Furthermore, it explains the discretizations used to integrate over energy and wave vectors, and how the Green functions, that may have extremely sharp peaks, are handled. At the end of this chapter, the new parallelization scheme is explained, together with its influence on the performance of the code.

### 3.1. Lattice setup

Initially, TITAN was limited to specific 2D multilayered systems, i.e. fcc Pt and CoPt (001) as well as bcc W and FeW ( $1\bar{1}0$ ) systems. The first task of this thesis was to generalize the code to accept any kind of 2D or 3D bravais lattice. In combination with this task, the Slater-Koster parametrization was introduced, replacing the fixed DFT parameters that were available for the four original systems.

The new routine requires the user to give the Bravais lattice vectors, lattice constant and positions and types of atoms in the unit cell via an input file called ‘basis’. The unit cell is then setup and repeated a few times along the first two or all three lattice vectors, depending on whether one wishes to calculate a 2D or a 3D system, to determine the neighboring sites. The distance between the atoms in the unit cell and all atoms in this neighbor cloud is determined and sorted (see Figure 3.1). In the input file, the user can choose to give the amount of next nearest neighbor distances to be considered in the hopping integrals (up to second nearest neighbors by default). The hoppings for all neighbors with larger distances are neglected.

For an efficient treatment of the general unit cell, data structures for all atoms in the nearest neighbor cluster have been defined, containing information about their position, the distance to each atom in the unit cell, as well as the hopping matrix in real space for each atom in the unit cell that they are neighbored to.

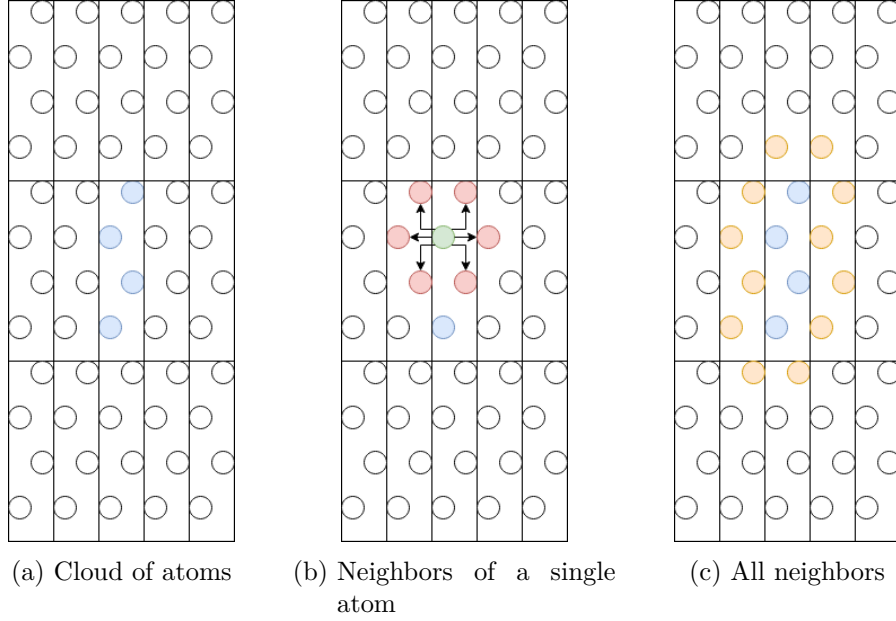


Figure 3.1.: Determination of first and second nearest neighbors for a 2D unit cell. (a) The unit cell is set up from the information in the input file and repeated along all dimensions. (b) The neighboring atoms for each atom in the unit cell are determined. (c) All atoms that are considered a neighbor to at least a single unit cell atom, are stored, discarding all unused atoms in the surrounding.

### 3.2. Brillouin zone generation

To discretize the Brillouin zone (BZ), it is necessary to first determine the reciprocal lattice vectors  $\vec{b}_i$ , which relate to the real space lattice vectors  $\vec{a}_i$  through:

$$\vec{a}_i \cdot \vec{b}_j = 2\pi\delta_{ij}. \quad (3.2.1)$$

For a three dimensional lattice they are defined as

$$\begin{aligned} \vec{b}_1 &= 2\pi \frac{\vec{a}_2 \times \vec{a}_3}{\vec{a}_1 \cdot (\vec{a}_2 \times \vec{a}_3)} \\ \vec{b}_2 &= 2\pi \frac{\vec{a}_3 \times \vec{a}_1}{\vec{a}_1 \cdot (\vec{a}_2 \times \vec{a}_3)} \\ \vec{b}_3 &= 2\pi \frac{\vec{a}_1 \times \vec{a}_2}{\vec{a}_1 \cdot (\vec{a}_2 \times \vec{a}_3)}, \end{aligned} \quad (3.2.2)$$

as for the two dimensional case the Brillouin zone is defined by

$$\begin{aligned} \vec{b}_1 &= 2\pi \frac{\vec{a}_2 \times \vec{e}_z}{\vec{e}_z \cdot (\vec{a}_1 \times \vec{a}_2)} \\ \vec{b}_2 &= 2\pi \frac{\vec{e}_z \times \vec{a}_1}{\vec{e}_z \cdot (\vec{a}_1 \times \vec{a}_2)}, \end{aligned} \quad (3.2.3)$$

with  $\vec{e}_z$  being the unit vector along z-direction.

With these vectors one can span and discretize a parallelepiped/parallelogram, respectively. The discretized points are then transformed into the Brillouin zone by subtracting the closest vertex of the parallelepiped/parallelogram (see Figure 3.2). A pseudocode example for this process can be found in Code 3.1.

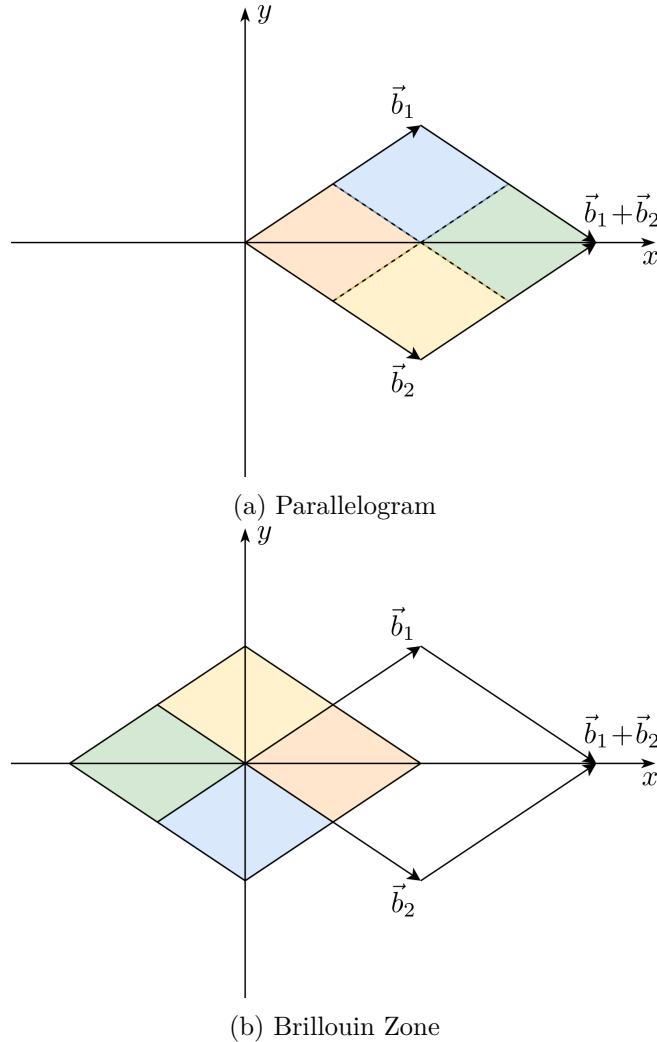


Figure 3.2.: Discretization of Brillouin zone. (a) The parallelogram with vertices  $\vec{0}$ ,  $\vec{b}_1$ ,  $\vec{b}_2$  and  $\vec{b}_1 + \vec{b}_2$  is setup and discretized. (b) The points are separated into groups by the vertex that is closest to them. Then, they are shifted by this vertex, moving their position to the actual BZ.

Points where more than one closest vertex exist will be duplicated and their weights will be adjusted. These points will, after the transformation, be at opposing borders of the Brillouin zone. The actual number of points will therefore be larger than the amount given by the user.

Code 3.1: Pseudocode of a simplified algorithm for BZ mesh generation in 3D.

```

def generate_3D_BZ(a1, a2, a3, nkpt):
    b1, b2, b3 = reciprocal_lattice(a1, a2, a3)
    vertices = define_vertices(b1, b2, b3)
    kpx = kpy = kpz = nkpt**(1/3)
    bz = []
    weight = []
    for i in range(kpx):
        for j in range(kpy):
            for k in range(kpz):
                p = get_point_in_parallelogram(vertices, i, j, k)
                v = find_closest_vertices(vertices, p)
                for vertex in v:
                    bz.append(p - vertex)
                    weight.append(1/len(v))
    weight = weight / nkpt
    return bz, weight

```

The actual implementation of the BZ mesh generation contains an additional feature to generate only a fraction of the BZ. This is necessary to achieve a balanced work parallelization for the energy dependent BZ mesh, which will be explained in the following sections.

### 3.3. Complex continuation

For the calculation of ground state properties and response functions in terms of Green functions, an integration over a half-infinite frequency domain is necessary. Even though the introduction of the broadening,  $\eta$ , makes the Green functions numerically integratable, it can still be demanding and problematic. From the spectral representation

$$G^r(E) = \lim_{\eta \rightarrow 0} \sum_m \frac{|m\rangle\langle m|}{E - \epsilon_m + i\eta}, \quad (3.3.1)$$

one can see that integration over energies still involves many peaks with sharp linewidth and thus may need a particularly fine discretization. One way around this problem is by complex continuation: Using the fact that the retarded Green function has no poles in the upper half of the complex plane, a closed contour with a path along the real axis  $I_r$ , followed by a path along the imaginary axis  $I_i$  at a fixed real energy  $\epsilon_F$  and closed by a quarter-circle  $I_C$ , should be zero ( $I_r + I_i + I_C = 0$ ). Therefore, the integration over the real axis can be substituted by one along the imaginary axis, where the Green functions get smoother with the larger imaginary part of the energy (see Figure 3.3). For the integration along the quarter-circle  $I_C$ , one can use the polar representation  $z \rightarrow \lim_{r \rightarrow \infty} r e^{i\phi}$  and integrate from  $\pi/2$  to  $\pi$ . The expectation values in ground state involve the integral over a single Green function. As  $G(z \rightarrow \infty) \sim \frac{1}{|z|}$ ,

the semi-circle integral can be written as

$$\int_C dz \frac{1}{z} = \lim_{r \rightarrow \infty} \int_{\pi/2}^{\pi} d\phi \frac{1}{r e^{i\phi}} i r e^{i\phi} = i \frac{\pi}{2}. \quad (3.3.2)$$

Therefore, the expectation value of an observable in ground state, given by Equation 2.2.8, can be rewritten as

$$\begin{aligned} \langle \hat{A} \rangle &= \frac{1}{\pi} \text{Im} \left[ \int_{\eta}^{\infty} dy \text{Tr} [G(\epsilon_F + iy) \hat{A}] + \frac{i\pi}{2} \text{Tr} \hat{A} \right] \\ &= \frac{1}{2} \text{Re} \text{Tr} \hat{A} + \frac{1}{\pi} \text{Im} \int_{\eta}^{\infty} dy \text{Tr} [G(\epsilon_F + iy) \hat{A}]. \end{aligned} \quad (3.3.3)$$

The first integral of the mean-field response function (Equation 2.3.22 is also semi-infinite, but involves the product of two retarded and two advanced Green functions. Thus the integral over the semi-circle can be rewritten as

$$\int_C dz \frac{1}{z^2} = \lim_{r \rightarrow \infty} \frac{1}{r} \int_{\pi/2}^{\pi} d\phi i e^{-i\phi} = 0 \quad (3.3.4)$$

and therefore the first integral of the mean-field response can be rewritten as

$$\begin{aligned} \chi_{\alpha\beta\gamma\delta}(\omega, \vec{k}) &= \frac{1}{2\pi i} \int_{\eta}^{\infty} dy \left[ G_{\beta\gamma}(\omega + \epsilon_F + iy, \vec{k}) G_{\delta\alpha}(\epsilon_F + iy, \vec{k}) \right. \\ &\quad \left. - [G_{\delta\alpha}(\epsilon_F + iy, \vec{k}) G_{\gamma\beta}(\omega + \epsilon_F + iy, \vec{k})]^* \right]. \end{aligned} \quad (3.3.5)$$

This technique is not suitable to the integral in the limits  $\epsilon_F - \omega$  to  $\epsilon_F$ , as it involves products of retarded and advanced Green functions, i.e., with poles on both sides of the complex plane. Therefore, the integration has to be done along the real axis in this range. As the Green functions are usually very sharp in that region (see Figure 3.3), a particularly fine discretization is needed there, causing most of the integration time to be spent on this term.

The integral along the imaginary axis is then mapped from  $[\eta, \infty)$  to  $[0, 1)$  using the transformation

$$\int_{\eta}^{\infty} dy f(y) = \int_0^1 dx \frac{1 + \eta}{(1 - x)^2} f\left(\frac{x + \eta}{1 - x}\right). \quad (3.3.6)$$

The integral is then discretized using Gauss-Legendre quadrature

$$\int_a^b dx f(x) = \frac{b - a}{2} \sum_{i=1}^n w_i f\left(\frac{b - a}{2} x_i + \frac{b + a}{2}\right), \quad (3.3.7)$$

where the points  $x_i$  are the  $n$  roots of the Legendre polynomial  $P_n(x)$  and the weights are given by

$$w_i = \frac{2}{(1 - x_i^2)[P'_n(x_i)]^2} . \quad (3.3.8)$$

The integral can be further split up into different parts to allow a finer discretization, e.g. when split into two parts, the Gauss-Legendre points are generated in the intervals  $[0, 10^{-2})$  and  $[10^{-2}, 1)$ . Figure 3.3 shows how the points will be distributed using two parts with 64 points each.

### 3.4. Energy-dependent Brillouin zone mesh

Most of the calculations are obtained through integrations along the imaginary energy axis and over the Brillouin zone. The Green functions have sharp peaks for energies close to the real axis. These peaks smoothen the further one is away from it. Figure 3.3 shows schematically how the Green functions change from sharp peaks (lower solid curve) to broadened curves (upper dashed curve) as the imaginary part of the energy increases. One can see why a cruder discretization of the Brillouin Zone suffices to achieve a convergent integration at larger imaginary parts of the energy.

To optimize the code, an energy dependent BZ mesh was implemented, reducing the total amount of calculations. For a given energy argument  $z = E + iy$ , the number of points used for the generation of the BZ is given by

$$N_{\text{BZ}}(y) = \left(\frac{y}{\eta}\right)^{1/d} N_{\text{BZ}}(\eta) , \quad (3.4.1)$$

where  $d$  is the dimensionality of the system,  $N_{\text{BZ}}(y)$  is the number of points given to subroutine setting up the BZ and  $N_{\text{BZ}}(\eta)$  and  $\eta$  are the number of points and the broadening given by the user in the input file (see Figure 3.4). This relation uses the rule of thumb that when the imaginary part of the energy decreases by an order of magnitude, approximately 10 times as many points per dimension are necessary to resolve the Lorentzian peak. A minimum of 1000 points is set, which is a conservative amount to have precise calculations.

Although this approach speeds up the code considerably, it also increases drastically the memory usage (a factor of  $\sim 11$  using the default amount of energy points). The increase in memory has been countered by a change in the parallelization, distributing the generation of points among all nodes (more details on that in section 3.6). By first summing the number of points in all Brillouin zones, each node can calculate how many and which points need to be generated locally.

As a positive side effect of this distributed approach, extremely fine meshes (e.g. 10 billion points) can be used when enough nodes are present to fulfill the memory requirements. Such meshes are necessary for calculations of metallic bulk systems with an extremely small broadening parameter (e.g.  $\eta < 10^{-4}$  Ry  $\approx 16$  K). Special care has to be taken for such fine meshes, as one reaches the limitations of 4-byte integers ( $\sim 2.14$  billion), such that a special compilation option has been added for these cases.

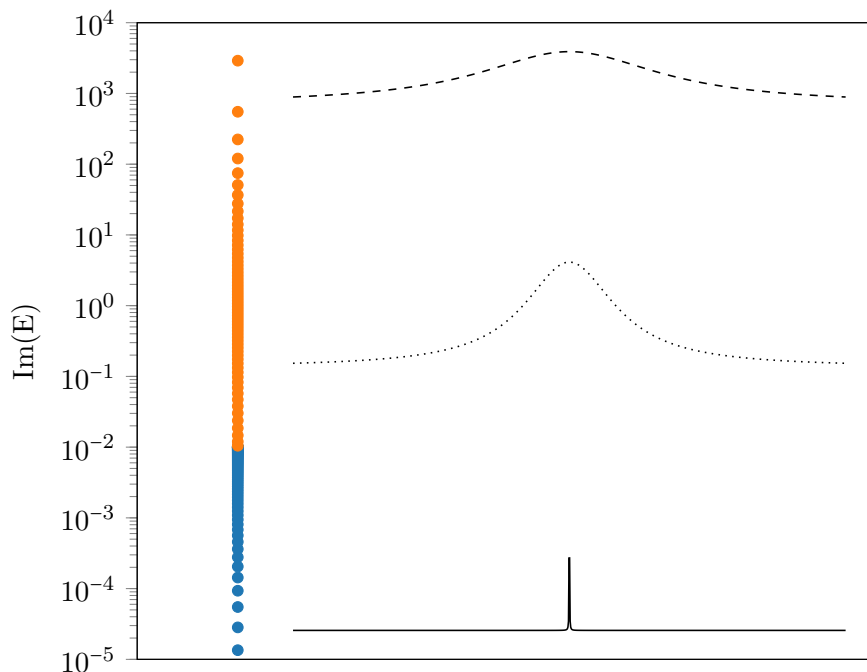


Figure 3.3.: Sketch of how larger imaginary parts of the energy affects the form of the Green function. The left side of the picture shows the distribution of energy points along the imaginary axis, in logarithmic scale, using TITAN's default settings of two parts (blue and orange) with each 64 points, while the right side depicts a Lorentzian distribution representing one of the Green function peaks.

### 3.5. Self-consistency

The Slater-Koster parameters used in TITAN are obtained for paramagnetic bulk configurations without any other interactions, such as external fields or spin-orbit interaction. For a correct description of the magnetic excitations of a system, it is necessary to start from a ground state that is compatible with these parameters, after the approximations are done and the additional terms are added. A self-consistent calculation is then performed to obtain the correct ground state expectation values for charge and spin densities that appear in the effective Coulomb interaction (Equation 2.1.31), as well as the Fermi level. These quantities are all bound to change upon the inclusion of the effective Coulomb interaction within the Hubbard model, external fields, and spin-orbit interaction. Other factors that can affect these values are modifications in the lattice configuration, such as varying the lattice constant or changing the dimensionality (e.g. multilayer structures) of the system.

From the Hohenberg-Kohn theorems [43] it is known that the Hamiltonian can be written as functional of the charge and spin densities and that there exist a unique set of charge and spin densities that minimize the energy of the system. In practice, the

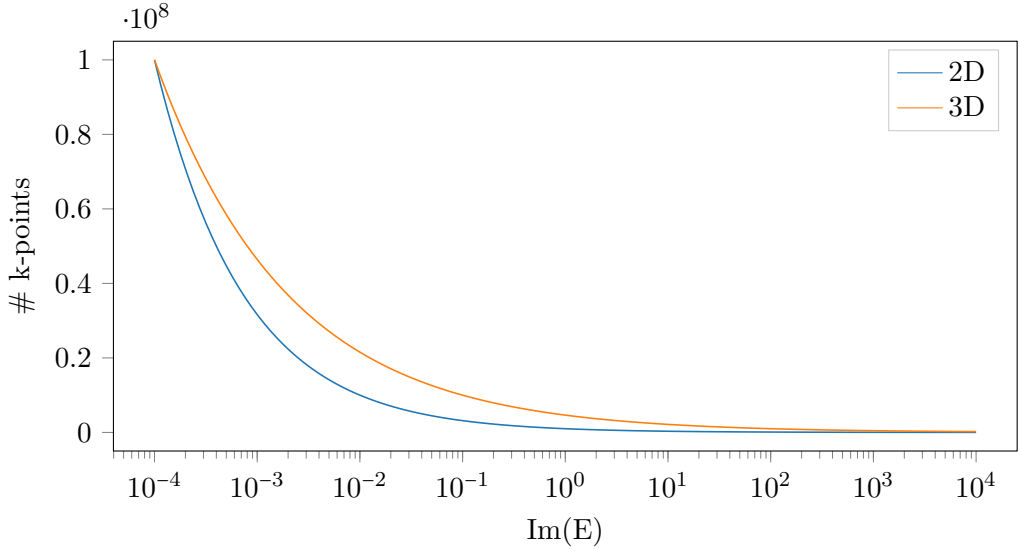


Figure 3.4.: Reduction of the amount of points in the BZ given by the user, with respect to the imaginary part of the energy. Starting from 100 million points for 2D and 3D systems.

many-body system is substituted by an effective single particle system that has the same ground state density as the original. The quantities that minimize the energy functional of the system can be obtained by iteratively calculating Equation 2.2.17 and updating the Hamiltonian, until self-consistency is reached [44].

The self-consistent calculations are done for the charge density and the magnetization of the  $d$ -orbitals under the constraints

$$\begin{aligned} n_i^{\text{out}, d}(n^{\text{in}, d}, \vec{m}^{\text{in}, d}, \epsilon_F) - n_i^{\text{in}, d} &= 0, \text{ and} \\ \vec{m}_i^{\text{out}, d}(n^{\text{in}, d}, \vec{m}^{\text{in}, d}, \epsilon_F) - \vec{m}_i^{\text{in}, d} &= 0, \end{aligned} \quad (3.5.1)$$

where the superscript ‘in’ describes the results of the previous iteration, and the superscript ‘out’ the results of the current iteration. The constraint is limited to the  $d$  orbitals, as these are the only ones that appear in the effective Coulomb interaction (Equation 2.1.31).

The charge density for an atomic site is allowed to change, but the total charge inside a unit cell has to be conserved (as the systems under consideration are periodic). To impose this, it is additionally imposed that the total number of electrons has to be constant

$$\sum_i n_i^{\text{out}}(n^{\text{in}}, \vec{m}^{\text{in}}, \epsilon_F) - N_{\text{el}} = 0. \quad (3.5.2)$$

These minimizations are done using the non-linear equation solver ‘C05RCF’ of the NAG Fortran library [45] which is based on the Powell hybrid solver. In every iteration, the routine returns new guesses for the charge density and magnetization of  $d$  orbitals as well as the Fermi level that are used to calculate the left hand side

of the constraints. When the convergence slows down, the Jacobian for the system of equations is calculated, determining the gradient and improving the convergence.

### 3.6. Parallelization

The parallelization of TITAN is done in three layers. After initialization and reading of all input files, the code enters the loop over different magnetic fields. The work done inside of each iteration is completely independent of the other iterations. The first layer of parallelization is to split up the available amount of MPI nodes into ‘parField’ groups. The variable ‘parField’ can be given by the user and defaults to one, which means this loop is done sequentially.

The first step in each iteration is to calculate the ground state charge density and magnetization self-consistently. The integrals over energy and Brillouin zone are flattened into a single sum over points  $(E, \vec{k})$ . This sum is split into equally sized part and each node in the group allocates its part of the work. The local workload is further split with OpenMP and the flattened integral is summed up locally using the OpenMP reduction clause. After the work is done locally, the results of all nodes in the group are summed up using the collective communication routine ‘MPI\_Allreduce’. Thus, all nodes obtain the final result of the self-consistency as they are necessary for further calculations.

In the same way, other ground state expectation values are computed. The only difference here is that the reduction routine ‘MPI\_Reduce’ is used: only the first node obtains the summed up result and writes them to a file.

The dynamic properties are obtained by looping over a set of given frequencies  $\omega$ . The iterations of this loop are again completely independent. The nodes available for a given value of the magnetic field are now further split up into ‘parFreq’ groups. Here, the variable ‘parFreq’ can again be given by the user and defaults to one.

The integrals in Equation 2.3.22 are now split up in the same manner as for the ground state properties, only with fewer nodes available (when split up among frequencies), thus increasing the workload of each node. The last integral in Equation 2.3.22 can not be solved using the complex continuation, as explained in section 3.3. Thus, this integration is performed close to the real axis, from  $\epsilon_F - \omega$  to  $\epsilon_F$ , and its workload is split up in the same way, except without using the energy-dependent mesh. Instead, since all the points have the same imaginary part, they use the largest BZ mesh for all energy points.

In the original parallelization, the distribution of the points for the integrals over energy and BZ was done differently. As the energy dependent mesh was not present before, the integral was distributed by energy points. This means that each node integrated a full BZ and it was not possible to use more MPI nodes than energy points for a given frequency and magnetic field. Aside from performing many unnecessary calculations for energy points far from the real axis, the original parallelization also limited the size of the BZ through the memory available for a single node. Thus the program was limited in the amount of nodes that could be used.

The only remaining similarity between the original and the new parallelization of the code is that the distribution of the field and frequency loops are done in the same way.

## 3.7. Full list of implementations

This chapter introduced a few aspects of the code, old and new, to give an introduction into the most challenging parts of the program. To finish this chapter, all major (and a few minor, but important) changes that have been done to the code as part of this thesis will be listed. Those changes, that have not been discussed before will receive a comment on their motivation in this section.

- Simplified reading of input parameters  
In the initial version of the program, adding a new parameter required parsing the input file anew. The changed version reads the complete input file and prepares the input variables for reading. Now, adding a new parameter can be done by calling an overloaded subroutine. It has been bundled into a standalone library that can be used for other projects as well (more details at: <https://github.com/JRSuckert/FInput>).
- Generalized lattice setup (see section 3.1)
- Implementation of the Slater-Koster parametrization (see section 2.1.2)
- Changed algorithm for BZ generation (see section 3.2)
- Energy dependent BZ mesh (see section 3.4)
- Generalized band structure calculations  
As the high symmetry points are not known anymore before compilation, the routine had to be changed. Now the user has to define points in the Brillouin zone in a file called 'kbands' and define a path by giving a list of these points in the 'input' file.
- Optimized parallelization (see section 3.6)
- Implementation of Gilbert damping calculation (see chapter 5)
- Using CMake for compilation, since TITAN is used on many different supercomputers (currently CLAIX, JURECA and JUQUEEN)

## 4. Numerical aspects

This chapter investigates general quality and performance aspects of TITAN. The model employed in the code, discussed in section 2.1, is evaluated through the calculation of the electronic structure and the magnetic ground state properties for bulk systems, as these are further investigated in the next chapter. To put the results into perspective, they are compared to results for the same systems obtained within the *ab initio* code SP-KKR [46, 47].

Then, convergence measurements are analyzed to understand how the the discretization for the calculations in the next chapter needs to be chosen.

Finally, to get a better understanding of the possible scale of calculations, the parallelization with MPI and OpenMP of TITAN is reviewed in terms of speedup measurements with respect to sequential executions of the code.

### 4.1. Quality of ground state properties

As an initial quality check of the tight-binding model, ground state properties for bcc Fe, fcc Co, and fcc Ni will be investigated. The studied properties are the magnetization, the local density of states as well as the band structures. For comparison, all three of this properties are also obtained within the SP-KKR code, a Green function DFT software package, based in the Korringa-Kohn-Rostocker (KKR) approach [47]. In TITAN, all calculations are obtained with  $\eta = 10^{-4}$  Ry, using the default value,  $U = 1$  eV, for the repulsive Coulomb interaction of  $U = 1$  eV and 100 million points in the largest BZ. The material dependent parameters can be found in Appendix A. Using SP-KKR, these values are obtained within local density (LDA), and atomic sphere approximations (ASA), a broadening of  $\eta = 5 \cdot 10^{-3}$  Ry and 117.649 points in the BZ are used.

The LDOS for bcc Fe obtained in TITAN, as shown in Figure 4.1, is in very good agreement with the results obtained with SP-KKR. The splitting of the bands in TITAN is slightly larger, which may be caused due to the U parameter being too large [48]. In the band structure, one can see that some bands are shifted with respect to the SP-KKR bands. The strongest deviation are found for the bands furthest from the Fermi-level, where the SP-KKR bands are not reproduced faithfully. The magnetization obtained for bcc Fe is  $2.2\mu_B$ , which is in very good agreement with results obtained SP-KKR and with experimental results [49].

For fcc Co, a shift of the Fermi-level can be recognized in the LDOS (Figure 4.2). This can also be seen from the band structure, where most bands are shifted downwards in energy with respect to the SP-KKR results. The *d* bands are split further

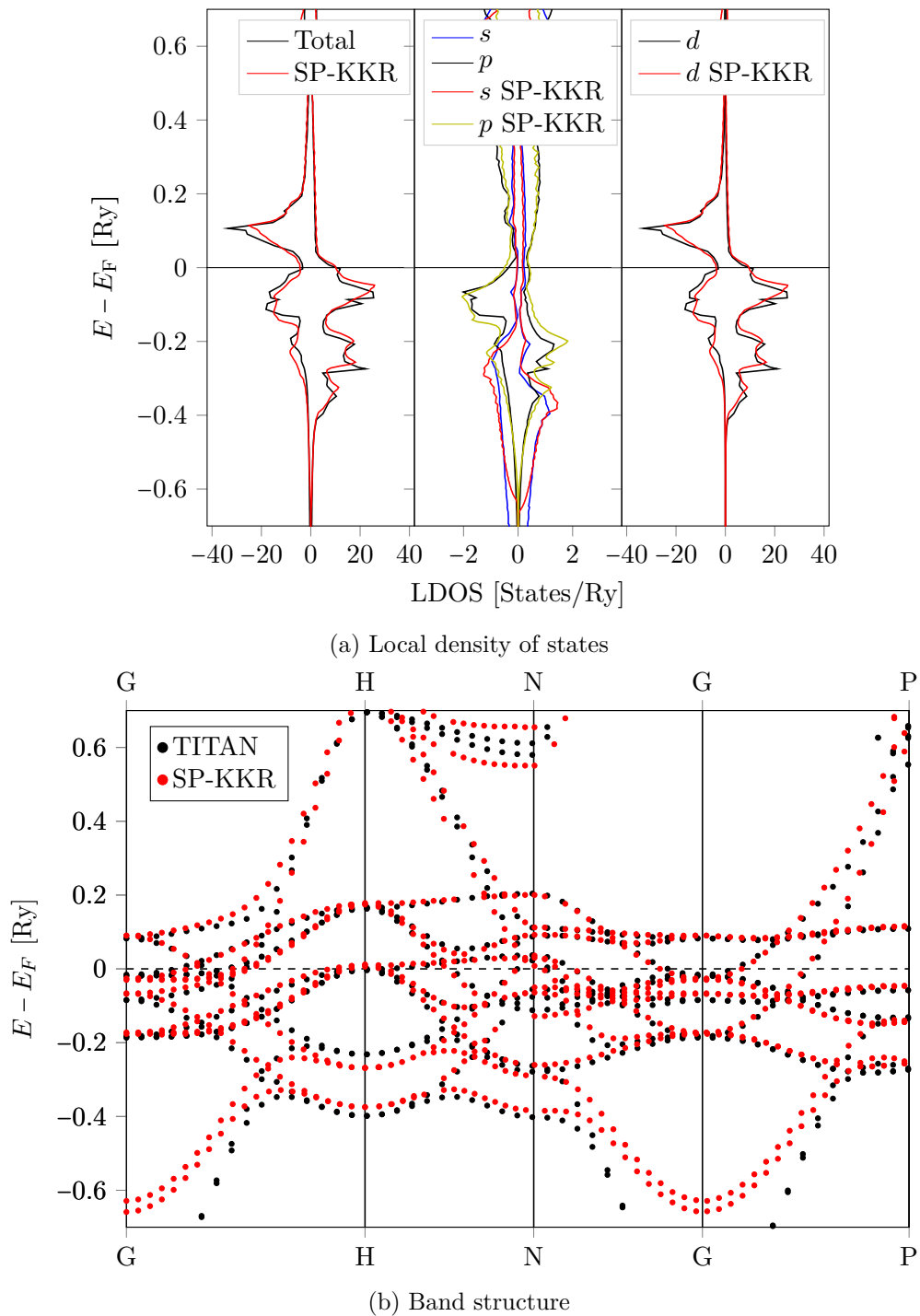


Figure 4.1.: LDOS and band structure of bcc Fe.

apart compared to the SP-KKR results, and the  $s$  bands below the Fermi-level are not well reproduced, even when accounting for the energy shift. The values for the magnetization obtained in TITAN ( $1.7\mu_B$ ), SP-KKR ( $1.6\mu_B$ ) and the experimentally ( $1.8\mu_B$  [49]) are in reasonable agreement. The larger splitting of the  $d$  bands is the cause of the larger magnetization compared to the SP-KKR results. The origin of this discrepancy with the SP-KKR results may not only come from a larger  $U$  parameter, but also from missing inter-atomic interactions [50].

Finally, from the LDOS and the band structure of fcc Ni shown in Figure 4.3, one can see that the results obtained from TITAN are in very good agreement with the SP-KKR ones. The peaks of the  $d$  bands close to the Fermi level are larger in TITAN which is caused by the smaller broadening and the resulting stronger localization of states. There might also be some hybridization effects, as the density of  $s$  states is too small. The magnetic moments for fcc Ni obtained from SP-KKR and experimentally are  $0.6\mu_B$  [49], while the value obtained in TITAN is  $0.7\mu_B$ . Although the relative error is high (17%), the absolute error is small.

## 4.2. Convergence of dynamic calculations

For the discussion of applications of TITAN, it is indispensable to understand how fine a discretization is needed for significant results. As has already been discussed in section 3.4, the value of the artificial broadening  $\eta$ , defining the minimal distance of the integration to the real axis, is a significant factor determining how fine the BZ meshes need to be. Here, convergence measurements for the Gilbert damping of bcc Fe, obtained from the spin-correlation model (see section 5.4), are done to determine the optimal amount of points in the Brillouin zone. The calculations are done for three different values for the broadening, ranging from  $\eta = 10^{-5}$  to  $\eta = 10^{-3}$ .

As one can see in Figure 4.4, converged values for  $\eta \geq 10^{-4}$  are reached for about 100 million points. For  $\eta = 10^{-5}$ , one can observe that above 100.000 points, the value drastically starts to change. For less points, the value does look flat and actually almost converged. This is most likely due to the fact that peaks of the Green functions lie between the points of the discretization in the BZ. For this broadening, one should use at least 1 billion points, which demonstrates the difficulty in the investigation of the Gilbert damping for clean systems at low temperatures.

## 4.3. Performance

To address difficult calculations, as the one in the previous section, large amounts of computing resources must be used. This requires an efficient parallelization scheme that is able to scale to a large number of computing nodes.

The performance of the MPI parallelization scheme for each part of the code, self-consistency (SC) and response function, as well as the full calculation are shown in Figure 4.5. The speedup measurements were done using a BZ mesh with 8 million points in the largest BZ (the one generated for the energy point closest to the real

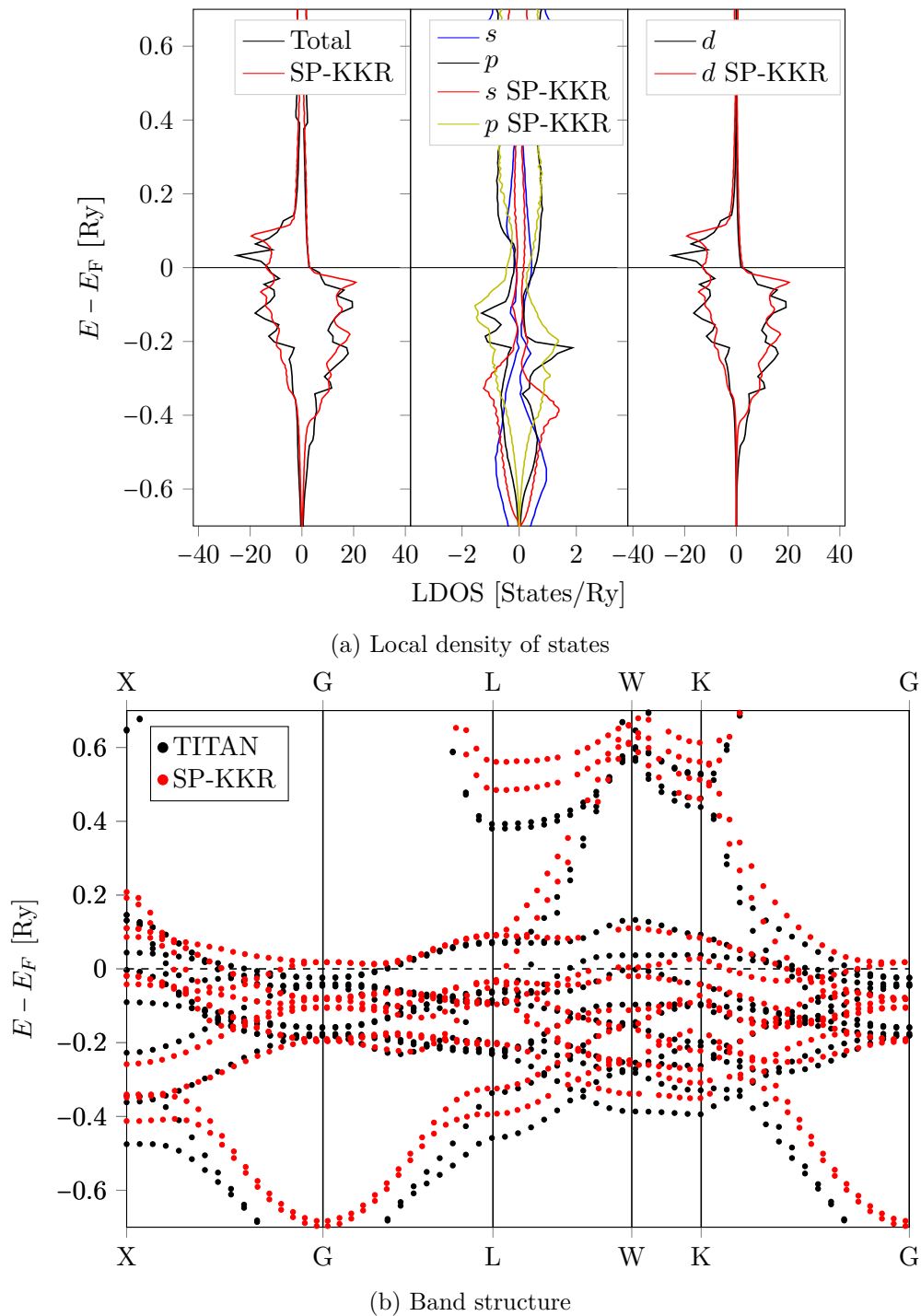


Figure 4.2.: LDOS and band structure of fcc Co.

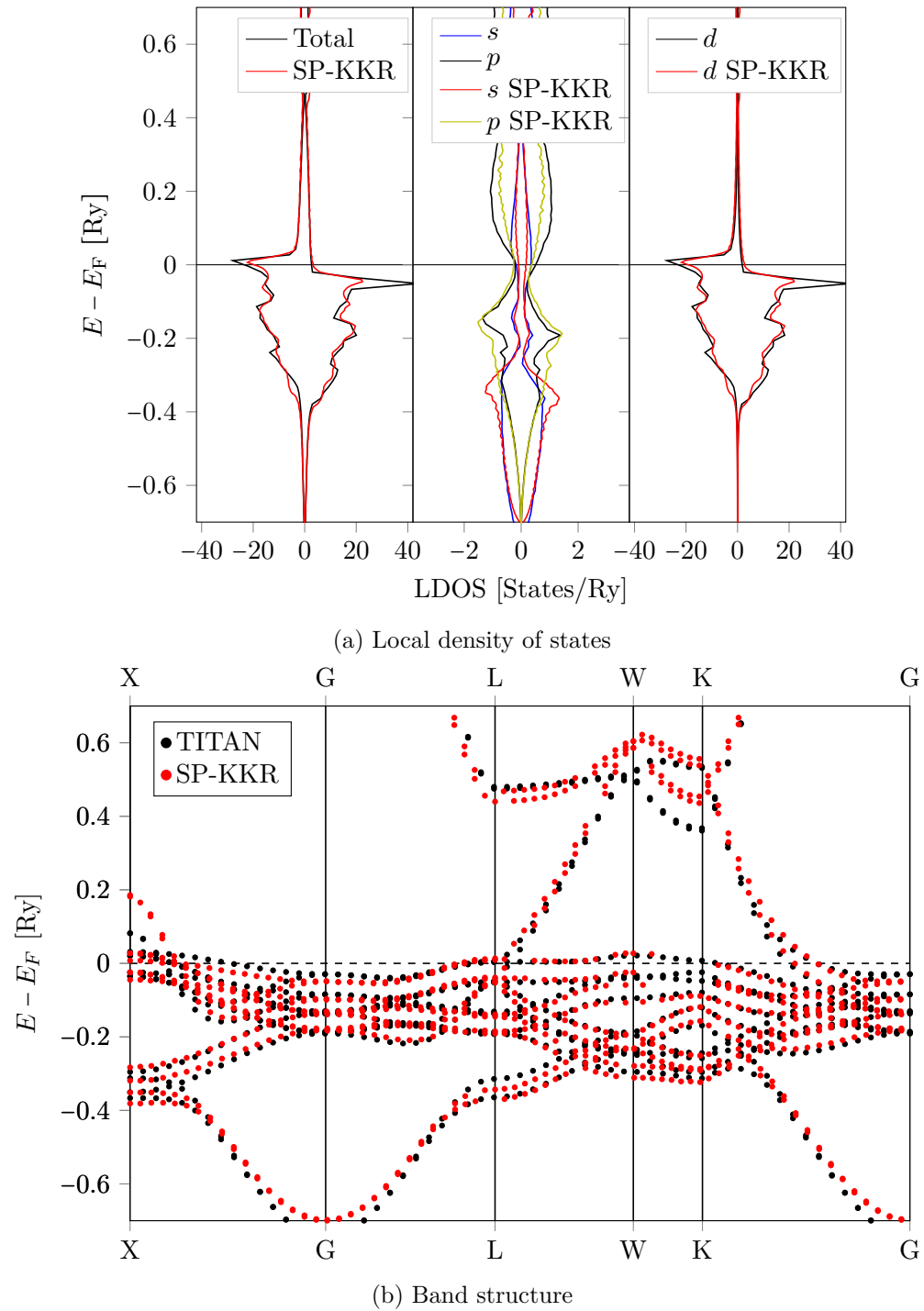


Figure 4.3.: LDOS and band structure of fcc Ni.

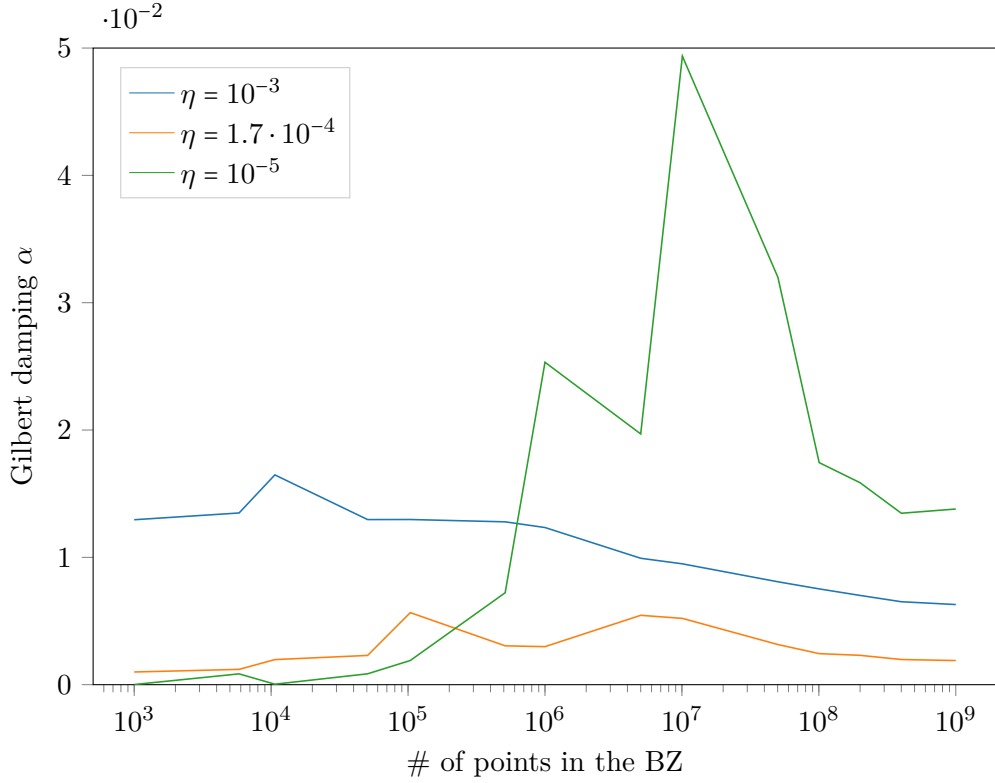


Figure 4.4.: Convergence with respect to the size of the largest BZ for the Gilbert damping obtained from the inverse transversal susceptibility in RPA.

axis). Along the imaginary axis, 128 energy points have been used, while 64 points were used for the real axis integration in the response functions. In Figure 4.5, one can see that the speedup follows closely the ideal curve. For 64 MPI nodes, the parallelization achieves a speedup of 59, which represents a deviation of approximately 8% from the theoretical optimal speedup. The speedup of just the calculation of the response function is slightly higher, at 61, less than 5% below the theoretical optimal speedup. One can observe that for the self-consistency calculation, the speedup is significantly lower for 32 and 64 MPI nodes. This is caused by the communication overhead, which gains importance as the amount of actual work per node is reduced. For the energy dependent mesh with 8 million points in the largest BZ, the amount of integration points per thread for the self-consistency calculation is approximately 150.000. For the response function, each thread has approximately 8 times as many iterations, which is why the speedup is still close to the theoretical optimum.

The OpenMP parallelization achieves a speedup of 20 for 24 OpenMP threads using a BZ mesh with one million points in the largest mesh (see Figure 4.6). Here, the same argument applies as for the MPI speedup of the self-consistency calculation. A better speedup can be expected when more points are used, increasing the workload per thread.

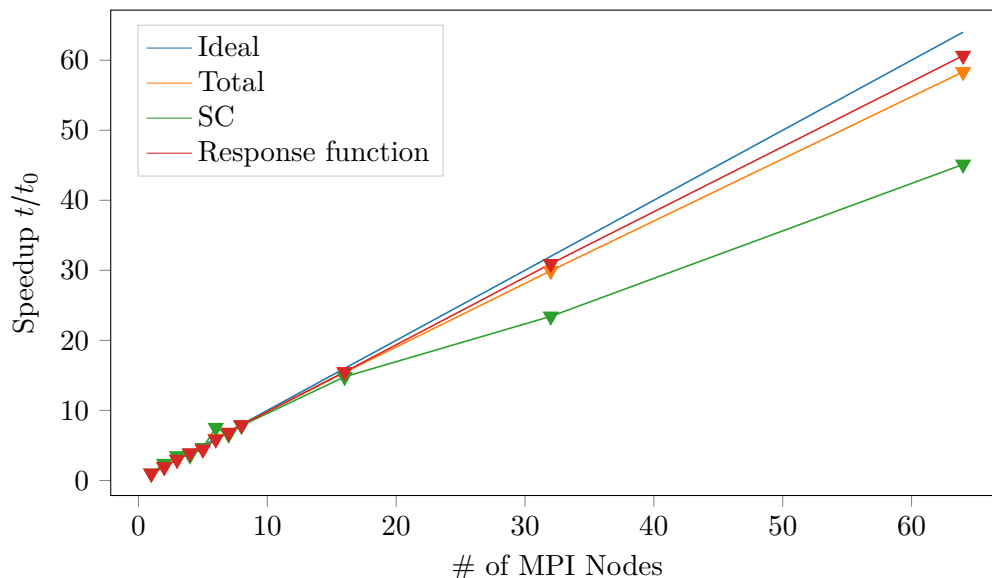


Figure 4.5.: MPI speedup for calculation of self-consistency and response function for a single frequency point, using 8 million  $\vec{k}$ -points for Fe bcc. Using 24 OpenMP threads on each node.

In both cases, the use of more points has been avoided to be conservative with the available computational resources. The speedup measurements were done using the JURECA supercomputer. The results shown in the next chapter were obtained using the supercomputers JURECA, CLAIX, and JUQUEEN.

## 4.4. Summary

In this chapter, the validity and performance of TITAN were investigated.

It could be seen, that the electronic and magnetic ground state properties are already quite well approximated. For fcc Co, there were still large differences in the LDOS and the band structure compared to the results obtained in SP-KKR. The self-consistent calculation of the ground state properties needs to be reevaluated, taking into account the orbital dependent densities. In this case, better agreements are expected.

From the convergence measurements, it became obvious that massive amounts of points may be necessary for the discretization of the BZ to obtain converged results for dynamical properties. This holds true especially for cases where the broadening,  $\eta$ , is taken to very small values.

Fortunately, the performance measurements demonstrate that TITAN is exceptionally well parallelized and can be used with vast amounts of CPU cores to account for such extremely fine discretizations.

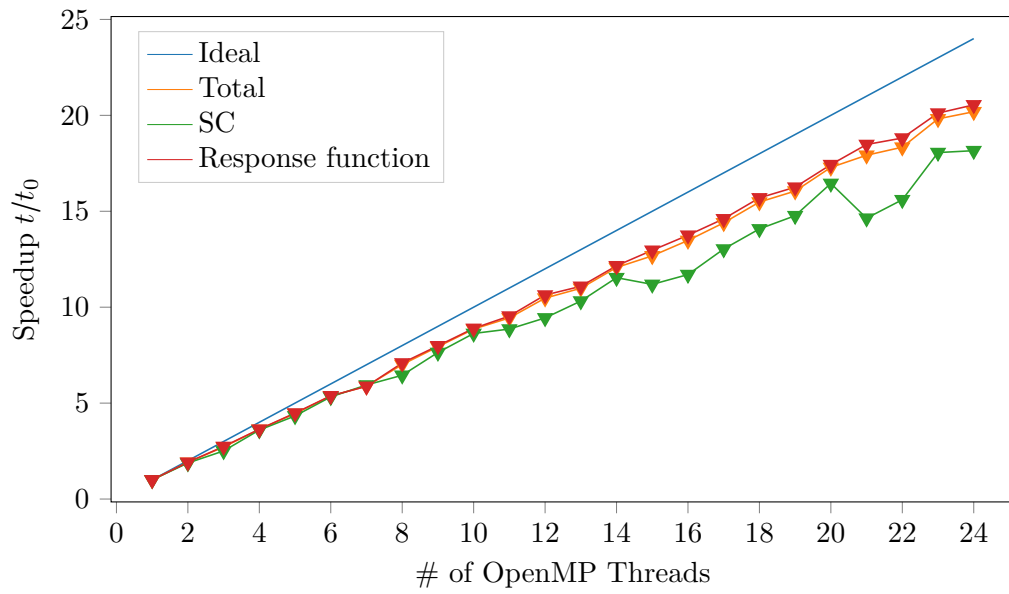


Figure 4.6.: OpenMP speedup for calculation of self-consistency and response function for a single frequency point, using one million  $\vec{k}$ -points for Fe bcc. Using 8 MPI nodes, each with the given number of OpenMP threads.

## 5. Gilbert Damping

To describe the dynamics of the magnetic moments, it is imperative to determine their equation of motion. As a semi-classical picture, in which the magnetic moments are assumed to be three dimensional vectors of constant length, the equation of motion is given by the Landau-Lifshitz-Gilbert equation [16, 15]

$$\frac{d}{dt}\vec{m}_i(t) = -\gamma\vec{m}_i(t) \times \vec{B}_{\text{eff}, i} + \alpha\vec{m}_i \times \frac{d}{dt}\vec{m}_i(t) . \quad (5.0.1)$$

This equation describes the time evolution of the unitary magnetic moments  $\vec{m}_i = \frac{\vec{M}_i}{M_i}$  at an atomic site  $i$  under the influence of an effective field  $\vec{B}_{\text{eff}, i}$ . The effective field is given as the change of the total energy with respect to the magnetization,

$$\vec{B}_{\text{eff}, i} = -\frac{\partial E}{\partial \vec{M}_i} . \quad (5.0.2)$$

The first term in Equation 5.0.1 describes a torque that sets the magnetic moment into a precessional mode around the equilibrium position (see red vector in Figure 5.1). The parameter  $\gamma$  is the gyromagnetic ratio. With just this term, the moments would precess indefinitely, never aligning with the effective field, even in the absence of an external time-dependent driving force.

The second term was introduced to describe relaxation of the magnetic moments, i.e. a torque that is oriented towards the effective field (see green vector in Figure 5.1). It quantifies the amount of angular momentum and energy that is dissipated out of the magnetic system.

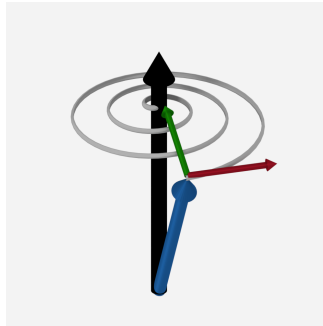


Figure 5.1.: Time evolution of a magnetic moment (blue arrow) in a static effective field (black arrow). The red arrow visualizes the precession torque and the green arrow the relaxation torque in Equation 5.0.1

Originally, this damping term was introduced as a phenomenological contribution [15], but later reformulated by Gilbert starting from a dissipative contribution in the Lagrangian [16]. This is why the parameter  $\alpha$  is commonly known as Gilbert damping. Numerous factors influence the strength of the damping parameter, such as intrinsic material properties, defects, and temperature. For magnetization dynamics in 3D, the parameter should be written as a  $3 \times 3$  tensor. In linear response, it reduces to  $2 \times 2$  tensor with components transverse to the magnetization direction. It can be further simplified to a scalar value for isotropic systems. Many efforts have been made to describe the nature of the Gilbert damping from first principles (see, for example, Refs. [17, 18, 51, 52, 53]) but the microscopic processes responsible for the observed relaxations in real materials are still not fully understood [19].

## 5.1. Overview

There exist numerous different approaches to obtain the Gilbert damping from first principles. The many different energy scales involved in the relaxation process, e.g. the ferromagnetic resonance frequency, intrinsic spin-orbit interaction, disorder and impurity scattering rate, led different authors to make qualitatively different predictions for the Gilbert damping. Experimentally, it can be obtained as relaxation of resonant processes through the linewidth of the ferromagnetic resonance peak (FMR) [54, 55], the inverse of which gives the lifetime of the excitation. The adimensional damping parameter is analogous to the quality factor of an oscillator [56], and is obtained by the ratio of the linewidth over the resonant frequency. It represents the number of oscillations it completes before being significantly damped. The first theoretical approach, to obtain a microscopic description of the Gilbert damping was made by Kambersky in 1970 [17], who considered that a change in magnetic moments forces a non-equilibrium population of electronic states that leads to a deformation of the Fermi surface. A few years later, in 1976, Kambersky proceeded to develop a new method to calculate the damping, known as torque correlation method (TCM). It became widespread due to its simplicity and low computational demand. More recent approaches, such as the one made by Garate and MacDonald [20], rely on a mapping of the inverse of the transverse susceptibility obtained from first principles to the LLG equation in Equation 5.0.1.

In many of these approaches, the relaxation process originates in the spin-flip scattering, and the electron-electron interaction is taken into account within the mean-field approximation [57], i.e. neglecting the influence of the collective modes. The existence of this many different methods is founded in the fact that the nature of the Gilbert damping is not yet completely explored and there are still open questions.

A key question is the behaviour of the damping at low temperatures. Kambersky already observed that in his model, for bulk crystals, the damping has two separate behaviours with respect to broadening of the Green functions [18]. At low temperatures the damping shows conductivity-like behaviour, increasing with  $\eta^{-1}$  as  $T \rightarrow 0$ . At high temperatures the damping behaves in a resistivity-like fashion, increasing

with  $\eta$  for larger temperatures. Together, these effects form a characteristic minimum of the damping. However, some authors claim that the damping should remain finite [19, 58, 59, 60], or even vanish [51, 61] for bulk materials without disorder at  $T = 0$  K.

In experiments [62, 70], an increase in the damping was measured, but it was material dependent and it was not clear if it would keep increasing until  $T \rightarrow 0$ . The role of impurities in these experiments is not clear and the observed behaviour at low temperature could be caused by them.

The role of the intrinsic spin-orbit interaction is still debated. It is not clear whether spin-orbit interaction should be included in the ground state or only as a perturbation [19, 34, 63]. Edwards [19] has shown that Kambersky's TCM formula is obtained using a perturbative approach for low SOC intensities  $\lambda$ . For that reason, he argues that the ground states should be obtained without spin-orbit interaction, otherwise inconsistent results would be generated that could lead to the divergence. Tserkovnyak [61] argued that the divergence occurs because the limits for the frequency and the broadening are taken in the wrong order, and taking the limit of vanishing broadening for a finite frequency would result in a vanishing damping.

In the quest of shedding some light on the evident controversies and to get a better general understanding of the different approaches for the damping, the next sections will explore a subset of the existing methods. Each of these methods will be applied for the cases of bulk transition metals: bcc Fe, fcc Co and fcc Ni.

## 5.2. Breathing Fermi surface model (BFS)

The first proposed method of calculating the Gilbert damping from first principles was the breathing Fermi surface (BFS) model introduced by Kambersky [17]. It is detailed here for completeness, but it will not be explored in this thesis.

This approach investigates how a change in the magnetic moment,  $\delta\vec{m}$ , affects the total energy of the system

$$E = \sum_{j,\vec{k}} \epsilon_{j,\vec{k}} n_{j,\vec{k}} , \quad (5.2.1)$$

where  $\epsilon_{j,\vec{k}}$  and  $n_{j,\vec{k}}$  are the eigenenergies and occupations of band  $j$  with wavevector  $\vec{k}$ . Without spin-orbit coupling the total energy of the system is invariant under rotation of the magnetization. However, in presence of spin-orbit coupling,  $\delta\vec{m}$  will cause a change in the total energy given by

$$\delta E = \sum_{j,\vec{k}} \delta n_{j,\vec{k}} \epsilon_{j,\vec{k}} + \sum_{j,\vec{k}} n_{j,\vec{k}} \delta \epsilon_{j,\vec{k}} . \quad (5.2.2)$$

This is caused by a change in the occupation numbers,  $\delta n_{j,\vec{k}}$ , and by a change in the single particle energies,  $\delta \epsilon_{j,\vec{k}}$ . For relatively small spin-orbit coupling, one can assume it only acts as a small perturbation and the change in occupation only occurs close to the Fermi level,

$$\sum_{j,\vec{k}} \delta n_{j,\vec{k}} \epsilon_{j,\vec{k}} \sim \epsilon_F \sum_{j,\vec{k}} \delta n_{j,\vec{k}} = 0 , \quad (5.2.3)$$

due to conservation of the total number of electrons in the system. Therefore the variation of the total energy is given by

$$\delta E = \sum_{j,\bar{k}} n_{j,\bar{k}} \delta \epsilon_{j,\bar{k}} \quad (5.2.4)$$

A precession of the magnetic moment will cause a continuous and oscillatory redistribution of both electronic states and occupations numbers which changes the single particle energies. This will distort the Fermi surface of the system making it “breath”.

A key factor here is that a change in occupation numbers is related to a change in the Fermi-Dirac distribution  $f_{j,\bar{k}}$ . As the BFS model does not contain a microscopic description of the scattering processes which cause these changes, they are instead introduced by a relaxation time parameter  $\tau$  as

$$n_{j,\bar{k}}(t) = f_{j,\bar{k}}(t) - \tau \frac{df_{j,\bar{k}}}{dt}. \quad (5.2.5)$$

The relaxation time is usually in the range of femtoseconds. Using this approach, as shown by Fähnle [52], the damping tensor can be calculated as

$$\alpha_{lm} = -\gamma\tau \sum_{j,\bar{k}} \frac{\partial f_{j,\bar{k}}}{\partial \epsilon_{j,\bar{k}}} \frac{\partial \epsilon_{j,\bar{k}}}{\partial M_l} \bigg|_{\vec{M}} \frac{\partial \epsilon_{j,\bar{k}}}{\partial M_m} \bigg|_{\vec{M}}. \quad (5.2.6)$$

As the predicted damping rate is proportional to the scattering time, the damping can not be calculated more accurately than the scattering time is known. Therefore, it is not possible to make quantitative comparisons between calculations of the BFS and experiments [53]. Kambersky later derived a more general formalism [18] which will be explored in section 5.6.

### 5.3. Ferromagnetic Resonance (FMR)

Ferromagnetic resonance (FMR) arises when the energy levels are split due to a static Zeeman or anisotropy field and the system absorbs energy from an oscillating magnetic field at sharply defined frequencies. Classically, this occurs for oscillatory fields at the Larmor frequency.

For a system subjected to a static magnetic field  $\vec{B}_0 = B_0 \vec{e}_z$  in the local frame of reference, determined by the magnetization direction,  $\vec{m} = \vec{e}_z$ , a small perturbation in the form of an oscillatory magnetic field  $\vec{b}(t) = b^x(t) \vec{e}_x + b^y(t) \vec{e}_y$  acting on the ground state of a system, will cause the magnetization to precess with a small cone angle around its equilibrium position,  $\vec{m}(t) = \vec{e}_z + \delta \vec{m}(t)$ . The change of the  $z$ -component will be small  $\delta m^z(t) \sim 0$  and it is reasonable to assume it to be constant. Thus, for the simple case of bulk systems, we assume the effective field,  $\vec{B}_{\text{eff}}$ , is given as sum of an external field  $\vec{B}_{\text{ext}}(t) = \vec{B}_0 + \vec{b}(t)$  and a general biaxial anisotropy  $\vec{B}_{\text{ani}}(t) = \frac{1}{M}(K^x m^x(t) \vec{e}_x + K^y m^y(t) \vec{e}_y + K^z \vec{e}_z)$ . The transversal components of the LLG equation

(Equation 5.0.1) are then given as

$$\begin{pmatrix} B_0 + \frac{1}{M}(K^z - K^x) + \frac{\alpha_x}{\gamma} \frac{d}{dt} & -\frac{1}{\gamma} \frac{d}{dt} \\ \frac{1}{\gamma} \frac{d}{dt} & B_0 + \frac{1}{M}(K^z - K^y) + \frac{\alpha_y}{\gamma} \frac{d}{dt} \end{pmatrix} \begin{pmatrix} m^x(t) \\ m^y(t) \end{pmatrix} = \begin{pmatrix} b^x(t) \\ b^y(t) \end{pmatrix} \quad (5.3.1)$$

The Fourier transform into frequency domain gives

$$\begin{pmatrix} B_0 + \frac{1}{M}(K^z - K^x) - i\frac{\alpha_x\omega}{\gamma} & i\frac{\omega}{\gamma} \\ -i\frac{\omega}{\gamma} & B_0 + \frac{1}{M}(K^z - K^y) - i\frac{\alpha_y\omega}{\gamma} \end{pmatrix} \begin{pmatrix} m^x(\omega) \\ m^y(\omega) \end{pmatrix} = \begin{pmatrix} b^x(\omega) \\ b^y(\omega) \end{pmatrix} \quad (5.3.2)$$

Transformation into circular components  $m^\pm = m^x \pm im^y$  gives

$$\begin{pmatrix} \tilde{B} + \frac{\omega}{\gamma} \left(1 - i\frac{\alpha_x + \alpha_y}{2}\right) & \frac{K^y - K^x}{2M} + i\frac{\omega}{\gamma} \frac{\alpha_y - \alpha_x}{2} \\ \frac{K^y - K^x}{2M} + i\frac{\omega}{\gamma} \frac{\alpha_y - \alpha_x}{2} & \tilde{B} - \frac{\omega}{\gamma} \left(1 + i\frac{\alpha_x + \alpha_y}{2}\right) \end{pmatrix} \begin{pmatrix} m^+(\omega) \\ m^-(\omega) \end{pmatrix} = \begin{pmatrix} b^+(\omega) \\ b^-(\omega) \end{pmatrix} \quad (5.3.3)$$

with  $\tilde{B} = B_0 + \frac{1}{M}(K^z - \frac{K^x + K^y}{2})$ .

In linear response theory, the response of magnetic moments to an oscillating magnetic field is given by

$$Mm^-(\omega) = \chi_{M^-M^+}(\omega)b^-(\omega) \quad (5.3.4)$$

where  $\chi_{M^-M^+}$  gives the response of the magnetic moment  $M^-$  to an external field which couples to  $M^+$  since  $\vec{M} \cdot \vec{b} = M^x b^x + M^y b^y = \frac{1}{2}(M^+ b^- + M^- b^+)$ .

Finally, for bulk materials with uniaxial anisotropy,  $K^x = K^y$ , the damping will also be isotropic ( $\alpha_x = \alpha_y$ ) and Equation 5.3.3 becomes diagonal. One can then identify the response function  $\chi^{-+}(\omega)$  as

$$\chi_{M^-M^+}(\omega) = \frac{\gamma M}{(\omega - \gamma\tilde{B}) - i\omega\alpha} \quad (5.3.5)$$

or

$$\text{Im}\chi_{M^-M^+}(\omega) = \frac{\gamma M \omega \alpha}{(\omega - \gamma\tilde{B})^2 + \omega^2 \alpha^2}. \quad (5.3.6)$$

This quantity is related to the energy absorption and dissipation of the system through the fluctuation-dissipation theorem [41], which is the quantity measured in FMR experiments [64]. The form of Equation 5.3.6 is a Lorentzian distribution when keeping the frequency fixed,  $\omega = \omega_0$ , and varying the intensity of the magnetic field  $\tilde{B}_0$ . In this case, the resonance is located at  $B_{\text{res}} = \frac{\omega_0}{\gamma}$  and the linewidth is  $\Delta B = \alpha\omega_0$ . Varying the frequency  $\omega$  and keeping the magnetic field  $\tilde{B}_0$  fixed, Equation 5.3.6 takes the form of a skewed Lorentzian, where the damping can be obtained from the linewidth through  $\Delta\omega/\omega_0 \approx \alpha + O(\alpha^3)$ . The higher order terms could generate deviations from the correct behaviour, which can be avoided by fitting the curve.

Using TITAN, the FMR curve can be calculated from the spin-spin response, by using the mapping  $\chi_{M^-M^+} = -\gamma^2 \langle\langle \hat{S}^-, \hat{S}^+ \rangle\rangle$ , both as a function of the frequency or as function of the magnetic field. As only uniform fields ( $\vec{q} = 0$ ) are considered in this thesis, the index  $\vec{q}$  of the response function has been dropped. Since the ground state changes when a magnetic field is applied, a new self-consistency calculation would

have to be done for each step. This is not the case when varying the frequency, so we choose this alternative to calculate  $\alpha$ .

The FMR curves for bcc Fe, fcc Co and fcc Ni are given in Figure 5.2. They are calculated for three different values of the broadening  $\eta$ , including spin-orbit interaction in the ground state Hamiltonian and without external fields. As no external fields are applied, the resonance frequency is determined by the anisotropy of the system that arises due to the spin-orbit interaction. The values of broadening were chosen at the minimum damping for  $\eta = \eta_0$ , one value for smaller broadening,  $\eta_<$ , in the conductivity-like region, and another for larger broadening,  $\eta_>$ , in the resistivity-like region.

The minimal value of the damping at  $\eta_0$  increases with decreasing magnetization, with the damping of elemental Ni being almost a magnitude larger than that of elemental Fe.

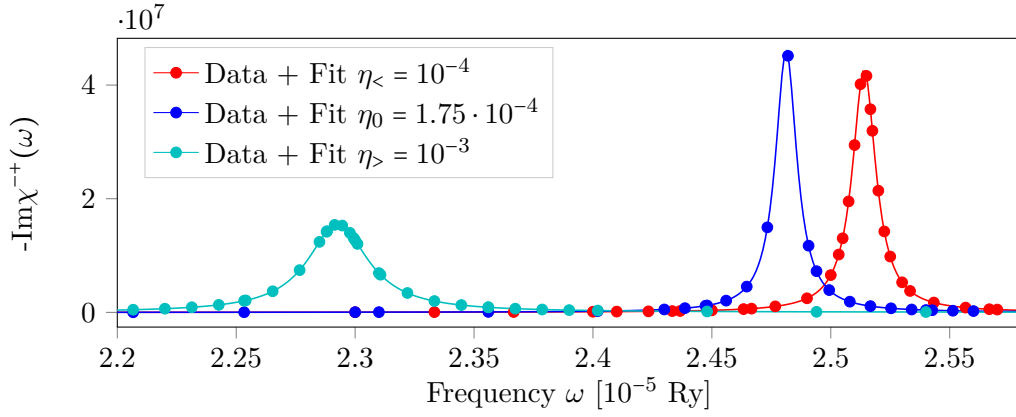
Table 5.1.: Magnetization,  $M/\gamma$ , Gilbert damping,  $\alpha$ , and anisotropy field  $\gamma\tilde{B}$ , obtained by fitting  $-\text{Im}\chi_{M-M^+}(\omega)/\gamma^2$  (Equation 5.3.6) to the curves in Figure 5.2.

$\eta$ [Ry]	$M/\gamma$	$\alpha$	$\gamma\tilde{B}$ [Ry]
bcc Fe			
$\eta_< = 10^{-4}$	2.558	$2.381 \cdot 10^{-3}$	$2.514 \cdot 10^{-5}$
$\eta_0 = 1.75 \cdot 10^{-4}$	2.531	$2.217 \cdot 10^{-3}$	$2.481 \cdot 10^{-5}$
$\eta_> = 10^{-3}$	2.396	$6.741 \cdot 10^{-3}$	$2.292 \cdot 10^{-5}$
fcc Co			
$\eta_< = 10^{-4}$	1.717	$8.202 \cdot 10^{-3}$	$5.268 \cdot 10^{-5}$
$\eta_0 = 3.75 \cdot 10^{-4}$	1.616	$5.197 \cdot 10^{-3}$	$4.862 \cdot 10^{-5}$
$\eta_> = 10^{-3}$	1.604	$1.027 \cdot 10^{-2}$	$4.717 \cdot 10^{-5}$
fcc Ni			
$\eta_< = 10^{-4}$	$7.884 \cdot 10^{-1}$	$2.325 \cdot 10^{-2}$	$4.433 \cdot 10^{-5}$
$\eta_0 = 2.5 \cdot 10^{-4}$	$7.884 \cdot 10^{-1}$	$1.881 \cdot 10^{-2}$	$4.494 \cdot 10^{-5}$
$\eta_> = 10^{-3}$	$7.310 \cdot 10^{-1}$	$4.506 \cdot 10^{-2}$	$4.204 \cdot 10^{-5}$

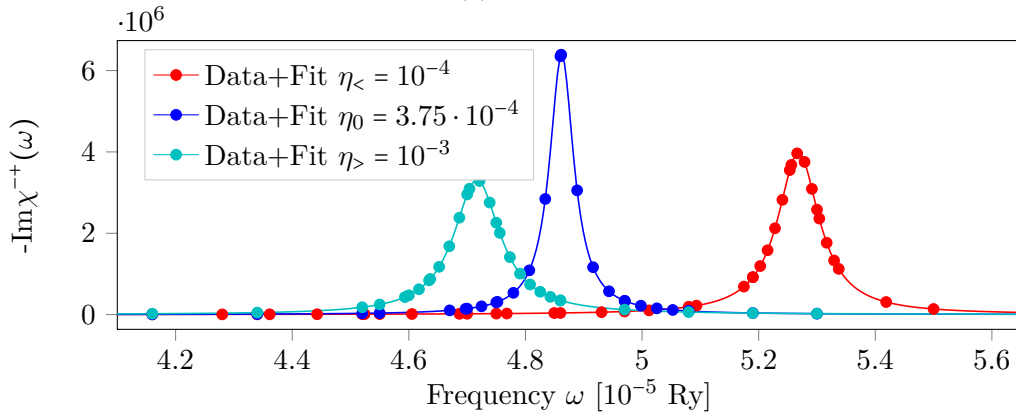
Obtaining the FMR curve is the most straightforward approach to calculate the Gilbert damping, since it mimics experimental setups. Unfortunately, this approach involves the calculation of the response function over a wide range of frequencies to find and resolve the resonance peak. A simpler method that yields similar results will be introduced in the next section.

## 5.4. Spin-correlation method (SCM)

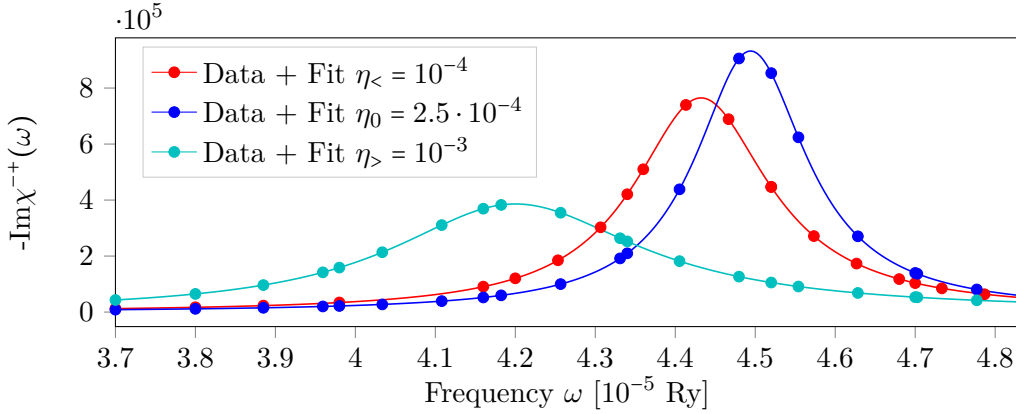
It might not be feasible to calculate the damping from the theoretical FMR curve, but exploring the analytical form of the phenomenological response, an alternative



(a) bcc Fe



(b) fcc Co



(c) fcc Ni

Figure 5.2.: Ferromagnetic resonance for three different materials, each of them calculated for three different broadenings,  $\eta$ . The points are obtained by calculation via TITAN and the solid lines are obtained by fitting the points to  $-\text{Im}\chi_{M-M^+}(\omega)/\gamma^2$  (Equation 5.3.6).

approach emerges. By inspection of Equation 5.3.5, one can obtain the damping parameter as the imaginary part of the inverse response function [20] as

$$\alpha = \frac{M}{\gamma} \lim_{\omega \rightarrow 0} \frac{\text{Im}[\chi^{-1}(\omega)]^{-+}}{\omega} \quad (5.4.1)$$

where  $[\chi^{-1}]^{-+}(\omega)$  is the inverse of the microscopic spin-spin response function that is related to the magnetization response through the mapping

$$\chi_{M-M^+}(\omega) = -\gamma^2 \langle\langle \hat{S}^-(\omega), \hat{S}^+ \rangle\rangle = -\gamma^2 \chi^{-+}(\omega). \quad (5.4.2)$$

Here, the static limit is taken to minimize the effect of higher order terms in the derivatives of the magnetic moments which were not considered in Equation 5.0.1 [65]. This approach will be referred to as spin-correlation method (SCM).

In Figure 5.3 one can see that the characteristic form described by Kambersky [18] can be recovered. For comparison, the damping obtained from fitting the FMR curves has been included as well. Equation 5.4.1 is general and should give the same result as the linewidth described in section 5.3, apart from the higher order terms mentioned above. It can be seen, that the agreement is striking, especially for Ni, showing that the higher order corrections are small in this range of frequencies and broadenings [66].

It is also possible to calculate the damping in terms of the mean-field response using Equation 2.3.23. Since  $U$  is real, and considering sums over  $d$ -orbitals only,  $\alpha$  can be written as

$$\alpha = \frac{M}{\gamma} \lim_{\omega \rightarrow 0} \frac{\text{Im}[\chi_0^{-1}(\omega)]^{-+}}{\omega} \quad (5.4.3)$$

When the system has uniaxial symmetry (i.e.,  $\chi^{++} = \chi^{--} = 0$  and the matrix is diagonal) [67], the functional form for the transverse magnetic susceptibility can be used. In the limit of  $\omega \rightarrow 0$ , the real part is approximately constant whereas the imaginary part shows a linear behaviour with frequency [68], i.e.,

$$\chi_0^{-+}(\omega) \approx \text{Re}\chi_0^{-+}(0) + i\omega \text{Im} \left. \frac{d}{d\omega} \chi_0^{-+}(\omega) \right|_{\omega=0} \quad (5.4.4)$$

One can write the inverse of Equation 5.4.4 as

$$\begin{aligned} [\chi_0^{-1}(\omega)]^{-+} = & \left\{ [\text{Re}\chi_0^{-+}(0)]^2 + \left[ \omega \text{Im} \left. \frac{d}{d\omega} \chi_0^{-+}(\omega) \right|_{\omega=0} \right]^2 \right\}^{-1} \\ & \times \left\{ \text{Re}\chi_0^{-+}(0) - i\omega \text{Im} \left. \frac{d}{d\omega} \chi_0^{-+}(\omega) \right|_{\omega=0} \right\}. \end{aligned} \quad (5.4.5)$$

Therefore, one obtains for the Gilbert damping

$$\alpha = -\frac{M}{\gamma} \frac{1}{[\text{Re}\chi_0^{-+}(0)]^2} \lim_{\omega \rightarrow 0} \frac{\text{Im}[\chi_0^{-+}(\omega)]}{\omega} \quad (5.4.6)$$

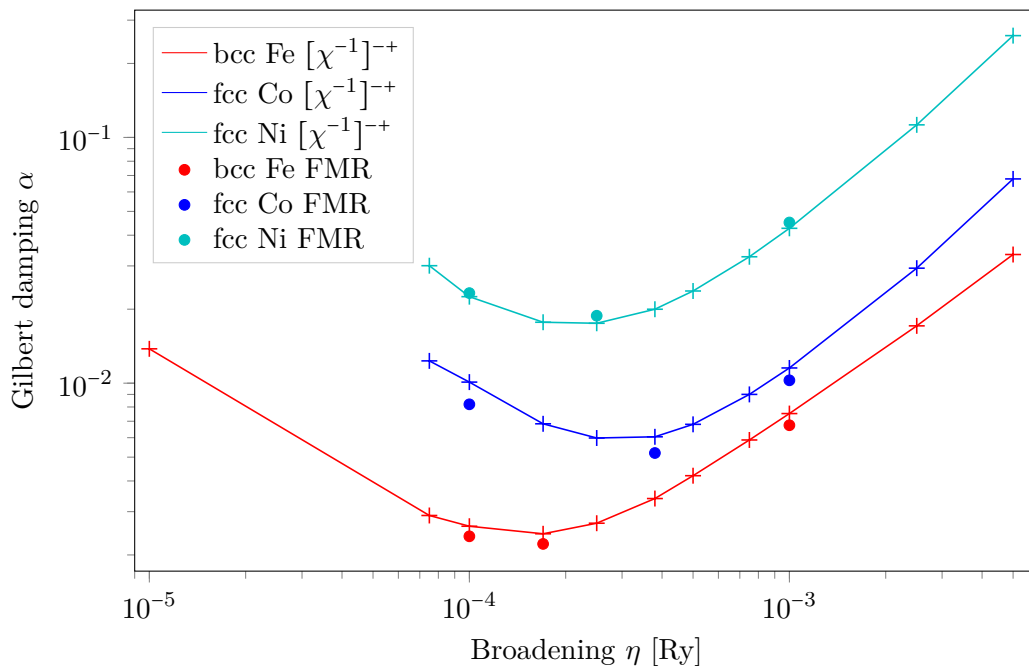


Figure 5.3.: Gilbert damping,  $\alpha$ , with respect to the broadening  $\eta$  obtained from the inverse slope of the SCM in RPA, including spin-orbit interaction in the ground state. For comparison, the results from section 5.3, i.e. FMR, have been included as well.

where the imaginary part in the denominator is of order  $\mathcal{O}(\omega^3)$  and thus vanishes when taking the limit  $\omega \rightarrow 0$ .

The real part of the mean-field response at zero frequency can be approximated using the sum rule for response function at zero frequency in the absence of spin-orbit interaction. For bulk materials and considering only  $d$ -orbitals in the response function, one can write [69]

$$\text{Re}\chi_0^{-+}(0) = \frac{1}{-U + \mu_{\text{B}}g_{\text{S}}B_{\text{ext}}M^{-1}}. \quad (5.4.7)$$

Finally, in absence of an external magnetic field, the damping can be written as

$$\alpha = -\frac{MU^2}{\gamma} \lim_{\omega \rightarrow 0} \frac{\text{Im}[\chi_0^{-+}]}{\omega} \quad (5.4.8)$$

Compared to Equation 5.4.1, this approximation has the advantage that it uses the mean-field response, which is easier and cheaper to obtain not only using the tight-binding framework, but also from DFT-based calculations.

As can be seen in Figure 5.4, the approximation, going from the RPA response function to the mean-field response function, starts to break down when  $\eta$  gets smaller, separating from the correct result close to the minimum of the damping. Although

this approximation simplifies the calculation, it is only valid as long in a certain range: The deviation is larger when the broadening,  $\eta$ , is small compared to the spin-orbit interaction strength (the values used in the code are  $\lambda_{\text{Fe}} = 0.004$ ,  $\lambda_{\text{Ni}} = 0.0055$ ,  $\lambda_{\text{Co}} = 0.005666$ ). Further approximations done in Equation 5.4.5 and Equation 5.4.8 give values for the Gilbert damping that are in very good agreement with the results obtained for Equation 5.4.3.

In the absence of spin-orbit interaction, no energy dissipation through the orbital angular momentum is possible. From Figure 5.5, one can see that this results in a linear behaviour of the damping, vanishing in the limit  $\eta \rightarrow 0$ . Mankovsky *et al.* showed that the linear behaviour for large  $\eta$  can be removed by taking vertex corrections into account [70]. Here, a similar result can be achieved by taking the difference between the damping including spin-orbit interaction and the one obtained in its absence. Figure 5.6 shows no linear increase in the  $\eta \rightarrow \infty$  limit anymore. These results are in fairly good agreement with the experiments shown in Ref. [70]. As the curves in Figure 5.5 contain all contributions in the Hamiltonian except the spin-orbit interaction one, the difference can be understood as the pure spin-orbit contributions to the damping.

## 5.5. Torque-torque method (TTM)

Arguing that the intrinsic Gilbert damping ultimately arises from dissipative torques on the individual spins, Hankiewicz *et al.* [51] used a different perspective to obtain the effects of relaxation. They start their argument by writing the equation of motion for the spin-spin response function,  $\chi^{-+}(t) = \langle\langle \hat{S}^-(t), \hat{S}^+ \rangle\rangle$ , as

$$i \frac{d}{dt} \langle\langle \hat{S}^-(t), \hat{S}^+ \rangle\rangle = \delta(t) \langle[\hat{S}^-, \hat{S}^+] \rangle + i \langle\langle \hat{\tau}^-(t), \hat{S}^+ \rangle\rangle \quad (5.5.1)$$

where  $\hat{\tau} = \frac{d}{dt} \hat{S}$  is the total torque acting on the spin, which in the Heisenberg picture can be written as

$$\hat{\tau}^-(t) = \frac{d}{dt} \hat{S}^-(t) = -i [\hat{S}^-(t), \hat{H}] . \quad (5.5.2)$$

The equation of motion for the torque-spin response, appearing in Equation 5.5.1, can also be calculated, using  $\frac{d}{dt} \langle\langle \hat{\tau}(t), \hat{S} \rangle\rangle = \frac{d}{dt} \langle\langle \hat{\tau}, \hat{S}(-t) \rangle\rangle$ , as

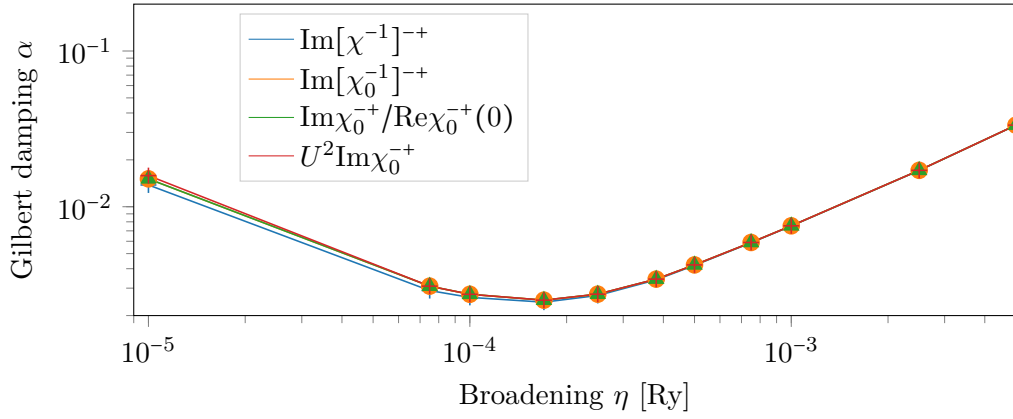
$$i \frac{d}{dt} \langle\langle \hat{\tau}^-, \hat{S}^+(-t) \rangle\rangle = \delta(t) \langle[\hat{\tau}^-, \hat{S}^+] \rangle + i \langle\langle \hat{\tau}^-, \hat{\tau}^+(-t) \rangle\rangle . \quad (5.5.3)$$

The total torque can be split in an external component caused by a magnetic field  $\vec{B}_{\text{ext}} = B_{\text{ext}} \vec{e}_z$  and an intrinsic term that contains the contribution from spin-orbit coupling and, depending on the system, can also contain contributions due to spin pumping [71],

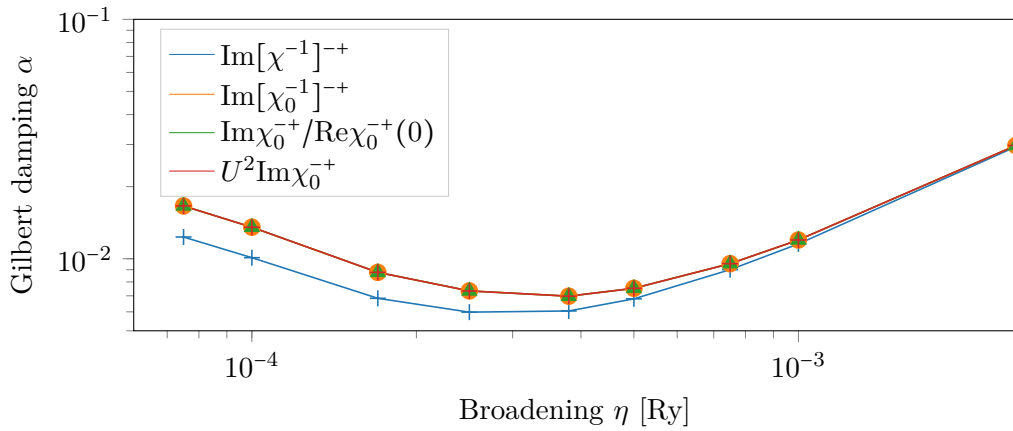
$$\hat{\tau}^\pm = \hat{\tau}_{\text{ext}}^\pm + \hat{\tau}_{\text{int}}^\pm = \mp \mu_B g_S B_{\text{ext}} \hat{S}^\pm + \hat{\tau}_{\text{int}}^\pm . \quad (5.5.4)$$

Using  $[\hat{S}^-, \hat{S}^+] = 2\hat{S}^z$  and  $[\hat{S}^\pm, \hat{S}^z] = \mp \hat{S}^\pm$ , one can write the Fourier transformed equation of motion for the spin-spin response function as

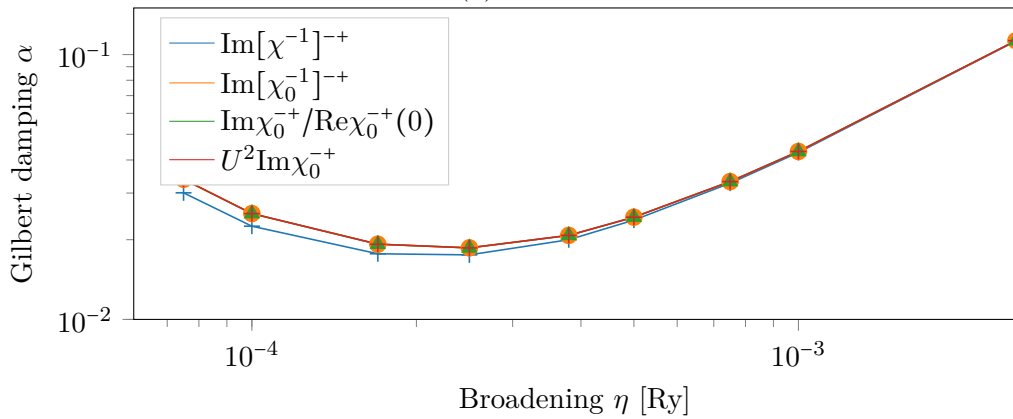
$$(\omega - \mu_B g_S B_{\text{ext}}) \langle\langle \hat{S}^-, \hat{S}^+ \rangle\rangle(\omega) = 2 \langle \hat{S}^z \rangle_0 + i \langle\langle \hat{\tau}_{\text{int}}^-, \hat{S}^+ \rangle\rangle(\omega) . \quad (5.5.5)$$



(a) bcc Fe



(b) fcc Co



(c) fcc Ni

Figure 5.4.: Gilbert damping obtained from the different approximation done within the SCM over the broadening  $\eta$ .

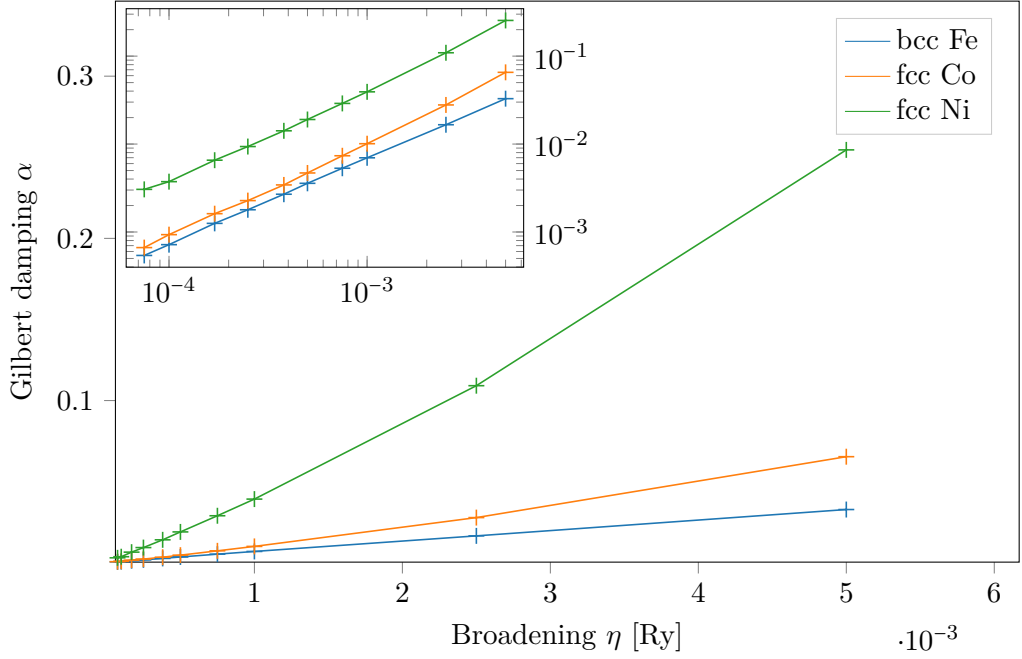


Figure 5.5.: Gilbert damping,  $\alpha$ , with respect to the broadening  $\eta$ , obtained from the inverse slope of the spin–spin response function in RPA, without spin-orbit interaction in the ground state.

Analogously

$$(\omega - \mu_{\text{BGS}} B_{\text{ext}}) \langle\langle \hat{\tau}_{\text{int}}^-, \hat{S}^+ \rangle\rangle(\omega) = \langle[\hat{\tau}_{\text{int}}^-, \hat{S}^+]_0 - i \langle\langle \hat{\tau}_{\text{int}}^-, \hat{\tau}_{\text{int}}^+ \rangle\rangle(\omega) \quad (5.5.6)$$

For the systems of interest, i.e. bulk metals, the internal torque

$$\hat{\tau}_{\text{int}}^\pm = [\hat{S}^\pm, \hat{H}_{\text{SO}}] \quad (5.5.7)$$

arises purely through spin-orbit interaction.

Inserting Equation 5.5.6 into Equation 5.5.5, one can write

$$\langle\langle \hat{S}^-, \hat{S}^+ \rangle\rangle(\omega) = \mathcal{L}^{-+}(\omega) + \mathcal{L}^{-+}(\omega) \Gamma^{-+}(\omega) \mathcal{L}^{-+}(\omega) \quad (5.5.8)$$

where  $\mathcal{L}$  is the spin–spin response in absence of spin-orbit interaction

$$\mathcal{L}^{-+}(\omega) = \frac{2\langle \hat{S}^z \rangle_0}{\omega - \mu_{\text{BGS}} B_{\text{ext}}}, \quad (5.5.9)$$

and

$$\Gamma^{-+}(\omega) = \frac{1}{4\langle \hat{S}^z \rangle_0^2} [i \langle[\hat{\tau}_{\text{int}}^+, \hat{S}^-]_0 + \langle\langle \hat{\tau}_{\text{int}}^+, \hat{\tau}_{\text{int}}^- \rangle\rangle(\omega)]. \quad (5.5.10)$$

Note that this approach does not take into account any additional broadening on the energy levels, and the susceptibility  $\mathcal{L}^{-+}$  is a purely real number. They can be

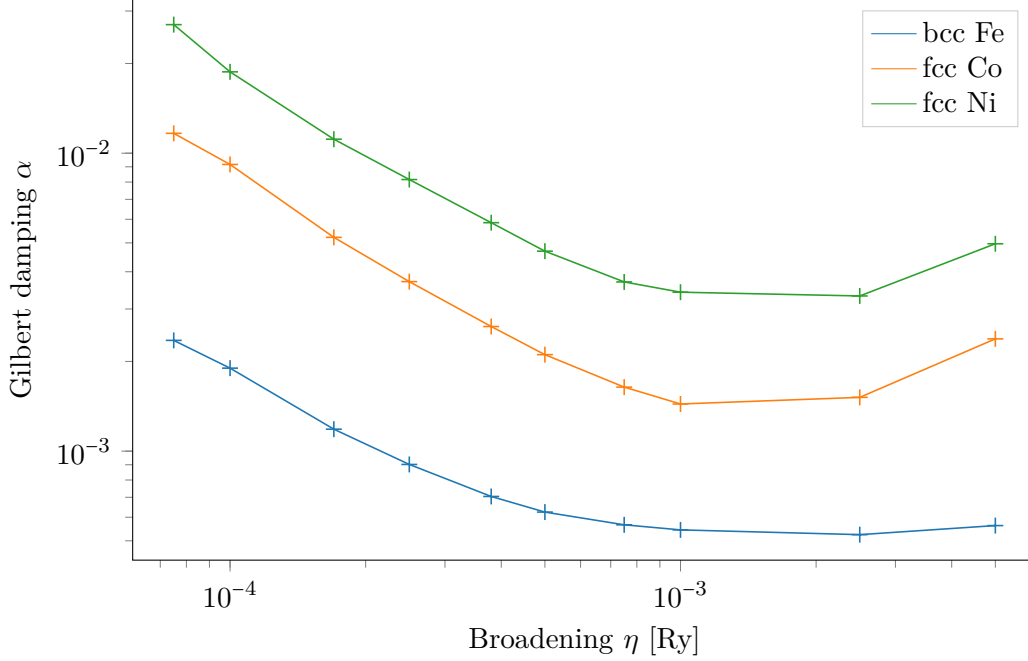


Figure 5.6.: Difference of the curves in Figure 5.3 and Figure 5.5.

added later the same way as done before, when the response functions are calculated in terms of Green functions.

To calculate the damping, given by Equation 5.4.1, the inverse of the transverse spin-spin response is necessary. It can be obtained from Equation 5.5.8, taking into account relatively low spin-orbit interaction, as

$$\begin{aligned}
 [\langle \hat{S}^+, \hat{S}^- \rangle(\omega)]^{-1} &= [\mathcal{L}^{-+}(\omega)]^{-1} (1 + \mathcal{L}^{-+}(\omega) \Gamma^{-+}(\omega))^{-1} \\
 &\approx [\mathcal{L}^{-+}(\omega)]^{-1} (1 - \mathcal{L}^{-+}(\omega) \Gamma^{-+}(\omega)) \\
 &\approx [\mathcal{L}^{-+}(\omega)]^{-1} - \Gamma^{-+}(\omega) .
 \end{aligned} \tag{5.5.11}$$

As the spin-torque commutator in  $\Gamma$  is real, and taking into account temperature and disorder effects through a broadening as before, the damping is given as

$$\begin{aligned}
 \alpha &= \frac{\gamma}{M} \lim_{\omega \rightarrow 0} \frac{\text{Im}[\mathcal{L}^{-1}]^{-+}}{\omega} - \frac{1}{\gamma M} \lim_{\omega \rightarrow 0} \frac{\text{Im} \langle \hat{\tau}^+, \hat{\tau}^- \rangle(\omega)}{\omega} \\
 &= \alpha^{\text{noSO}} - \frac{1}{\gamma M} \lim_{\omega \rightarrow 0} \frac{\text{Im} \langle \hat{\tau}^+, \hat{\tau}^- \rangle(\omega)}{\omega} ,
 \end{aligned} \tag{5.5.12}$$

where  $M = 2\langle \hat{S}^z \rangle_0$ . Equation 5.5.12 was also implemented directly in TITAN, where the slope of  $\langle \hat{\tau}^-, \hat{\tau}^+ \rangle$  is calculated at  $\omega \rightarrow 0$ . This method will be called the torque-torque method (TTM). There have been a few approximations made for this approach. Equation 5.5.11 is only valid for low spin-orbit coupling as the geometric series is

aborted after the linear term. According to Edwards, this is equivalent to second order perturbation theory in the spin-orbit coupling parameter [19]. Since each torque operator is already linear in the spin-orbit coupling, the Green functions should be calculated without inclusion of the spin-orbit interaction, otherwise inconsistent results are generated. When this is done, the intraband contribution, responsible for the conductivity-like behaviour of the damping [53], vanishes and the damping is finite in the limit  $\eta \rightarrow 0$ .

In Figure 5.7, one can see that the TTM in RPA without spin-orbit interaction in the ground state, is in good agreement with the results obtained for the spin-orbit contribution in SCM for the region where  $\lambda \ll \eta$ . Interestingly, when adding the spin-orbit interaction in the ground state, the TTM has the same behaviour as the broadening contribution of SCM. The reasons for this must be further investigated.

Another result obtained by Edwards [19] is that without spin-orbit interaction in the Green function, the torque-torque response obtained in Equation 5.5.12 can be calculated within the mean-field approximation, i.e.,

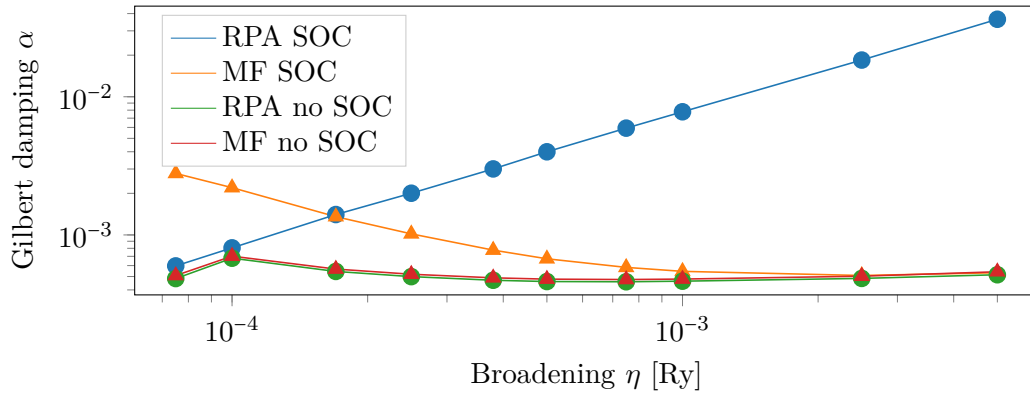
$$\alpha = \alpha_0^{\text{noSO}} - \frac{1}{\gamma M} \lim_{\omega \rightarrow 0} \frac{\text{Im} \langle \langle \hat{\tau}^-, \hat{\tau}^+ \rangle \rangle_0(\omega)}{\omega}. \quad (5.5.13)$$

In absence of spin-orbit interaction, the mean-field TTM provides the same results as the RPA one, with a small gap between the results that is proportional to the spin-orbit coupling strength of the material. For large broadenings, the mean-field responses with and without spin-orbit interaction in the ground state provide similar results. Nevertheless, when  $\eta \ll \lambda$ , the second-order approximation proposed by Edwards is not good, and does not capture the diverging behaviours of  $\alpha$  as expected from the full susceptibility. Surprisingly, the mean-field response including spin-orbit interaction in the ground state presents the same behaviour as the spin-orbit contribution obtained in the SCM, and indicates that the analysis in terms of expanded contributions in  $\lambda$  can be made more general, for the full range of  $\eta$ . This also reflects in the results and discussions made in the next section, for the model of Kambersky.

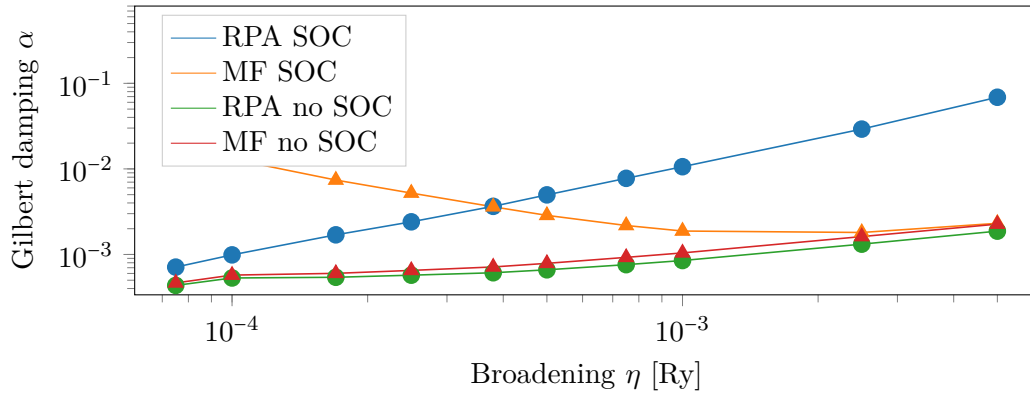
## 5.6. Torque-correlation method (TCM)

For the methods presented in this section, a general result will be used. The mean-field response,  $\langle \langle \hat{A}, \hat{B} \rangle \rangle_0$ , can be written in the Lehmann representation [41] as

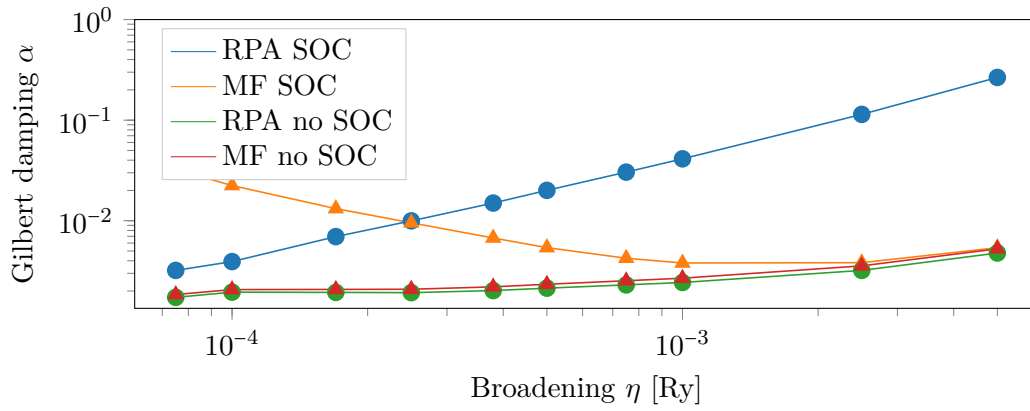
$$\begin{aligned} \langle \langle \hat{A}, \hat{B} \rangle \rangle_0(\omega) &= \sum_{mn} f_{\text{F}}(\epsilon_m) \left( \frac{\langle m | \hat{A} | n \rangle \langle n | \hat{B} | m \rangle}{\omega + (\epsilon_m - \epsilon_n) + i\eta} - \frac{\langle m | \hat{B} | n \rangle \langle n | \hat{A} | m \rangle}{\omega - (\epsilon_m - \epsilon_n) + i\eta} \right) \\ &= \sum_{mn} [f_{\text{F}}(\epsilon_m) - f_{\text{F}}(\epsilon_n)] \frac{\langle m | \hat{A} | n \rangle \langle n | \hat{B} | m \rangle}{\omega + (\epsilon_m - \epsilon_n) + i\eta}. \end{aligned} \quad (5.6.1)$$



(a) bcc Fe



(b) fcc Co



(c) fcc Ni

Figure 5.7.: Gilbert damping over broadening  $\eta$  obtained from the TTM, in RPA and MF approximation, with and without spin-orbit interaction included in the ground state.

Using  $\frac{1}{x \pm i\eta} = \mathcal{P}(\frac{1}{x}) \mp i\pi\delta(x)$ , where  $\mathcal{P}$  gives the Cauchy principal value, the imaginary part of the mean-field response is given as

$$\begin{aligned} \text{Im}\langle\langle\hat{A}, \hat{B}\rangle\rangle_0(\omega) &= \pi \sum_{mn} [f_{\text{F}}(\epsilon_n) - f_{\text{F}}(\epsilon_m)] \langle m|\hat{A}|n\rangle \langle n|\hat{B}|m\rangle \delta(\omega + \epsilon_m - \epsilon_n) \\ &= \pi \sum_{mn} [f_{\text{F}}(\epsilon_m + \omega) - f_{\text{F}}(\epsilon_m)] \langle m|\hat{A}|n\rangle \langle n|\hat{B}|m\rangle \delta(\omega + \epsilon_m - \epsilon_n) \end{aligned} \quad (5.6.2)$$

The slope of Equation 5.6.2, can be calculated as

$$\begin{aligned} \lim_{\omega \rightarrow 0} \frac{\text{Im}\langle\langle\hat{A}, \hat{B}\rangle\rangle_0(\omega)}{\omega} &= \pi \sum_{mn} \lim_{\omega \rightarrow 0} \frac{f_{\text{F}}(\epsilon_m + \omega) - f_{\text{F}}(\epsilon_m)}{\omega} \langle m|\hat{A}|n\rangle \langle n|\hat{B}|m\rangle \delta(\omega + \epsilon_m - \epsilon_n) \\ &= \pi \sum_{mn} \frac{df_{\text{F}}(\epsilon_m)}{d\omega} \langle m|\hat{B}|n\rangle \langle n|\hat{B}|m\rangle \delta(\epsilon_m - \epsilon_n) \\ &= -\pi \sum_{mn} \delta(\epsilon_m - \epsilon_{\text{F}}) \langle m|\hat{A}|n\rangle \langle n|\hat{B}|m\rangle \delta(\epsilon_m - \epsilon_n) . \end{aligned} \quad (5.6.3)$$

Adding a complete basis set  $\sum_{\ell} |\ell\rangle\langle\ell| = 1$ , the slope can be rewritten in terms of single particle Green functions as

$$\begin{aligned} \lim_{\omega \rightarrow 0} \frac{\text{Im}\langle\langle\hat{A}, \hat{B}\rangle\rangle_0(\omega)}{\omega} &= -\pi \sum_{mn} \text{Tr} [ |m\rangle\delta(\epsilon_m - \epsilon_{\text{F}}) \langle m|\hat{A}|n\rangle \delta(\epsilon_n - \epsilon_{\text{F}}) \langle n|\hat{B}|m\rangle ] \\ &= \frac{\pi}{4} \text{Tr} [ (G^r(\epsilon_{\text{F}}) - G^a(\epsilon_{\text{F}})) \hat{A} (G^r(\epsilon_{\text{F}}) - G^a(\epsilon_{\text{F}})) \hat{B} ] \\ &= -\frac{1}{\pi} \text{Tr} [ \text{Im}G(\epsilon_{\text{F}}) \hat{A} \text{Im}G(\epsilon_{\text{F}}) \hat{B} ] \end{aligned} \quad (5.6.4)$$

Here, it has been used that  $\text{Im}G(\epsilon_{\text{F}}) = -\pi \sum_m |m\rangle\delta(\epsilon_{\text{F}} - \epsilon_m) \langle m| = -\frac{i}{2} [G^r(\epsilon_{\text{F}}) - G^a(\epsilon_{\text{F}})]$ . Thus, the slope of a mean-field response can be written as a Fermi-level quantity, reducing the amount of necessary calculations significantly.

### 5.6.1. Spin-orbit torque (TCM-SO)

Using the result obtained above for the TTM in Equation 5.5.13, one obtains

$$\alpha = -\frac{\gamma}{4M\pi} \text{Tr} [ \text{Im}G(\epsilon_{\text{F}}) \hat{\tau}^- \text{Im}G(\epsilon_{\text{F}}) \hat{\tau}^+ ] , \quad (5.6.5)$$

which is equivalent to the result obtained by Kamberskys in 1976 [18], and has been used by many due to its simplicity, requiring only an integration of the Brillouin zone [72, 73]. This approach is called the torque-correlation method (TCM), and for bulk systems, it involves only the spin-orbit torque  $\tau^{\pm} = [\hat{S}^{\pm}, \hat{H}_{\text{SO}}]$ . This method will be referenced as TCM-SO from here on, to differentiate from the method given in the next section.

As can be seen from Figure 5.8, this approximation is in very good agreement with the results obtained for the TTM in Equation 5.5.13, with and without spin-orbit interaction included in the ground state. They demonstrate that TCM-SO

without spin-orbit interaction in the ground state is only valid in the  $\lambda \ll \eta$  regime, but including spin-orbit interaction gives reasonable results for  $\alpha$ , as will be seen in section 5.7.

### 5.6.2. Exchange-correlation torque (TCM-XC)

Using now Equation 5.6.4 on Equation 5.4.8, the damping can also be obtained as

$$\alpha = -\frac{1}{M\gamma\pi} \text{Tr}[\text{Im}G(\epsilon_F)\tau_{\text{XC}}^-\text{Im}G(\epsilon_F)\tau_{\text{XC}}^+] \quad (5.6.6)$$

where

$$\hat{\tau}_{\text{XC}}^\pm = [\hat{S}^\pm, UM\hat{S}^z] = \mp UM\hat{S}^\pm. \quad (5.6.7)$$

This result will henceforth be referred to as TCM-XC, since it involves the exchange-correlation torque. It was also derived using a different approach [74] and also appears in the literature [21, 70].

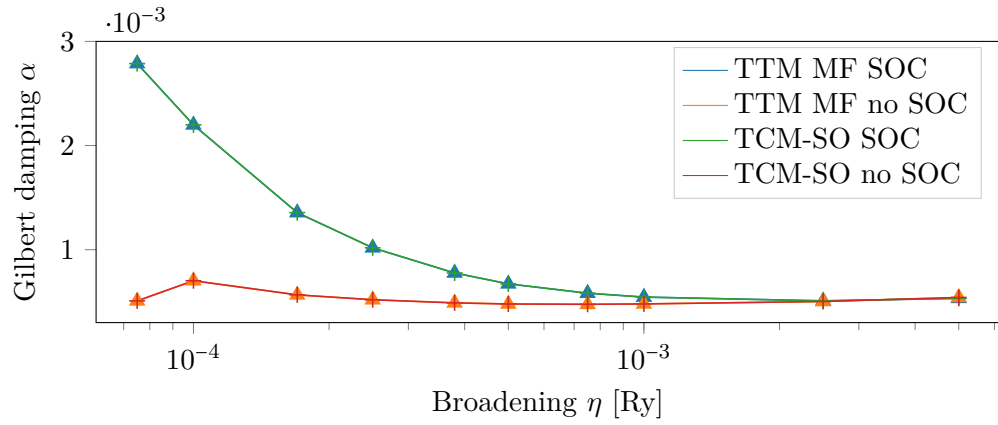
As before, this approximation results in a simple formula that provides values in very good agreement with the SCM method using mean-field approximation in Equation 5.4.8. The comparisons are shown in Figure 5.9.

## 5.7. Summary of methods

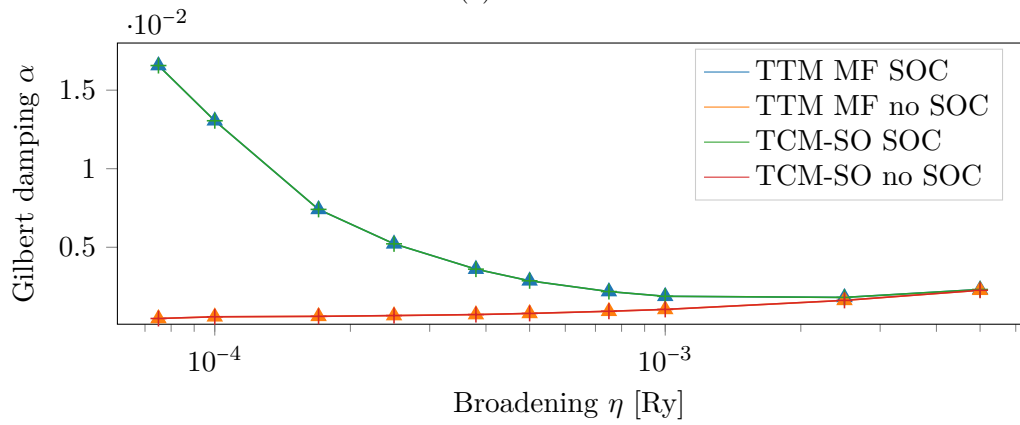
This chapter introduced many different methods to calculate the Gilbert damping. Starting from the FMR experimental setup, the damping was obtained from the calculations of the transverse susceptibility as a function of the frequency, in Figure 5.2. The results presented a divergence for  $\eta \rightarrow 0$  (conductivity-like), as well as an increase with  $\eta$  for larger broadenings (resistivity-like). It was shown that very similar results are obtained by mapping the results to the inverse susceptibility obtained from LLG in the static limit.

From the SCM results, one could see that the approximation, from the RPA to the MF response results in a small deviation that gets larger when the broadening gets small with respect to the spin-orbit interaction. This indicates that the approximation is valid when the spin-orbit coupling strength is small compared to the energy scale of broadening effects. This can be highlighted once more, looking at Figure 5.10, where the damping of bcc Fe is calculated for scaled strengths of the spin-orbit interaction. One can furthermore see that the strength of the damping scales significantly with the spin-orbit interaction strength. But, for large broadenings, the curves with different  $\lambda$  converge to the same asymptotic behaviour, which is the contribution to the damping that is completely independent of the spin-orbit interaction, as could be seen in Figure 5.5. This contribution can be decreased by adding vertex corrections [70, 21].

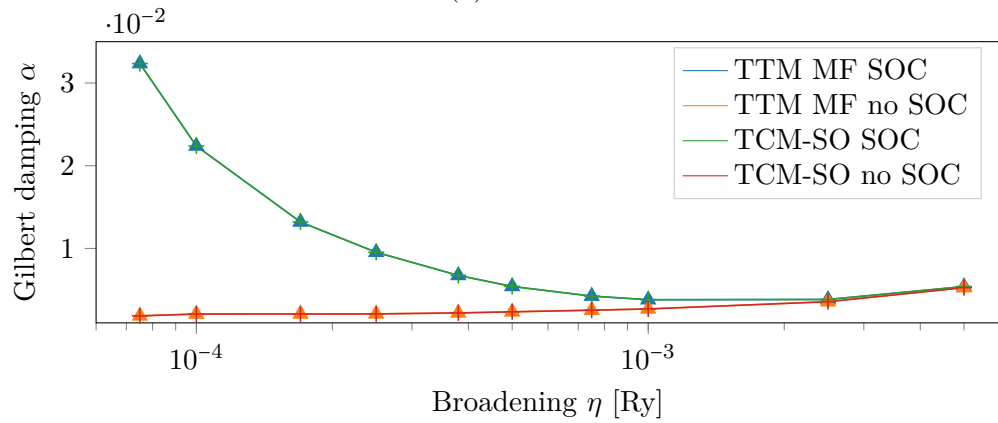
The results obtained from TTM are more peculiar. The damping obtained from calculations without spin-orbit interaction in the ground state, result in non-diverging damping, as predicted by Edwards [19]. In the large broadening limit it recovers the behaviour of the spin-orbit contribution in SCM. On the other hand, if one includes



(a) bcc Fe

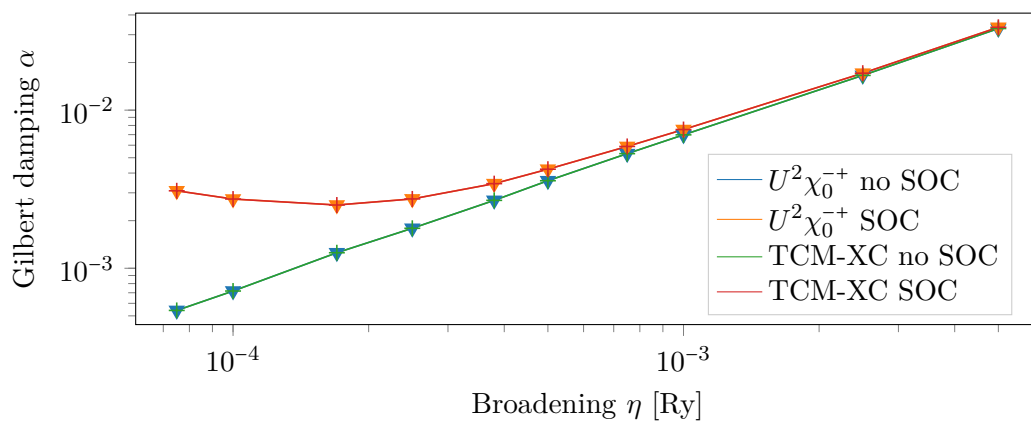


(b) fcc Co

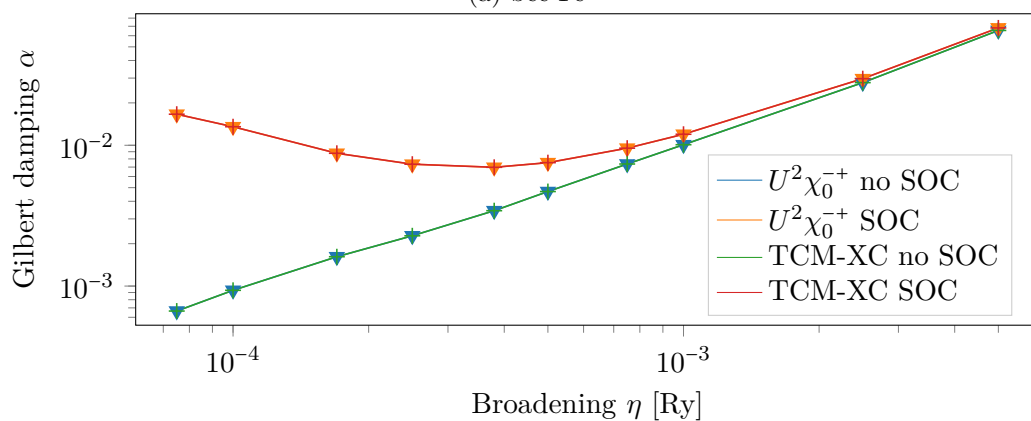


(c) fcc Ni

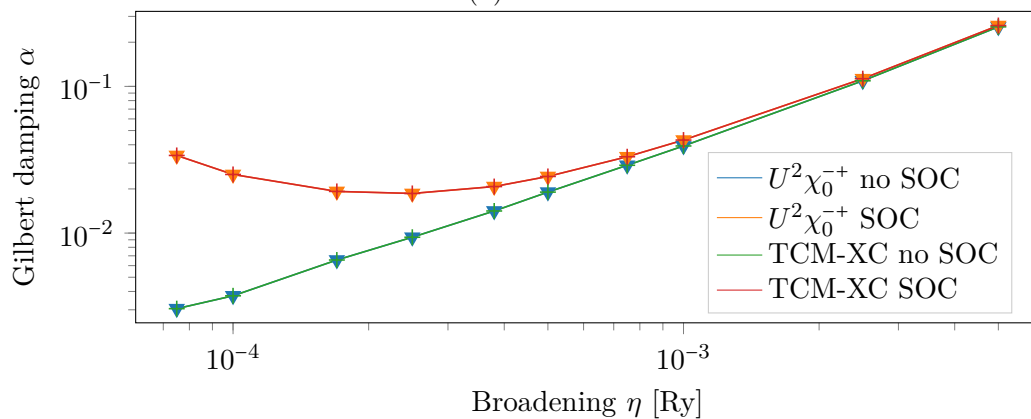
Figure 5.8.: Comparison of Gilbert damping obtained from the TTM in mean-field approximation and from the TCM-SO over broadening  $\eta$ .



(a) bcc Fe



(b) fcc Co



(c) fcc Ni

Figure 5.9.: Comparison of Gilbert damping obtained from Equation 5.4.8 and from the TCM-SO over broadening  $\eta$ .

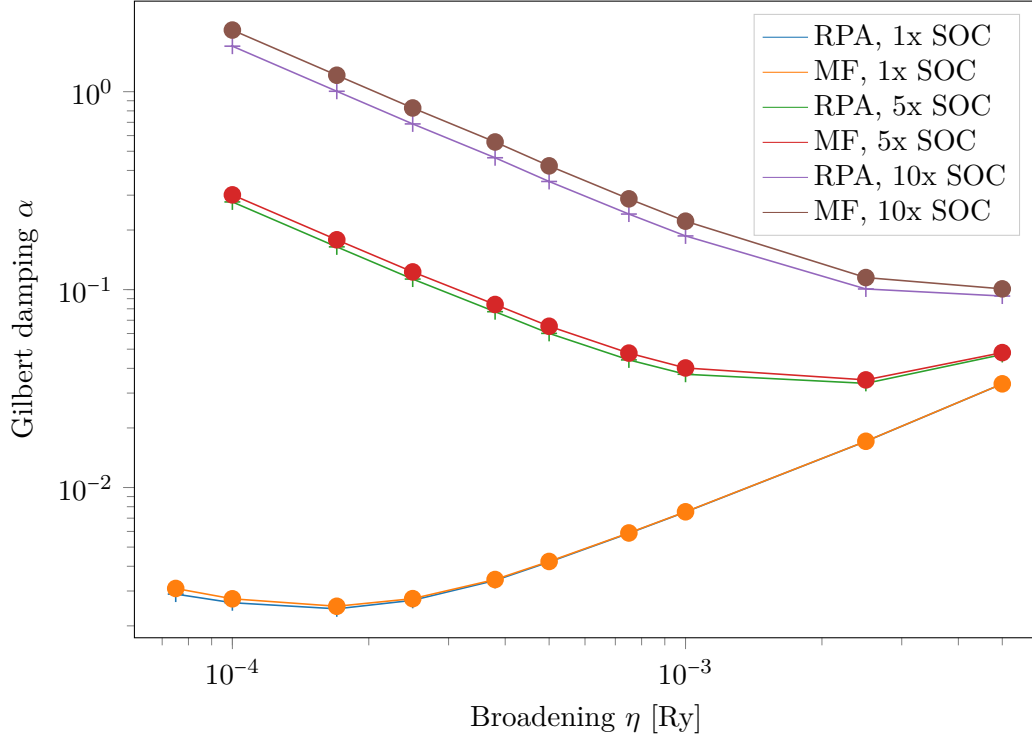


Figure 5.10.: Gilbert damping,  $\alpha$ , for bcc Fe with respect to the broadening  $\eta$  obtained from the inverse slope of the spin–spin response function in RPA and MF. Influence of the spin-orbit coupling strength on the validity of the approximation.

the spin-orbit interaction in the ground state for these calculations, two completely different behaviours from RPA and MF approximation are found (see Figure 5.7). From the RPA result, one can see the same resistivity-like linear behaviour as could already be seen for SCM without spin-orbit interaction, whereas the MF one resembles the pure spin-orbit contribution of SCM.

Both TCM approaches show that, for the investigated materials, they perfectly approximate the results obtained for their respective mean field response. But as the mean-field approximation deviates for regions where the spin-orbit interaction is large with respect to the broadening, so is the TCM.

In Figure 5.11, a comparison of the main results for bcc Fe is shown. One can see that the spin-orbit contribution of the SCM, obtained by the difference between the calculations with and without spin-orbit interaction, are in good agreement with the results obtained from TCM-SO when spin-orbit interaction is present. This is in contradiction with Ref. [19], which claims that this method is equivalent to second order perturbation theory and for that reason should not include spin-orbit interaction in the ground state. The results obtained from TTM in RPA with SOC resemble the linear behaviour obtained from SCM in RPA without SOC.

It could be shown that the Gilbert damping can clearly be split into two independent contributions, those that stem from the spin-orbit interaction and those that appear even without. The contribution obtained without spin-orbit interaction in SCM (and also from TCM-XC), shows a linear behaviour in the limit  $\eta \rightarrow \infty$ . Comparing with experimental and with first principles results that add temperature in a more accurate prescription, it is clear that the broadening added to the energy levels leads to an artificially large increase for large temperatures. Here, this contribution is eliminated by taking the difference between the total damping and that without spin-orbit interaction. This has a similar effect as the inclusion of vertex corrections.

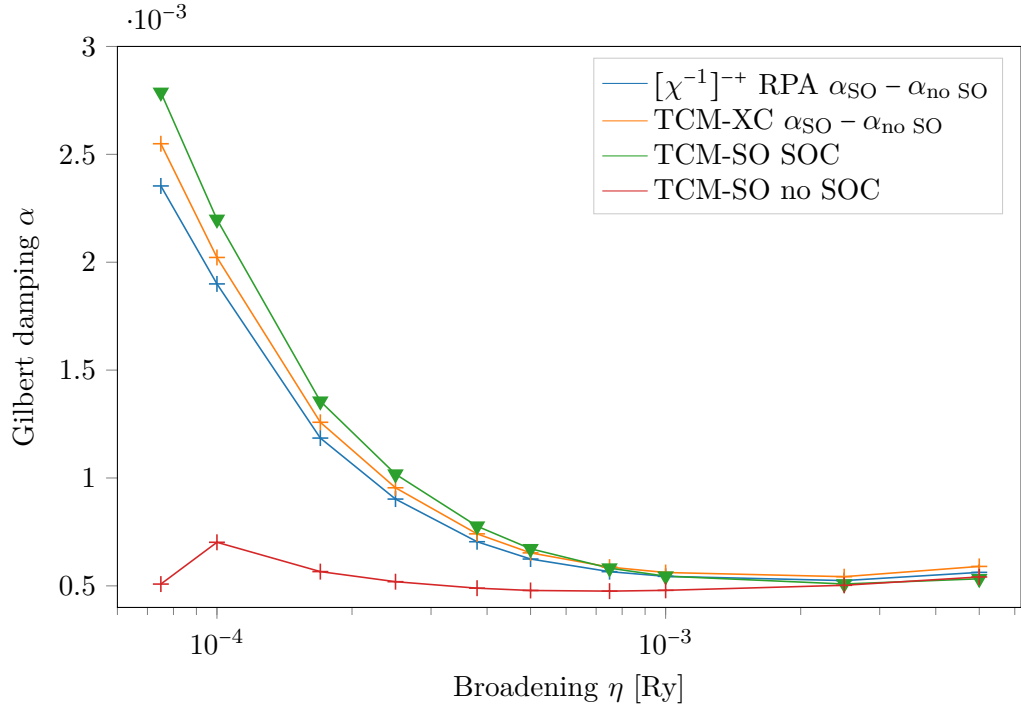
The remaining contribution, which stems purely from spin-orbit interaction, still shows an increase in the clean limit,  $\eta \rightarrow 0$ . This becomes especially clear in the analytical description of the TTM (Equation 5.5.13), where it shows this same result in a perturbative manner. In fact, the divergence seems to be present even in the most accurate methods, namely SCM in RPA and FMR. Additionally, it can be shown analytically that the damping diverges in the mean-field regime for the clean limit by making an analogy with torque calculations [75], since this quantity is also obtained as the slope of a response function with respect to the frequency. In the case of the damping, only the odd contribution in Ref. [75] is present, which diverges as  $\eta^{-1}$  in the  $\eta \rightarrow 0$  limit.

In conclusion, all methods are valid in the  $\eta \gg \lambda$  regime. When the spin-orbit interaction gets large, FMR and SCM in RPA (discounting effects of broadening) are the most accurate methods. Although the former includes higher order contributions in frequency, it can still be interpreted as the quality factor of the system.

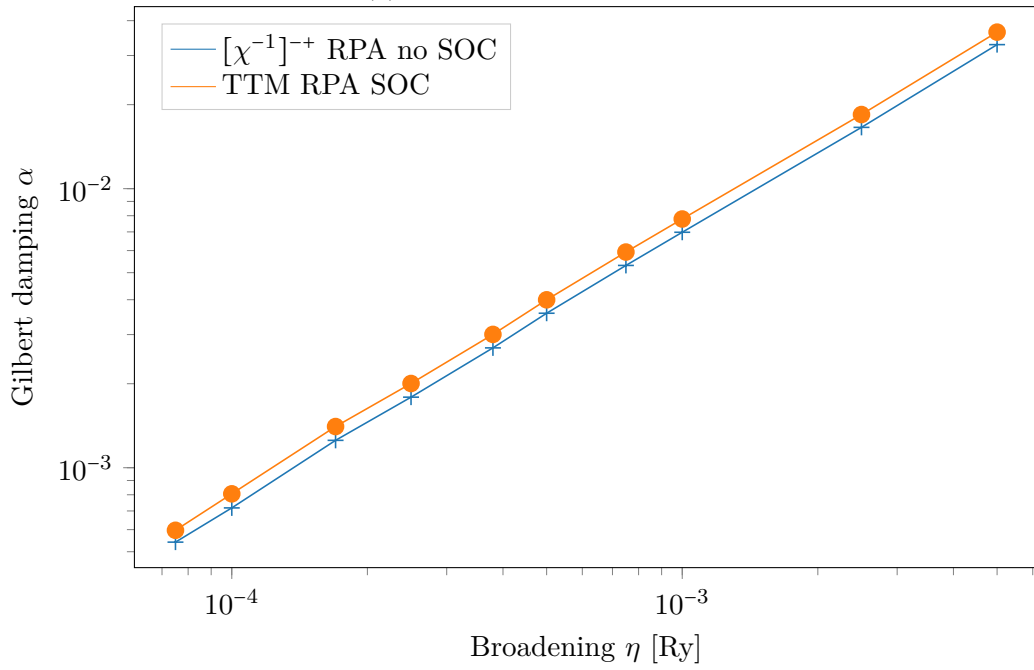
In general, a diverging behaviour of the damping represents an instantaneous flow of the energy out of the spin degree of freedom, immediately stopping any motion of the magnetic system. The magnetization direction would never align with the effective field, retaining its momentary position indefinitely.

Mahfouzi *et al.* [76] have shown that through treatment of the magnetic unit as a quantum object, the damping is obtained from the transition rates of excited states to states with lower energy, and that the divergence thus does not occur.

Another possible approach to achieve finite results in the clean limit is the inclusion of the response of the orbital degree of freedom  $\hat{J} = \hat{S} + \hat{L}$  [77]. Measuring only the spin degrees of freedom (while still exciting both  $\hat{S}$  and  $\hat{L}$ ), the divergence may be cancelled and become finite. This must further be investigated.



(a) Spin-orbit contributions



(b) Broadening contributions

Figure 5.11.: Comparison of broadening and spin-orbit contribution of the Gilbert damping for bcc Fe obtained from SCM, TTM and TCM.

## 6. Conclusions

The goal of this thesis was to introduce TITAN, the simulation program for time-dependent transport and angular momentum properties in nanostructures, focusing on the new implementations and on its power and capabilities to describe a key aspect of spin excitations.

In chapter 2, the theoretical framework was introduced. The model Hamiltonian was elaborated, followed by discussions about how the ground state and dynamical properties of the system are described.

Chapter 3 was devoted to discuss the relevant computational aspects of the program. Before the start of this thesis, TITAN only existed to calculate dynamic properties in two systems, fcc CoPt (001) and bcc FeW ( $1\bar{1}0$ ). In the course of this project, the program was generalized to allow for arbitrary 2D and 3D periodic crystal lattices using Slater-Koster tight-binding approximation. This approximation enables the study of dozens of different systems due to the availability of parameters in databases such as Ref. [22]. The implemented scaling law and mixing scheme further increase the range of potential systems, enabling a vast variety of compound materials.

In chapter 4, the quality of the program has been analyzed by investigation of the electronic structure and magnetic ground state properties, while the performance has been evaluated by convergence and speedup measurements. On the one hand, the electronic structure and ground state properties for bcc Fe and fcc Ni are in very good agreement with calculations done using the *ab initio* code SP-KKR, while the match between those codes had a reasonable agreement for fcc Co. On the other hand, the obtained scaling plots, together with the distributed memory usage demonstrate that the program is optimally prepared for the calculation of dynamical properties even for broadening regimes that require extremely fine discretizations of the Brillouin zone. TITAN is now able to process calculations for broadenings in the region  $10^{-5} \text{ Ry} \leq \eta \leq 10^{-4} \text{ Ry}$ , which requires up to a billion points in the Brillouin zone and therefore could not be accessed before, even using novel sophisticated tricks as is done in Ref. [58]. Further improvements can be obtained by performing a self-consistency calculation over orbital dependent densities, which is currently being introduced in the code.

As an application of TITAN, the Gilbert damping was then investigated in chapter 5. Many of the different available methods of calculating the damping using a microscopical theory have been implemented into the program and subsequently compared to understand their similarities and differences. It has been seen that the strength of the spin-orbit interaction plays an important role in the validity of many of these methods. At least for uniaxial bulk systems, those methods that work within the mean-field approximation of the response functions, seem to be only valid in the

limit of low spin-orbit interaction strengths. Between the results obtained in RPA and those obtained within the MF approximation, a gap is forming that scales with the spin-orbit strength. For the investigated materials, the approximations are still reasonable, but it may result in larger errors in multilayers [59], or in systems composed by heavy metals such as Pt which have significantly larger spin-orbit interaction. This again also affects the TCM methods, which are perfect approximations of the mean-field methods, but therefore also share their flaw. Hence, this constitutes a problem, since many people rely on TCM methods for their ease of use and because they are numerically less demanding. The main area of interest for the Gilbert damping is in spintronic applications, where the tuning of the relaxation can be used to manipulate switching times and propagations of spin currents. As could be seen in chapter 5, the damping scales with the spin-orbit interaction strength. Therefore, a large spin-orbit coupling is preferential for shorter magnetic switching times. A still open question is how the TTM in RPA with SOC can be understood. From Figure 5.11, it does seem as if the spin-orbit interaction in the ground state is completely cancelled by the spin-orbit torques in this approach.

Although the focus application of the code was in the spin excitations — especially the damping parameter — many other quantities can be investigated. The previous version of the code has been used to investigate the effect of dynamical spin orbit torques in ferro- and antiferromagnetic multilayers [7] and transport properties of alternating currents up to the THz regime [25]. Further features, that are still expected to be added in the future, are pulsed perturbations and enabling the use of variable numbers of atomic orbitals for calculations of larger unit cells (e.g. to investigate topological spin textures such as Skyrmions).

All the recently implemented features, together with the upcoming ones discussed above, constitute a powerful microscopic material-specific dynamical framework. These developments open up new routes for the investigation of a multitude of phenomena in the rising field of antiferromagnetic spintronics [78]. Possibly relevant systems in this research field are  $\text{Mn}_2\text{Au}$  [79],  $\text{PtMn}$  [8] and  $\text{CuMnAs}$  [14]. More applications for TITAN can be found in the study of transport properties of topological magnetic textures [80], possibly in connection with dynamical properties of orbital moments [81], and topological insulators [82].

## References

- [1] A. Hirohata et al. “Roadmap for Emerging Materials for Spintronic Device Applications”. In: *IEEE Transactions on Magnetics* 51.10 (Oct. 2015), pp. 1–11. ISSN: 0018-9464. DOI: 10.1109/TMAG.2015.2457393.
- [2] E. Saitoh et al. “Conversion of spin current into charge current at room temperature: Inverse spin-Hall effect”. In: *Applied Physics Letters* 88.18 (May 2006), p. 182509. ISSN: 0003-6951. DOI: 10.1063/1.2199473.
- [3] T. Brächer, P. Pirro, and B. Hillebrands. “Parallel pumping for magnon spintronics: Amplification and manipulation of magnon spin currents on the micron-scale”. In: *Physics Reports* 699 (June 2017), pp. 1–34. ISSN: 0370-1573. DOI: 10.1016/J.PHYSREP.2017.07.003.
- [4] W. Zhang et al. “Spin galvanic effect at the conducting SrTiO<sub>3</sub> surfaces”. In: *Applied Physics Letters* 109.26 (Dec. 2016), p. 262402. ISSN: 0003-6951. DOI: 10.1063/1.4973479.
- [5] H. Nakayama et al. “Spin Hall Magnetoresistance Induced by a Nonequilibrium Proximity Effect”. In: *Physical Review Letters* 110.20 (May 2013), p. 206601. ISSN: 0031-9007. DOI: 10.1103/PhysRevLett.110.206601.
- [6] M. Z. Hasan and C. L. Kane. “Colloquium : Topological insulators”. In: *Reviews of Modern Physics* 82.4 (Nov. 2010), pp. 3045–3067. ISSN: 0034-6861. DOI: 10.1103/RevModPhys.82.3045.
- [7] F. S. M. Guimarães et al. “Dynamical current-induced ferromagnetic and anti-ferromagnetic resonances”. In: *Physical Review B* 92.22 (Dec. 2015), p. 220410. ISSN: 1098-0121. DOI: 10.1103/PhysRevB.92.220410.
- [8] W. Zhang et al. “Spin Hall Effects in Metallic Antiferromagnets”. In: *Physical Review Letters* 113.19 (Nov. 2014), p. 196602. ISSN: 0031-9007. DOI: 10.1103/PhysRevLett.113.196602.
- [9] T. Jungwirth, J. Wunderlich, and K. Olejník. “Spin Hall effect devices”. In: *Nature Materials* 11.5 (May 2012), pp. 382–390. ISSN: 1476-1122. DOI: 10.1038/nmat3279.
- [10] P. Gambardella and I. M. Miron. “Current-induced spin-orbit torques.” In: *Philosophical transactions. Series A, Mathematical, physical, and engineering sciences* 369.1948 (Aug. 2011), pp. 3175–97. ISSN: 1364-503X. DOI: 10.1098/rsta.2010.0336.

- [11] K. Garello et al. “Symmetry and magnitude of spin–orbit torques in ferromagnetic heterostructures”. In: *Nature Nanotechnology* 8.8 (Aug. 2013), pp. 587–593. ISSN: 1748-3387. DOI: 10.1038/nnano.2013.145.
- [12] F. Freimuth, S. Blügel, and Y. Mokrousov. “Direct and inverse spin-orbit torques”. In: *Physical Review B* 92.6 (Aug. 2015), p. 064415. ISSN: 1098-0121. DOI: 10.1103/PhysRevB.92.064415.
- [13] K. Garello et al. “Ultrafast magnetization switching by spin-orbit torques”. In: *Applied Physics Letters* 105.21 (Nov. 2014), p. 212402. ISSN: 0003-6951. DOI: 10.1063/1.4902443.
- [14] P. Wadley et al. “Electrical switching of an antiferromagnet”. In: *Science* 351.6273 (Feb. 2016), pp. 587–590. ISSN: 0036-8075. DOI: 10.1126/science.aab1031.
- [15] E.M. Lifshitz and L.P. Pitaevskii. *Statistical Physics: Theory of the Condensed State*. Bd. 9. Elsevier Science, 2013. ISBN: 9780080503509.
- [16] T.L. Gilbert. “Classics in Magnetism A Phenomenological Theory of Damping in Ferromagnetic Materials”. In: *IEEE Transactions on Magnetism* 40.6 (Nov. 2004), pp. 3443–3449. ISSN: 0018-9464. DOI: 10.1109/TMAG.2004.836740.
- [17] V. Kamberský. “On the Landau–Lifshitz relaxation in ferromagnetic metals”. In: *Canadian Journal of Physics* 48.24 (Dec. 1970), pp. 2906–2911. ISSN: 0008-4204. DOI: 10.1139/p70-361.
- [18] V. Kamberský. “On ferromagnetic resonance damping in metals”. In: *Czechoslovak Journal of Physics* 26.12 (Dec. 1976), pp. 1366–1383. ISSN: 0011-4626. DOI: 10.1007/BF01587621.
- [19] D. M. Edwards. “The absence of intraband scattering in a consistent theory of Gilbert damping in pure metallic ferromagnets”. In: *Journal of Physics: Condensed Matter* 28.8 (Mar. 2016), p. 086004. ISSN: 0953-8984. DOI: 10.1088/0953-8984/28/8/086004.
- [20] I. Garate and A. MacDonald. “Gilbert damping in conducting ferromagnets. I. Kohn-Sham theory and atomic-scale inhomogeneity”. In: *Physical Review B* 79.6 (Feb. 2009), p. 064403. ISSN: 1098-0121. DOI: 10.1103/PhysRevB.79.064403. eprint: 0808.1373.
- [21] H. Ebert et al. “Ab Initio Calculation of the Gilbert Damping Parameter via the Linear Response Formalism”. In: *Physical Review Letters* 107.6 (Aug. 2011), p. 066603. ISSN: 0031-9007. DOI: 10.1103/PhysRevLett.107.066603. eprint: 1102.4551.
- [22] D. Papaconstantopoulos. In: *Handbook of the Band Structure of Elemental Solids*. 2nd Edition. Boston, MA: Springer US, 2015, pp. 1–37. ISBN: 978-1-4419-8264-3. DOI: 10.1007/978-1-4419-8264-3\_1.

- 
- [23] R. Kubo. “Statistical-Mechanical Theory of Irreversible Processes. I. General Theory and Simple Applications to Magnetic and Conduction Problems”. In: *Journal of the Physical Society of Japan* 12.6 (June 1957), pp. 570–586. ISSN: 0031-9015. DOI: 10.1143/JPSJ.12.570.
- [24] M. Born and R. Oppenheimer. “Zur Quantentheorie der Molekeln”. In: *Annalen der Physik* 389.20 (Jan. 1927), pp. 457–484. ISSN: 00033804. DOI: 10.1002/andp.19273892002.
- [25] F. S. M. Guimarães et al. “Dynamical amplification of magnetoresistances and Hall currents up to the THz regime”. In: *Scientific Reports* 7.1 (Dec. 2017), p. 3686. ISSN: 2045-2322. DOI: 10.1038/s41598-017-03924-1.
- [26] L.D. Landau and E.M. Lifshitz. *Quantum Mechanics: Non-Relativistic Theory*. Teoreticheskaja fizika. Elsevier Science, 2013. ISBN: 9781483149127.
- [27] Inigo.quilez. *Spherical Harmonics*. [Online; CC BY-SA 3.0; accessed 22-February-2018]. 2014. URL: <https://commons.wikimedia.org/w/index.php?curid=32782753>.
- [28] M. Finnis. *Interatomic Forces in Condensed Matter*. EBSCO ebook academic collection. Oxford University Press, 2003. ISBN: 9780198509776.
- [29] J. C. Slater and G. F. Koster. “Simplified LCAO Method for the Periodic Potential Problem”. In: *Physical Review* 94.6 (June 1954), pp. 1498–1524. ISSN: 0031-899X. DOI: 10.1103/PhysRev.94.1498.
- [30] O. K. Andersen and O. Jepsen. “Advances in the theory of one-electron energy states”. In: *Physica B+C* 91 (July 1977), pp. 317–328. ISSN: 0378-4363. DOI: 10.1016/0378-4363(77)90200-5.
- [31] J. Shore and D. Papaconstantopoulos. “Transferability and scaling of Slater-Koster parameters in transition metals”. In: *Physical Review B* 35.3 (Jan. 1987), pp. 1122–1128. ISSN: 0163-1829. DOI: 10.1103/PhysRevB.35.1122.
- [32] J. Hubbard. “Electron Correlations in Narrow Energy Bands”. In: *Proceedings of the Royal Society A: Mathematical, Physical and Engineering Sciences* 276.1365 (Nov. 1963), pp. 238–257. ISSN: 1364-5021. DOI: 10.1098/rspa.1963.0204.
- [33] R. D. Lowde and C. G. Windsor. “Magnetic Excitations in Nickel”. In: *Journal of Applied Physics* 40.3 (Mar. 1969), pp. 1442–1442. ISSN: 0021-8979. DOI: 10.1063/1.1657709.
- [34] A. Edström. “Theoretical and Computational Studies on the Physics of Applied Magnetism : Magnetocrystalline Anisotropy of Transition Metal Magnets and Magnetic Effects in Elastic Electron Scattering”. Felaktigt ISBN i den tryckta versionen: 9789155497149. PhD thesis. Uppsala University, Materials Theory, 2016. ISBN: 978-91-554-9753-8.
- [35] F. S. M. Guimarães. “Dinâmica de spins em nanoestruturas metálicas”. PhD thesis. Universidade Federal Fluminense, Instituto de Física, 2011.

- [36] E. C. Stoner. “Collective Electron Ferromagnetism”. In: *Proceedings of the Royal Society A: Mathematical, Physical and Engineering Sciences* 165.922 (Apr. 1938), pp. 372–414. ISSN: 1364-5021. DOI: 10.1098/rspa.1938.0066.
- [37] G. C. Wick. “The Evaluation of the Collision Matrix”. In: *Physical Review* 80.2 (Oct. 1950), pp. 268–272. ISSN: 0031-899X. DOI: 10.1103/PhysRev.80.268.
- [38] H. Bruus and K. Flensberg. *Many-Body Quantum Theory in Condensed Matter Physics: An Introduction*. Oxford Graduate Texts. OUP Oxford, 2004. ISBN: 9780191057472.
- [39] A. L. Fetter and J. D. Walecka. *Quantum Theory of Many-particle Systems*. Dover Books on Physics. Dover Publications, 2003. ISBN: 9780486428277.
- [40] J. Glazer and E. Tosatti. “Theory of spin-flip excitations across the ferromagnetic stoner gap in electron energy loss”. In: *Solid State Communications* 52.11 (Dec. 1984), pp. 905–908. ISSN: 0038-1098. DOI: 10.1016/0038-1098(84)90852-4.
- [41] G. Giuliani and G. Vignale. *Quantum Theory of the Electron Liquid*. Cambridge: Cambridge University Press, 2005. ISBN: 9780511619915. DOI: 10.1017/CB09780511619915.
- [42] R. D. Mattuck. *A Guide to Feynman Diagrams in the Many-Body Problem: Second Edition*. Dover Books on Physics. Dover Publications, 2012. ISBN: 9780486131641.
- [43] P. Hohenberg and W. Kohn. “Inhomogeneous Electron Gas”. In: *Physical Review* 136.3B (Nov. 1964), B864–B871. ISSN: 0031-899X. DOI: 10.1103/PhysRev.136.B864.
- [44] W. Kohn and L. J. Sham. “Self-Consistent Equations Including Exchange and Correlation Effects”. In: *Physical Review* 140.4A (Nov. 1965), A1133–A1138. ISSN: 0031-899X. DOI: 10.1103/PhysRev.140.A1133.
- [45] The Numerical Algorithms Group (NAG), Oxford, United Kingdom. *The NAG Fortran Library*. [www.nag.com](http://www.nag.com).
- [46] J. Chico. *SP-KKR results for magnetization, band structure and LDOS of bcc Fe, fcc Co, and fcc Ni*. Private communications. Feb. 2018.
- [47] H. Ebert, D. Ködderitzsch, and J. Minár. “Calculating condensed matter properties using the KKR-Green’s function method—recent developments and applications”. In: *Reports on Progress in Physics* 74.9 (Sept. 2011), p. 096501. ISSN: 0034-4885. DOI: 10.1088/0034-4885/74/9/096501.
- [48] E. Şaşıoğlu, C. Friedrich, and S. Blügel. “Effective Coulomb interaction in transition metals from constrained random-phase approximation”. In: *Physical Review B* 83.12 (Mar. 2011), p. 121101. ISSN: 1098-0121. DOI: 10.1103/PhysRevB.83.121101.

- 
- [49] I. M. Billas, A. Châtelain, and W. A. de Heer. “Magnetism from the atom to the bulk in iron, cobalt, and nickel clusters.” In: *Science (New York, N. Y.)* 265.5179 (Sept. 1994), pp. 1682–4. ISSN: 0036-8075. DOI: 10.1126/science.265.5179.1682.
- [50] C. Barreteau et al. “Effects of intersite Coulomb interactions on ferromagnetism: Application to Fe, Co, and Ni”. In: *Physical Review B* 69.6 (Feb. 2004), p. 064432. ISSN: 1098-0121. DOI: 10.1103/PhysRevB.69.064432.
- [51] E. M. Hankiewicz, G. Vignale, and Y. Tserkovnyak. “Gilbert damping and spin Coulomb drag in a magnetized electron liquid with spin-orbit interaction”. In: *Physical Review B* 75.17 (May 2007), p. 174434. ISSN: 1098-0121. DOI: 10.1103/PhysRevB.75.174434.
- [52] M. Fähnle, D. Steiauf, and C. Illg. “Generalized Gilbert equation including inertial damping: Derivation from an extended breathing Fermi surface model”. In: *Physical Review B* 84.17 (Nov. 2011), p. 172403. ISSN: 1098-0121. DOI: 10.1103/PhysRevB.84.172403.
- [53] K. Gilmore, Y. U. Idzerda, and M. D. Stiles. “Identification of the Dominant Precession-Damping Mechanism in Fe, Co, and Ni by First-Principles Calculations”. In: *Physical Review Letters* 99.2 (July 2007), p. 027204. ISSN: 0031-9007. DOI: 10.1103/PhysRevLett.99.027204.
- [54] B. Heinrich and Z. Frait. “Temperature Dependence of the FMR Linewidth of Iron Single-Crystal Platelets”. In: *physica status solidi (b)* 16.1 (Jan. 1966), K11–K14. ISSN: 03701972. DOI: 10.1002/pssb.19660160138.
- [55] B. Heinrich, D. J. Meredith, and J. F. Cochran. “Wave number and temperature dependent Landau-Lifshitz damping in nickel”. In: *Journal of Applied Physics* 50.B11 (July 1979), p. 7726. ISSN: 00218979. DOI: 10.1063/1.326802.
- [56] I. R. Senitzky. “Dissipation in Quantum Mechanics. The Harmonic Oscillator”. In: *Physical Review* 119.2 (July 1960), pp. 670–679. ISSN: 0031-899X. DOI: 10.1103/PhysRev.119.670.
- [57] E. Barati et al. “Gilbert damping in magnetic layered systems”. In: *Physical Review B* 90.1 (July 2014), p. 014420. ISSN: 1098-0121. DOI: 10.1103/PhysRevB.90.014420.
- [58] A. Umerski and D. M. Edwards. “New calculations of Gilbert damping in ferromagnetic transition metals”. In: *Journal of Physics: Conference Series* 903.1 (Oct. 2017), p. 012056. ISSN: 1742-6588. DOI: 10.1088/1742-6596/903/1/012056.
- [59] A. T. Costa and R. B. Muniz. “Breakdown of the adiabatic approach for magnetization damping in metallic ferromagnets”. In: *Physical Review B* 92.1 (July 2015), p. 014419. ISSN: 1098-0121. DOI: 10.1103/PhysRevB.92.014419.
- [60] D. Thonig et al. “Nonlocal Gilbert damping tensor within the torque-torque correlation model”. In: *Physical Review Materials* 2.1 (Jan. 2018), p. 013801. ISSN: 2475-9953. DOI: 10.1103/PhysRevMaterials.2.013801.

- [61] Y. Tserkovnyak, G. A. Fiete, and B. I. Halperin. “Mean-field magnetization relaxation in conducting ferromagnets”. In: *Applied Physics Letters* 84.25 (June 2004), pp. 5234–5236. ISSN: 0003-6951. DOI: 10.1063/1.1762979.
- [62] S. M. Bhagat and P. Lubitz. “Temperature variation of ferromagnetic relaxation in the 3 d transition metals”. In: *Physical Review B* 10.1 (July 1974), pp. 179–185. ISSN: 0556-2805. DOI: 10.1103/PhysRevB.10.179.
- [63] B. Schweflinghaus et al. “Role of Dzyaloshinskii-Moriya interaction for magnetism in transition-metal chains at Pt step edges”. In: *Physical Review B* 94.2 (July 2016), p. 024403. ISSN: 2469-9950. DOI: 10.1103/PhysRevB.94.024403.
- [64] B. Heinrich et al. “Dynamic Exchange Coupling in Magnetic Bilayers”. In: *Physical Review Letters* 90.18 (May 2003), p. 187601. ISSN: 0031-9007. DOI: 10.1103/PhysRevLett.90.187601.
- [65] S. Bhattacharjee, L. Nordström, and J. Fransson. “Atomistic Spin Dynamic Method with both Damping and Moment of Inertia Effects Included from First Principles”. In: *Physical Review Letters* 108.5 (Jan. 2012), p. 057204. ISSN: 0031-9007. DOI: 10.1103/PhysRevLett.108.057204.
- [66] D. Thonig, O. Eriksson, and M. Pereiro. “Magnetic moment of inertia within the torque-torque correlation model”. In: *Scientific Reports* 7.1 (Dec. 2017), p. 931. ISSN: 2045-2322. DOI: 10.1038/s41598-017-01081-z.
- [67] F. S. M. Guimarães et al. “Engineering elliptical spin-excitations by complex anisotropy fields in Fe adatoms and dimers on Cu(111)”. In: *Physical Review B* 96.14 (Oct. 2017), p. 144401. ISSN: 2469-9950. DOI: 10.1103/PhysRevB.96.144401.
- [68] S. Lounis, M. dos Santos Dias, and B. Schweflinghaus. “Transverse dynamical magnetic susceptibilities from regular static density functional theory: Evaluation of damping and g shifts of spin excitations”. In: *Physical Review B* 91.10 (Mar. 2015), p. 104420. ISSN: 1098-0121. DOI: 10.1103/PhysRevB.91.104420.
- [69] M. dos Santos Dias et al. “Relativistic dynamical spin excitations of magnetic adatoms”. In: *Physical Review B* 91.7 (Feb. 2015), p. 075405. ISSN: 1098-0121. DOI: 10.1103/PhysRevB.91.075405.
- [70] S. Mankovsky et al. “First-principles calculation of the Gilbert damping parameter via the linear response formalism with application to magnetic transition metals and alloys”. In: *Physical Review B* 87.1 (Jan. 2013), p. 014430. ISSN: 1098-0121. DOI: 10.1103/PhysRevB.87.014430. eprint: 1301.2114.
- [71] A. T. Costa et al. “Spin-orbit coupling and spin waves in ultrathin ferromagnets: The spin-wave Rashba effect”. In: *Physical Review B - Condensed Matter and Materials Physics* 82.1 (2010), pp. 1–12. ISSN: 10980121. DOI: 10.1103/PhysRevB.82.014428.

- 
- [72] A. Sakuma. “Theoretical investigation on the relationship between the torque correlation and spin correlation models for the Gilbert damping constant”. In: *Journal of Applied Physics* 117 (2015). DOI: 10.1063/1.4905429doi.org/10.1063/1.4905429.
- [73] D. Thonig and J. Henk. “Gilbert damping tensor within the breathing Fermi surface model: Anisotropy and non-locality”. In: *New Journal of Physics* 16.001 (2014). ISSN: 13672630. DOI: 10.1088/1367-2630/16/1/013032.
- [74] A. Brataas, Y. Tserkovnyak, and G. E. W. Bauer. “Scattering Theory of Gilbert Damping”. In: *Physical Review Letters* 101.3 (July 2008), p. 037207. ISSN: 0031-9007. DOI: 10.1103/PhysRevLett.101.037207. eprint: 0807.5009.
- [75] F. Freimuth, S. Blügel, and Y. Mokrousov. “Spin-orbit torques in Co/Pt(111) and Mn/W(001) magnetic bilayers from first principles”. In: *Physical Review B* 90.17 (Nov. 2014), p. 174423. ISSN: 1098-0121. DOI: 10.1103/PhysRevB.90.174423.
- [76] F. Mahfouzi, J. Kim, and N. Kioussis. “Intrinsic damping phenomena from quantum to classical magnets: An ab initio study of Gilbert damping in a Pt/Co bilayer”. In: *Physical Review B* 96.21 (Dec. 2017), p. 214421. ISSN: 2469-9950. DOI: 10.1103/PhysRevB.96.214421.
- [77] C. Kittel. “On the Gyromagnetic Ratio and Spectroscopic Splitting Factor of Ferromagnetic Substances”. In: *Physical Review* 76.6 (Sept. 1949), pp. 743–748. ISSN: 0031-899X. DOI: 10.1103/PhysRev.76.743.
- [78] T. Jungwirth et al. “Antiferromagnetic spintronics”. In: *Nature Nanotechnology* 11.3 (Mar. 2016), pp. 231–241. ISSN: 1748-3387. DOI: 10.1038/nnano.2016.18.
- [79] M. Jourdan et al. “Epitaxial Mn<sub>2</sub>Au thin films for antiferromagnetic spintronics”. In: *Journal of Physics D: Applied Physics* 48.38 (Sept. 2015), p. 385001. ISSN: 0022-3727. DOI: 10.1088/0022-3727/48/38/385001.
- [80] Y. Ohuchi et al. “Electric-field control of anomalous and topological Hall effects in oxide bilayer thin films”. In: *Nature Communications* 9.1 (Dec. 2018), p. 213. ISSN: 2041-1723. DOI: 10.1038/s41467-017-02629-3.
- [81] M. dos Santos Dias et al. “Chirality-driven orbital magnetic moments as a new probe for topological magnetic structures”. In: *Nature Communications* 7 (Dec. 2016), p. 13613. ISSN: 2041-1723. DOI: 10.1038/ncomms13613.
- [82] T. Hirahara et al. “Interfacing 2D and 3D Topological Insulators: Bi(111) Bilayer on Bi<sub>2</sub>Te<sub>3</sub>”. In: *Physical Review Letters* 107.16 (Oct. 2011), p. 166801. ISSN: 0031-9007. DOI: 10.1103/PhysRevLett.107.166801.



# A. Parameters

In this appendix, the parameters for the investigated materials are given in the format, as they are used in TITAN:

Name

Lattice parameter  $a_0$

$\lambda_p$   $\lambda_d$

$\rho_s$   $\rho_p$   $\rho_d$

$a_1$

$a_2$

$a_3$

s on-site

p on-site

t2g on-site

eg on-site

( $ss\sigma$ ) 1st nearest neighbor

( $pp\sigma$ ) 1st nearest neighbor

( $pp\pi$ ) 1st nearest neighbor

( $dd\sigma$ ) 1st nearest neighbor

( $dd\pi$ ) 1st nearest neighbor

( $dd\delta$ ) 1st nearest neighbor

( $sp\sigma$ ) 1st nearest neighbor

( $sd\sigma$ ) 1st nearest neighbor

( $pd\sigma$ ) 1st nearest neighbor

( $pd\pi$ ) 1st nearest neighbor

( $ss\sigma$ ) 2nd nearest neighbor

( $pp\sigma$ ) 2nd nearest neighbor

( $pp\pi$ ) 2nd nearest neighbor

( $dd\sigma$ ) 2nd nearest neighbor

( $dd\pi$ ) 2nd nearest neighbor

( $dd\delta$ ) 2nd nearest neighbor

( $sp\sigma$ ) 2nd nearest neighbor

( $sd\sigma$ ) 2nd nearest neighbor

( $pd\sigma$ ) 2nd nearest neighbor

( $pd\pi$ ) 2nd nearest neighbor

All parameters are obtained from [22].

### A.1. bcc Fe

5.30  
0.0 0.004  
0.7415  
0.58 0.37 7.05  
0.5 0.5 -0.5  
0.5 -0.5 0.5  
-0.5 0.5 0.5

s on-site	1.2017709017	1	Fe
p on-site	1.8725119829	2	Fe
t2g on-site	0.6881678104	3	Fe
eg on-site	0.6643740535	4	Fe
sss 1st nn	-0.1394413859	5	Fe
pps 1st nn	0.2681021988	6	Fe
ppp 1st nn	0.0297146384	7	Fe
dds 1st nn	-0.0508569255	8	Fe
ddp 1st nn	0.0309574008	9	Fe
ddd 1st nn	-0.0030320531	10	Fe
sps 1st nn	0.1777951121	11	Fe
sds 1st nn	-0.0678095073	12	Fe
pds 1st nn	-0.0930757448	13	Fe
pdp 1st nn	0.0208929181	14	Fe
sss 2nd nn	-0.0314096436	15	Fe
pps 2nd nn	0.1884829849	16	Fe
ppp 2nd nn	0.0390681326	17	Fe
dds 2nd nn	-0.0312470067	18	Fe
ddp 2nd nn	0.0061819027	19	Fe
ddd 2nd nn	0.0007075703	20	Fe
sps 2nd nn	0.0735426247	21	Fe
sds 2nd nn	-0.0388437621	22	Fe
pds 2nd nn	-0.0602805056	23	Fe
pdp 2nd nn	-0.0038276755	24	Fe

### A.2. fcc Co

6.54  
0.0 0.005666  
0.7010  
0.64 0.34 8.02  
0.5 0.5 0.0  
0.5 0.0 0.5  
0.0 0.5 0.5

s on-site	1.1294561625	1	Co
-----------	--------------	---	----

p on-site	1.7526212931	2	Co
t2g on-site	0.6054722667	3	Co
eg on-site	0.6044489145	4	Co
sss 1st nn	-0.0904335380	5	Co
pps 1st nn	0.2374771684	6	Co
ppp 1st nn	-0.0014205084	7	Co
dds 1st nn	-0.0421276167	8	Co
ddp 1st nn	0.0297612343	9	Co
ddd 1st nn	-0.0068388805	10	Co
sps 1st nn	0.1364858747	11	Co
sds 1st nn	-0.0380593911	12	Co
pds 1st nn	-0.0406895205	13	Co
pdp 1st nn	0.0279652234	14	Co
sss 2nd nn	-0.0033726902	15	Co
pps 2nd nn	0.0284892824	16	Co
ppp 2nd nn	0.0109884273	17	Co
dds 2nd nn	-0.0075941500	18	Co
ddp 2nd nn	0.0049518463	19	Co
ddd 2nd nn	-0.0001581584	20	Co
sps 2nd nn	0.0013494873	21	Co
sds 2nd nn	-0.0111941742	22	Co
pds 2nd nn	-0.0106077287	23	Co
pdp 2nd nn	0.0113362744	24	Co

### A.3. fcc Ni

6.55

0.0 0.0055

0.6410

0.69 0.34 8.97

0.5 0.5 0.0

0.5 0.5 0.5

0.0 0.5 0.5

s on-site	1.1552640200	1	Ni
p on-site	1.6058666706	2	Ni
t2g on-site	0.5606777072	3	Ni
eg on-site	0.5575338006	4	Ni
sss 1st nn	-0.0952508897	5	Ni
pps 1st nn	0.2170848101	6	Ni
ppp 1st nn	0.0166009460	7	Ni
dds 1st nn	-0.0371246748	8	Ni
ddp 1st nn	0.0262859277	9	Ni
ddd 1st nn	-0.0060013193	10	Ni
sps 1st nn	0.1400250643	11	Ni

## A. Parameters

---

sds	1st	nn	-0.0388022438	12	Ni
pds	1st	nn	-0.0440008491	13	Ni
pdp	1st	nn	0.0237692818	14	Ni
sss	2nd	nn	-0.0006464904	15	Ni
pps	2nd	nn	0.0621984713	16	Ni
ppp	2nd	nn	0.0068240496	17	Ni
dds	2nd	nn	-0.0065054153	18	Ni
ddp	2nd	nn	0.0034442015	19	Ni
ddd	2nd	nn	-0.0002681518	20	Ni
sps	2nd	nn	0.0144056119	21	Ni
sds	2nd	nn	-0.0101546962	22	Ni
pds	2nd	nn	-0.0101174628	23	Ni
pdp	2nd	nn	0.0051021385	24	Ni

# Acknowledgements

I wish to thank Prof. Samir Lounis for the opportunity to perform this project in his research group.

Special thanks goes to Dr. Filipe S.M. Guimarães for supervising me throughout this project.

My gratitude goes towards Dr. Jonathan Chico for reading this thesis and providing the SP-KKR results to benchmark the ground-state results.

I thank Juba Bouaziz for many fruitful discussions.

I thank Prof. Antonio T. Costa and Prof. Roberto B. Muniz for fruitful discussions regarding the Gilbert damping.

I also thank Flaviano José dos Santos for insightful inputs regarding the Brillouin zone generation.

I am grateful for the computing resources granted by the Jülich Supercomputing Centre under project jias15 and by the RWTH Aachen University under project jara0175.